博士論文

Electronic States and Magnetic Structure of Fe_3O_4 (111) Surfaces
(Fe_3O_4(111)表面の電子状態と磁気構造)

浅川　寛太

Acknowledgments

This research was supported by many people inside and outside Fukutani lab., otherwise it would have been impossible to accomplish this work.

I am deeply grateful to Professor Katsuyuki Fukutani for his invaluable advice and encouragement. He read and commented on the whole manuscript. He has shown me the way to go through his advice, his discussion with us and his own attitudes towards the research. I have learned a lot from him.

I am grateful to Mr. Taizo Kawauchi for supporting me during the beamtime of the synchrotron radiation. He also taught me the fundamental skills of the experiments, machining, designing the experimental apparatus, etc.

All the NRS experiments in this study were supported by Professor Xiaowei Zhang who was a staff of High Energy Accelerator Research Organization (KEK).

I would like to thank Dr. Shohei Ogura for giving me meaningful advice about technical and scientific issues.

I am deeply grateful to the Emeritus Professors Akira Kinbara, Takaaki Kawamura, Yu Fukai and Yoshitada Murata. The suggestions and opinions they gave me were always precise and meaningful.

Dr. Koichi Kato gave me many comments and ideas from the theoretical point of view. My understanding of the electronic properties and magnetism was greatly deepened by the discussions with him.

I would like to express my gratitude to the examination committee, Professors Yukio Hasegawa, Shuji Hasegawa, Daichi Chiba and Yoshio Miura. Their advice helped me improve the quality of this study.

Let me thank the former members of Fukutani Lab. They helped my research in the experiments and discussions. I had meaningful discussions with Dr. Kotaro Takeyasu. He also taught me how to use the ESCA apparatus.

I thank the students of Fukutani Lab. It always was great pleasure for me to have discussions with them. The four-point probe measurements were conducted in collaboration with Mr. Naoki Nagatsuka and Mr. Shohei Ogawa. It would have been impossible to construct the experimental apparatus without their support.

Also, I am indebted to Ms. Tomoka Nakamura for her supports on managements of research funds.

Thank you to the staff in the central workshop in Inst. Industrial Sci., Univ. Tokyo and Kyowa Shinku company. Without their kindness and skills of machining, it would have been impossible to construct the experimental apparatus used in this study.

I want to thank my parents, Junko and Kenichi, for supporting me. They also gave me useful advice as researchers. I am deeply grateful to my fiancée Maho. She has encouraged me so much.

Abstract

Magnetite (Fe_3O_4) is the oldest known magnetic material and still has been attracting scientific interest due to its fascinating characters such as predicted half-metallicity, catalytic activity, magnetism and the metal-to-insulator transition called the Verwey transition. Although the mechanism of the Verwey transition has been under debate for more than 80 years since its discovery, it has been argued that the decrease in electrical conductivity by the Verwey transition can be explained by the formation of charge and orbital ordering of the B-site Fe atoms. It has been reported that the surfaces of Fe_3O_4 have peculiar characters.

In terms of the electronic structure, the behavior of the Verwey transition at surfaces seems to be different from the bulk. The Fe_3O_4 (001) surface has a ($\sqrt{2} \times \sqrt{2}$) $R45^\circ$ superstructure which resembles to the structure under the Verwey transition. For the Fe_3O_4 (111) surface, a band gap has been observed above the Verwey temperature while in the bulk band gap closes above the Verwey temperature. These results suggest that the Verwey temperature at the surface is different from the bulk. Since the Verwey transition is a charge order-disorder transition of the Fe(B) site, it is considered to be sensitive to the charge state of surface Fe(B) sites which may be influenced by the surface electronic states. In this study, we investigated the electronic structure of the Fe_3O_4 (111) surface by ultra-violet photoemission spectroscopy (UPS) in order to establish a method to modulate the charge state of Fe(B) atoms.

The magnetic properties of Fe_3O_4 surfaces are alsxo known to be different from the bulk. It has been reported that the saturation magnetization of the Fe_3O_4 nanoparticles is significantly smaller than bulk samples and that the spins of the Fe(A) and Fe(B) sites are non-collinear. These can be attributed to the effect of the surface because nanoparticles are more largely influenced by the surface than large samples. However, since it is difficult to obtain the stoichiometric nanoparticles and the size effect cannot be excluded in nanoparticles, studies on the well-defined single crystal surface is necessary to clarify the effect of surfaces on the magnetic structure of Fe_3O_4. In this study, we investigated the magnetic structure of the Fe_3O_4 (111) surface by nuclear resonant X-ray scattering (NRS) conversion electron Mössbauer spectroscopy (CEMS).

The UPS results showed that the atomic H adsorbs on the Fe(A)-terminated Fe_3O_4 (111) surface and reduces the work function, but no significant change in the UPS spectra near the Fermi level was observed, which means that the charge state of the surface Fe(B) atoms is not influenced by the H adsorption. This can be understood by assuming that the bonding between the substrate and the H is covalent. The decrease of work function indicates the formation of electric dipole due to the covalent bonding. Furthermore, we have found that by exposing the surface to atomic H after exposing to O_2, the Fe(B) t_{2g}-derived peak of the UPS spectrum can be enhanced. This means that the bonding between the H and the O_2-exposed Fe(A)-terminated Fe_3O_4 (111) surface is ionic, and that the electron released by the H is transfered to the Fe(B) t_{2g} orbital.

From the NRS and the CEMS results, we have found that the Fe_3O_4 (111) surface is covered by closure domains and the magnetization direction of the near-surface region is tilted from the original easy-axes to the surface-parallel direction. This can be attributed to the magnetostatic energy. We have also found that the spin directions of the Fe(A)

and Fe(B) sites are non-collinear to each other. This suggests the presence of a peculiar exchange interaction such as Dzialoshinsky-Moriya interaction near the surface. Furthermore, we have found, using Low-/High-temperature NRS, that the thermal behavior of the magnetization of the Fe_3O_4 (111) surface is different from the bulk. This also indicates the presence of a peculiar exchange interaction since the thermal behavior of the magnetization is largely dependent on the exchange constant.

Contents

Chapter 1

Introduction

1.1 Properties of Fe_3O_4

Magnetite (Fe_3O_4) has attracted interest due to its fascinating characters such as the predicted half-metallicity [1, 2, 3], catalytic activity [4, 5], magnetism, and the metal-to-insulator transition at 120 K called the Verwey transition [6, 7, 7, 8]. In ambient conditions, Fe_3O_4 has an inverse spinel structure with space group $Fd3m$ with the lattice constant of 8.39 Å[9]. Figure 1.1 shows the unit cell of Fe_3O_4. The unit cell consist of 32 O atoms and 24 Fe atoms. The 24 Fe atoms consists of eight tetrahedrally coordinated Fe(A) sites and 16 octahedrally coordinated Fe(B) sites, which are represented by the green and the blue circles in figure 1.1. The Fe(A) sites are occupied by Fe^{3+} ions while Fe(B) sites are occupied by an equal number of Fe^{2+} and Fe^{3+} ions [10, 11, 12].

1.1.1 Electronic Structure of Fe_3O_4

Fe_3O_4 is predicted to be a half metal above the Verwey temperature ($\sim$ 120 K). Half metals are the materials whose Fermi levels are occupied by an electron orbital with one spin direction. Figure 1.3 shows the band structure and the electron density of states of Fe_3O_4 calculated by Jeng *et al.* [1]. The 3*d* orbitals of the Fe(A) and Fe(B) atoms are split into the two-fold degenerate e_g orbital and the three-fold degenerate t_{2g} orbital due to the ligand field. Since the symmetry of the ligand field that the Fe(A) and Fe(B) atoms feel is different, the relation of the energy levels t_{2g} and e_g orbitals depends on the site: The t_{2g} orbital is energetically higher than the e_g orbital in Fe(A) site while in Fe(B) site the e_g orbital is higher than the t_{2g} orbital. Due to the exchange interaction between the electrons, the electron configuration tends to make the total spin momentum the maximum if the ligand splitting is small, which is known as Hund's rules. This makes the energy levels of an electron orbital with a certain spin direction different from the other. In the case of Fe_3O_4, the effect of exchange interaction exceeds that of the ligand splitting. Therefore, the Fe 3*d* bands with a certain spin direction is completely separated from the orbital with the other spin direction, which is called the high-spin state. As shown in figure 1.3 (b), the Fermi level is occupied by the down-spin Fe(B) t_{2g} orbital. This indicates that the hopping of down-spin Fe(B) t_{2g} electrons gives rise to the conductivity, which makes the conduction electrons spin-polarized.

Figure 1.2 shows a simplified illustration of the energy band structure of the Fe 3*d* orbitals. The total spin quantum number of the $Fe(A)^{3+}$, $Fe(B)^{2+}$ and Fe(B) $^{3+}$ are $-5/2$, 2 and $5/2$, respectively.

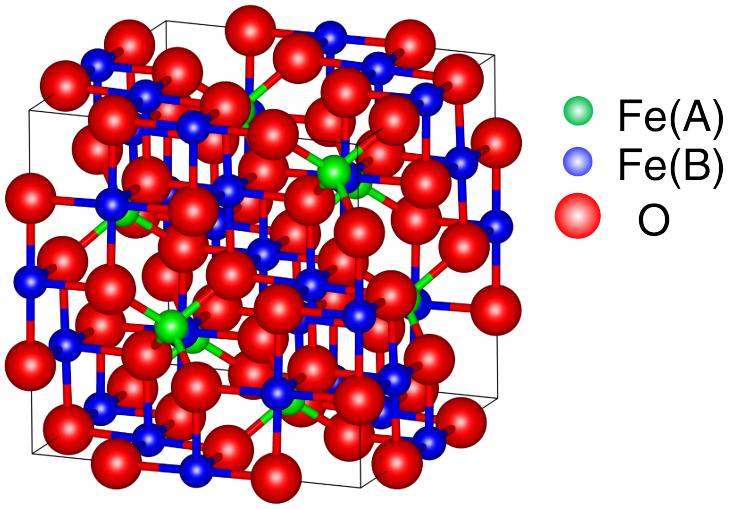

Figure 1.1: The unit cell of Fe_3O_4.

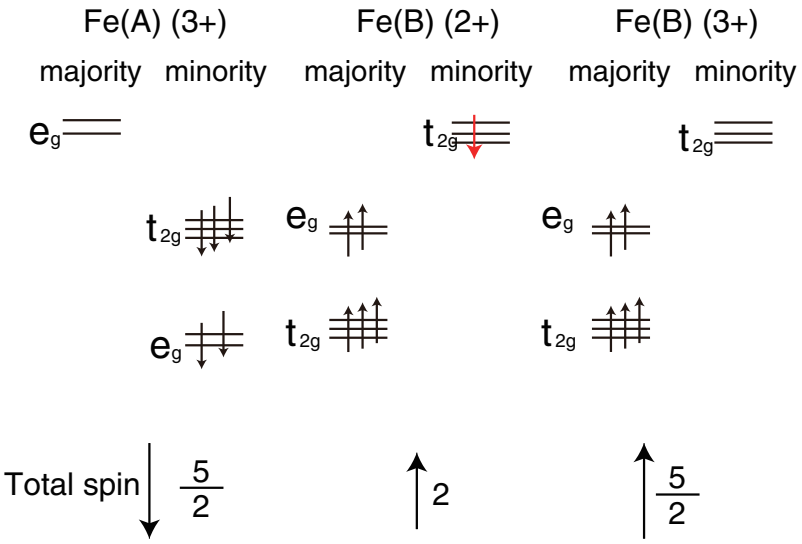

Figure 1.2: The energy band diagram of the Fe 3*d* orbitals.

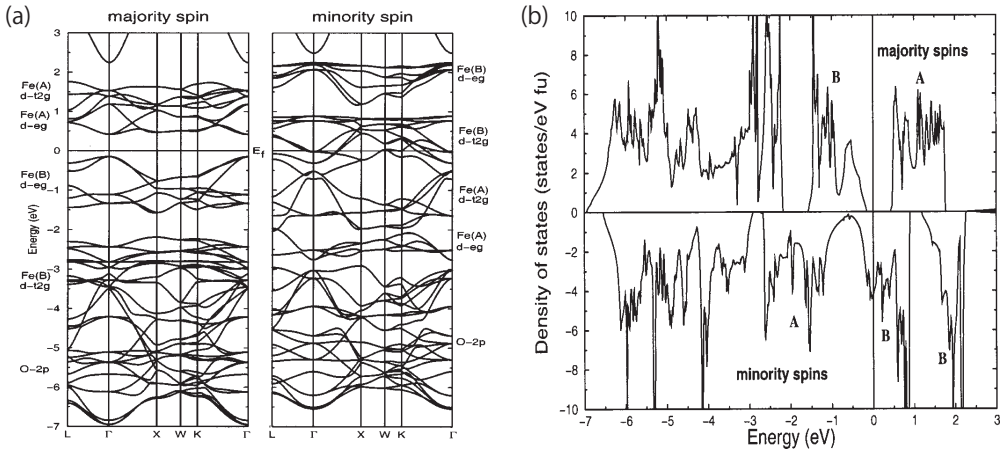

Figure 1.3: (a) The band structure and (b) the electron density of states of Fe_3O_4 [1]. 0 eV corresponds to the Fermi level.

Fe_3O_4 undergoes a metal-to-insulator transition called the Verwey transition at 120 K. Figure 1.5 shows the temperature dependence of the electronic conductivity of an Fe_3O_4 single crystal [6]. Across the Verwey temperature, the crystal structure changes from cubic ($T > T_v$) to monoclinic ($T < T_v$). Although the origin of the Verwey transition is not fully clarified, it is usually explained by formation of a charge and orbital ordering. Figure 1.4 shows the angular distribution of the minority spin 3d electrons of Fe(B) cations for the monoclinic phase ($T < T_v$) reported by Leonov *et al.* [13]. The calculation was based on the local-spin-density approximation (LSDA) with on-site Coulomb interaction (LSDA+U). The results show that the distribution of minotiry-spin Fe(B) t_{2g} electrons exhibits a charge ordering and an orbital ordering.

1.1.2 Magnetic Properties of Fe_3O_4

Exchange Interaction

Fe_3O_4 is a ferrimagnet in which the spins of the Fe atoms that belong to the same sublattice (Fe(A) or Fe(B)) are aligned ferromagnetically but the spin orientations of each sublattice are anti-parallel to each other. The exchange interaction between spins $\boldsymbol{S_1}$ and $\boldsymbol{S_2}$ is written as

$$E_{exchange} = -2J_{12}\boldsymbol{S_1} \cdot \boldsymbol{S_2}, \tag{1.1}$$

where J_{12} is the exchange constant. Table 1.1 shows the experimentally determined exchange constants of Fe_3O_4 estimated by fitting the temperature dependence of hyperfine field observed by Mössbauer spectroscopy [14]. The anti-ferromagnetic spin arrangement of the Fe(A) and Fe(B) spins is due to the superexchange interaction between the Fe(A) and Fe(B) spins via oxygen.

The mechanism of the superexchange interaction can be explained in the following way. Here, we assume a system in which two Fe atoms are bonded to an O atom. The

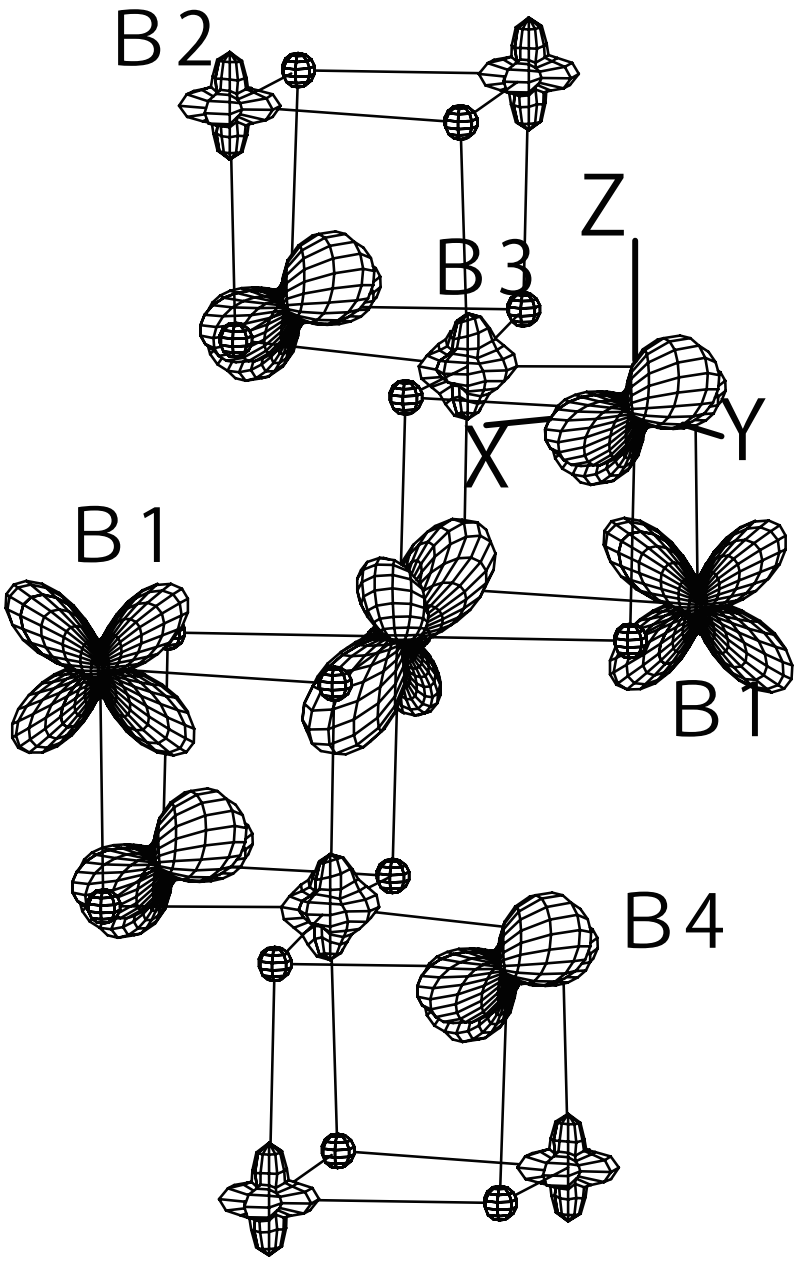

Figure 1.4: The angular distribution of the minority spin 3d electrons of Fe(B) cations for the monoclinic phase ($T < T_v$) of Fe_3O_4 [13].

Table 1.1: The exchange constant of Fe_3O_4. J_{IJ} represents the exchange constant between the I and J sites.

J_{AB}	J_{AA}	J_{BB}
-22 K	-11 K	3 K

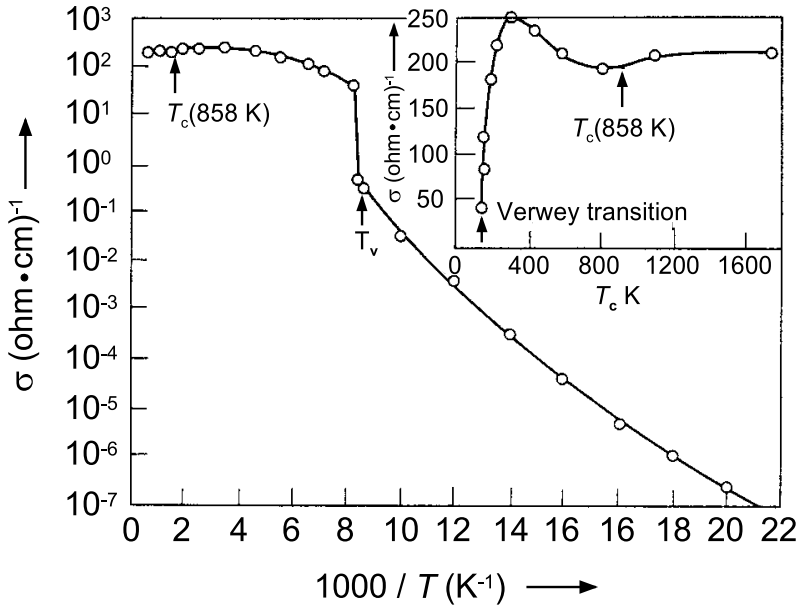

Figure 1.5: The temperature dependence of the electronic conductivity of an Fe_3O_4 single crystal [6].

bonding of Fe and O atoms has covalency which means that electrons can transfer from the O 2*p* and Fe 3*d* orbitals. If all the Fe 3*d* up-spin orbitals are occupied, only the O 2*p* down-spin electrons can be transfered to the Fe 3*d* orbital. If the 2*p* down-spin electron transfers to the Fe 3*d* down-spin orbital, the O atom will have a spin. The spin of the O atom generated by the electron transfer interacts with a spin of another nearest Fe by the exchange interaction. This gives rise to an interaction between the spins of two Fe atoms. The size and the signature of the angle formed by the two Fe-O bonds and the number of electrons in the Fe 3*d* orbital. For example, when the angle between the two Fe-O bonds is 90° and the number of Fe 3d electrons is not five, the exchange interaction between the two Fe atoms is ferromagnetic (i.e. $J > 0$), which is known as Goodenough-Kanamori rule. Figure 1.6 shows the atomic positions of the Fe(A), Fe(B), and O atoms of Fe_3O_4. One O atom is coordinated by one Fe(A) atom and three Fe(B) atoms. The angle formed by two O-Fe(B) bonds is 90° and the angle formed by the O-Fe(A) and the O-Fe(B) bond is 125.3°. From the Goodenough-Kanamori rule, the exchange interaction between the two Fe(B) atoms are considered to be positive, which is consistent with Table 1.1.

Origin of Magnetocrystalline Anisotropy Energy

Although the exchange interaction determines the relationship of the spin direction with the neighboring spins, it does not determine the direction of the total magnetic moment of the crystal. The magnetization is determined by the magnetocrystalline energy. There are several mechanisms that give rise to the magnetocrystalline energy.

Here, we consider the electronic state of a metal ion surrounded by ligands [15]. In the case of Ni^{2+} ions, for example, the 3*d* shell is occupied by 8 electrons, which means that there are ${}_{10}C_8 = 45$ multiplet states with various total spin S and total orbital angular momentum L. These multiplets are split into LS multiplet due to the electron-electron

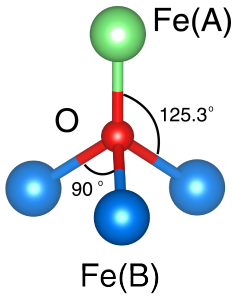

Figure 1.6: Atomic positions of the Fe(A)(green), Fe(B) (blue), and O (red) atoms.

interaction. In the case of a free ion, the multiplet with largest total spin momentum S is the energetically lowest state, which is known as the Hund's rules. In the case of free Ni^{2+} ions, the ground state is the ^3F state ($S = 1$ and $L = 3$) which consists of $(2S + 1) \cdot (2L + 1) = 21$ states. The LS multiplet is further split under ligand field. In the case of cubic ligand field, the ground state is Γ_2 state which consists of three states with $S_z = 0, \pm 1$. The first and the second excited states are the nine-fold Γ_5 state and the nine-fold Γ_4 state. The energy gap between the ground and the first excited state is about 1 eV. In the presence of spin-orbit interaction, the Γ_2 state is modified, which can be described by the second perturbation. The Hamiltonian of the spin-orbit interaction can be written as

$$H_{LS} = \lambda \boldsymbol{L} \cdot \boldsymbol{S}, \tag{1.2}$$

where $\boldsymbol{L}$, $\boldsymbol{S}$, and λ are the total orbital angular momentum, the total spin momentum and the spin-orbit interaction constant. Since the Γ_2 state has three-fold degeneracy, the second perturbation by H_{LS} is a matrix whose element between the ground states $|gM_s\rangle$ and $|gM_{s'}\rangle$ is written as

$$-\sum_e \frac{\langle gM_{s'}|H_{LS}|eM_{s''}\rangle\langle eM_{s''}|H_{LS}|gM_s\rangle}{E_e - E_g}. \tag{1.3}$$

Here, $|eM_{s''}\rangle$ is the first excited states, and $E_e - E_g$ is the energy gap between the ground and the first excited state. From equation 1.2, the numerator of equation 1.3 can be expressed as

$$\langle gM_{s'}|H_{LS}|eM_{s''}\rangle = \sum_\mu \lambda \left\langle g\middle|L_\mu\middle|e\right\rangle \left\langle M_{s'}\middle|S_\mu\middle|M_{s''}\right\rangle, \tag{1.4}$$

where μ is the real space axis ($\mu \in (x, y, z)$). Equation 1.3 can be written as

$$-\sum_e \frac{\sum_{\mu,\nu} \lambda \left\langle g\middle|L_\mu\middle|e\right\rangle \langle e|L_\nu|g\rangle \left\langle M_{s'}\middle|S_\mu\middle|M_{s''}\right\rangle \langle M_{s''}|S_\nu|M_s\rangle}{E_e - E_g}. \tag{1.5}$$

Given the relationship

$$\sum_{M_{s''}} \left\langle M_{s'} \middle| S_\mu \middle| M_{s''} \right\rangle \langle M_{s''} | S_\nu | M_s \rangle = \left\langle M_{s'} \middle| S_\mu S_\nu \middle| M_s \right\rangle, \tag{1.6}$$

the matrix element of H_{ls} is identical to the operator

$$H_{eff} = \lambda^2 \sum_{\mu,\nu} \Lambda_{\mu\nu} S_\mu S_\nu, \tag{1.7}$$

where

$$\Lambda_{\mu\nu} = \sum_e \frac{\left\langle g \middle| L_\mu \middle| e \right\rangle \langle e | L_\nu | g \rangle}{E_e - E_g}. \tag{1.8}$$

The operator H_{eff} is called the effective Hamiltonian since its matrix element $\left\langle gM_{s'} \middle| H_{eff} \middle| gM_s \right\rangle$ is identical to equation 2.29. By choosing an appropriate axis, the perturbation energy $\left\langle gM_s \middle| H_{eff} \middle| gM_s \right\rangle$ can be written as

$$-\lambda^2(\Lambda_{xx} S_x^2 + \Lambda_{yy} S_y^2 + \Lambda_{zz} S_z^2). \tag{1.9}$$

If the crystal symmetry is other than the cubic symmetry, the total magnetization direction is also determined by the magnetocrystalline anisotropy energy which originates from the magnetic dipole interaction and the electron spin-orbit interaction. The first perturbation of the magnetic dipole interaction between the two sites (i, j) with total spin $\boldsymbol{S}$ can be written as

$$\begin{aligned} E_d &= g^2 \mu_B^2 S^2 \sum_{\mu,\nu} \sum_{i,j(i\neq j)} \Phi_{\mu\nu}(\mathrm{r}_{ij}) \alpha_\mu \alpha_\nu, \\ \Phi_{\mu\nu}(\mathrm{r}_{ij}) &= \frac{1}{r_{ij}^3} \left(\delta_{\mu\nu} - \frac{3 x_{ij\mu} x_{ij\nu}}{r_{ij}^2} \right), \end{aligned} \tag{1.10}$$

where g is the g-factor, μ_B is the Bohr magneton, S is the total spin quantum number $\boldsymbol{S}$, r_{ij} is the displacement vector from the site i to j, μ and ν are the spacial axes ($\mu, \nu \in (x, y, z)$), $\alpha_\mu, \alpha\nu$ are the direction cosines between the spin $\boldsymbol{S}$ and the axes μ and ν, and $x_{ij\nu}$ is the ν component of the displacement vector r_{ij}. $\delta_{\mu\nu}$ is the Kronecker delta which is one when $\mu = \nu$ and zero when $\mu \neq \nu$. Equation 1.10 can be written more simply by assuming that the spin i feels an effective magnetic field $H_\mathrm{d}(\boldsymbol{r}_i)$. The μ component of the effective magnetic field $H_{\mathrm{d}\mu}(r_i)$ is

$$H_{d\mu}(\boldsymbol{r}_i) = g\mu_B S \sum_{j,\mu} \Phi_{\mu\nu}(\boldsymbol{r}_{ij}) \alpha_\nu \tag{1.11}$$

where r_i is the position of the spin i. The sum $\sum_j$ runs over all the spins in the sample. Therefore effective magnetic field $H_{d\mu}(\boldsymbol{r}_i)$ includes the contribution from the demagnetizing field which reflects the macroscopic shape of the sample as well as the crystallographic symmetry. In order to distinguish these two contributions, we divide the summation of equation 1.11 into two terms: the contributions from the spins inside and outside of the

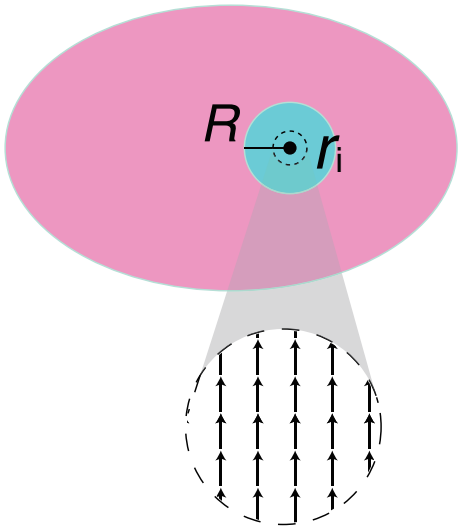

Figure 1.7: Schematic illustration of the model used to understand the anisotropy energy originating from the dipole interaction. The spins inside the sphere with radius R are treated as spins arranged in a periodic structure. The spins outside of the sphere is treated as a continuum.

sphere with radius R whose center is r_i where R is an arbitrary value, which is illustrated in figure 1.7. When R is large enough compared to the lattice constant, the contribution of the spin outside the sphere to the term $\sum_j \Phi_{\mu\nu}(\mathrm{r}_{ij})$ in equation 1.11 can be written, using the integration instead of the summation, as

$$\sum_{j \text{ s.t. } r_{ij} \geq R} \Phi_{\mu\nu}(\mathrm{r}_{ij}) = \frac{1}{\Omega} \int\int\int d^3\boldsymbol{r}_{ij} \left\{ -\frac{\partial}{\partial x_{ij\mu}} \frac{\partial}{\partial x_{ij\nu}} \left(\frac{1}{r_{ij}} \right) \right\}, \tag{1.12}$$

where Ω is the volume of the unit cell. Equation 1.12 can be simplified as

$$\begin{aligned} \sum_{j \text{ s.t. } r_{ij} \geq R} \Phi_{\mu\nu}(\mathrm{r}_{ij}) &= -\frac{1}{\Omega} \left\{ \int_1 dS\, n_\mu \frac{\partial}{\partial x_\nu} \left(\frac{1}{r_{ij}} \right) - \int_2 dS\, n_\mu \frac{\partial}{\partial x_\nu} \left(\frac{1}{r_{ij}} \right) \right\} \\ &= -N_\mu \delta_{\mu\nu} + \frac{4\pi}{3} \delta_{\mu\nu} \end{aligned} \tag{1.13}$$

where $\int_1$ is the integral on the sample surface and $\int_2$ is the integral on the sphere with radius R. n_μ is the μ component of the normal vector. N_μ is the demagnetizing coefficient which satisfies $N_x + N_y + N_z = 4\pi$. On the other hand, the contribution from the spins inside the sphere to the term $\sum_j \Phi_{\mu\nu}(\mathrm{r}_{ij})$ is

$$-\Omega \sum_{j \text{ s.t. } r_{ij} \leq R} \Phi_{\mu\nu}(\mathrm{r}_{ij}) \tag{1.14}$$

From equations 1.13 and 1.14, the effective magnetic field $H_{\mathrm{d}}(\boldsymbol{r}_i)$ is written as

$$\begin{aligned} H_{\mathrm{d}}(\boldsymbol{r}_i) &= \sum_{\nu} \Psi_{\mu\nu} M_\mu - N_\mu M_\mu + \frac{4\pi}{3} M_\mu, \\ \Psi_{\mu\nu} &= \sum_{j \text{ s.t. } r_{ij} \leq R} -\Omega \Phi_{\mu\nu}(\mathrm{r}_{ij}) \end{aligned} \tag{1.15}$$

where M is the magnetization per unit volume. The first term is contribution of the spins inside an isolated sphere with radius R. Therefore, this term includes the effect of the demagnetization field induced by discontinuity at the sphere surface. However, for the present purpose, this demagnetization term should be canceled by the second term in equation 1.16 because the sphere is imaginary and there is no discontinuity at the sphere surface. The third term is the contribution of the demagnetizing field derived from the discontinuity at the sample surface, which is dependent on the shape of the sample. Therefore, the contribution of the lattice symmetry to the effective magnetic field is included in $\Psi_{\mu\nu}$. It is known that $\Psi_{\mu\nu}$ is zero when the crystal symmetry is cubic. Also, we should note that these considerations are based on the assumption that the sample is composed of a single domain magnetized in one direction. In a large sample with multiple domains, the demagnetizing field expressed by the third term in equation 1.16 is canceled in the bulk by the presence of the neighboring domains. This term is effective only on the surfaces where the neighboring domains are absent.

The magnetocrystalline anisotropy energy E_a per unit volume can be written as

$$E_a = K_1(\alpha_1^2\alpha_2^2 + \alpha_2^2\alpha_3^2 + \alpha_3^2\alpha_1^2 - 1/3) \tag{1.16}$$

where α_{1-3} are the direction cosines of the magnetization direction with respect to the $\langle 111 \rangle$ axes and K_1 is the magnetocrystalline anisotropy constant. For Fe_3O_4, K_1 is -1.1×10^4 J/m^3 [16]. E_a is minimum when the magnetization direction is parallel to one of the $\langle 111 \rangle$ axes which means that the easy magnetization is $\langle 111 \rangle$ axes. Figure 1.8 shows the bulk easy-magnetization axes of Fe_3O_4. There are four equivalent $\langle 111 \rangle$ axes ([111], $\left[1\bar{1}\bar{1}\right]$, $\left[\bar{1}1\bar{1}\right]$, and $\left[11\bar{1}\right]$), and the angle between each $\langle 111 \rangle$ axis is 109.5°.

Temperature Dependence

In the above discussion, we neglected the effect of the temperature. At 0 K, the spin is perfectly directed parallel to the external field and the magnetic moment of the atom can be written as $\boldsymbol{M} = 2\mu_B \boldsymbol{S}$ where μ_B is the Bohr magneton and $\boldsymbol{S}$ is the spin angular momentum. However, at a finite temperature, the magnetic moment of the atom is written by the thermal average. The magnetization of a paramagnetic N-atom system in an external field H can be written as

$$M(H,T) = \frac{N\left\{\sum_{M_S=-S}^{S}(-g_S\mu_B M_S)\exp(-g_S\mu_B H M_S/kT)\right\}}{\left\{\sum_{M_S=-S}^{J}\exp(-g_S\mu_B H M_S/kT)\right\}} \tag{1.17}$$

where M_S is the z-component of the total spin angular momentum S, N is the number of atoms in the system, g_S is the g-factor, k is the Boltzmann constant and T is the temper-

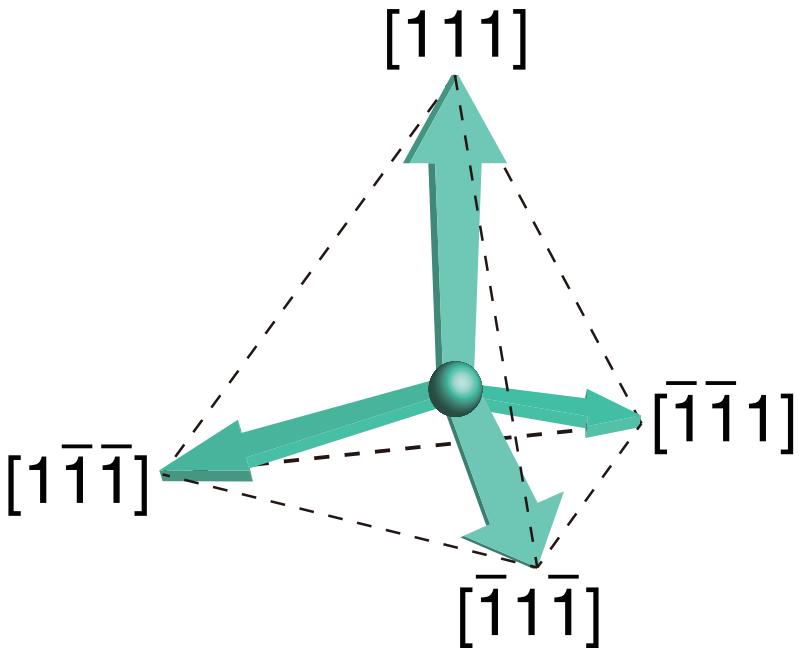

Figure 1.8: The room-temperature easy-magnetization axes of bulk Fe_3O_4.

ature. When $-g_S\mu_B H/kT \approx 1$, $M(HT)$ can be written, using the Brillouin function B_S, as

$$M(H,T) = Ng_S\mu_B S\, B_S\left(\frac{Jg_S\mu_B H}{kT}\right). \tag{1.18}$$

In the case of ferromagnetic and ferrimagnetic systems, the spin direction is determined not only by the external field but also by the exchange interaction with the neighboring spins. The exchange interaction can be taken into account by using a molecular field theory. In the presence of exchange interaction, the spin i feels a molecular field $H_m(i)$ given by

$$H_m(i) = -\frac{1}{g_S\mu_B}\sum_j 2J_{ij}\left\langle \boldsymbol{S}_j\right\rangle_{AV}, \tag{1.19}$$

where i and j are neighboring spins, $\boldsymbol{S}_j$ is the spin angular momentum of the site j, J_{ij} is the exchange constant, and $\left\langle \boldsymbol{S}_j\right\rangle_{AV}$ is the thermal average of $\boldsymbol{S}_j$. In the case of ferromagnetic materials, the thermal average of the spin momentum $\langle S_z\rangle_{AV}$,which determines the magnetization of the material, can be obtained by solving the self-consistent equation

$$\langle S_z\rangle_{AV} = -S\, B_s\left(\frac{\sum_j 2S\, J_{ij}\langle S_z\rangle_{AV}}{kT}\right). \tag{1.20}$$

In the case of ferrimagnetic materials which consist of two sites of magnetic atoms, the

molecular field is written, instead of equation 1.19, as

$$\begin{aligned} \boldsymbol{H_m}(A) &= -\lambda \boldsymbol{M_A} - \mu \boldsymbol{M_B} \\ \boldsymbol{H_m}(B) &= -\mu \boldsymbol{M_A} - \nu \boldsymbol{M_B} \end{aligned} \tag{1.21}$$

where $\boldsymbol{H_m}(A)$ and $\boldsymbol{H_m}(B)$ are the molecular field at the A and B site, respectively. $\boldsymbol{M_A}$ and $\boldsymbol{M_B}$ are the magnetic moments of the A and the B site, respectively. λ, μ and ν are the coefficients of the molecular field which reflect the exchange interaction. The thermal behavior of the magnetic moments $\boldsymbol{M_A}$ and $\boldsymbol{M_B}$ is largely dependent on the coefficients λ, μ and ν which reflect the exchange interaction.

1.1.3 Properties of the Fe_3O_4 (111) surface

It is known that the Fe_3O_4 surfaces have peculiar electronic properties. The Fe_3O_4 (001) surface exhibits a ($\sqrt{2} \times \sqrt{2}$) $R45^\circ$ superstructure and has a band gap [17]. Łodziana *et al.* pointed out that the surface electronic state of the Fe_3O_4 (001) surface has charge and orbital ordering which resembles the electronic state below the Verwey temperature [18]. Kurahashi *et al.* reported that the half-metallicity is lost on the Fe_3O_4 (001) surface [19]. Parkinson *et al.* reported that the band gap can be removed by atomic H exposure [2]. Furthermore, Kurahashi *et al.* found that the spin polarization is recovered by atomic H exposure [19]. They considered, based on the density-functional-theory (DFT) calculations, that the absence of half-metallicity is due to the hybridization of O $2p_x$, $2p_y$ orbitals with the Fe(B) $3d_{x^2-y^2}$ orbital. The similarity between the Fe_3O_4 (001) surface state and the Verwey transition and the changes in the electronic structure by H adsorption may indicate that the charge ordering occurs at higher temperature than the bulk on the Fe_3O_4 (001) surface, and that the surface charge ordering can be modulated by H adsorption.

Jordan *et al.* observed a band gap by STS on the Fe_3O_4 (111) surface at 140 K. At this temperature, the bulk is expected to be metallic at this temperature since the Verwey transition occurs at $\simeq$120 K. This indicates that the Verwey temperature is different from bulk on the Fe_3O_4 (111) surface. However, the origin of the band gap is still to be clarified, which may be due to the difficulties in preparing a well-defined stoichiometric Fe_3O_4 (111) surface.

The low-dimensionality of the surface also influences the magnetic structure. On surfaces, the demagnetizing field, written in the first term of equation 1.12 is dominant. The demagnetizing field gives rise to the magnetostatic energy. Magnetostatic energy originates from the magnetic poles at the surface. Here, we consider a periodic domain structure shown in figure 1.9 (a). The magnetostatic energy is written as

$$\begin{aligned} E_m &= \frac{\mu_0 M_s^2 \cos^2\theta L}{\pi^2} \times B, \\ B &= \sum_{n=1}^{\infty} \frac{1}{n^2 L} \int_0^d \sin n\left(\frac{\pi}{d}\right) x dx, \end{aligned} \tag{1.22}$$

where M_s is the spontaneous magnetization, θ is the angle between the magnetization direction and the surface-normal direction and L is the width of the domains. Equation

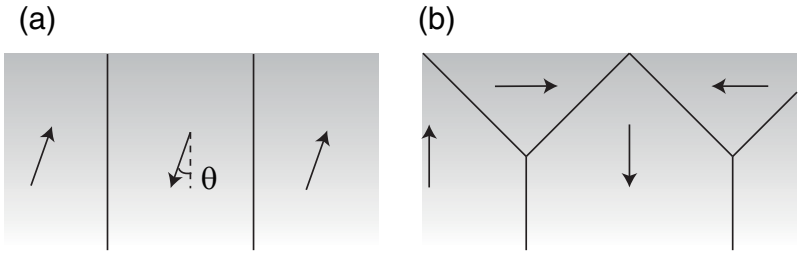

Figure 1.9: (a) A model of the magnetic domain structure without the closure domain and (b) the structure of closure domains.

1.22 can be written as

$$E_m = 8.53 \times 10^{-8} M_s^2 \cos^2 \theta L. \tag{1.23}$$

It seems, from equation 1.22, that $L = 0$ gives the minimum magnetostatic energy. However, making the domain size small will result in the increase in the amount of domain walls which will increase in the exchange energy. Therefore, the domain size L is determined by the compensation of the magnetostatic and the exchange energy. For magnetite, $M_s = 480$ kA/m and L is typically about 50 μm [20, 21].

Equation 1.22 also shows that the structure with smaller $\cos^2 \theta$ is energetically stable which means that the magnetization direction tends to be surface-parallel on the surface. As shown in figure 1.8, Fe_3O_4 has four easy-magnetization axes. One of the axes is perpendicular and the other three are non-perpendicular to the surface. Equation 1.22 indicates that the non-perpendicular magnetization axes are more preferable on the surface. This gives rise to a peculiar magnetic domain structure called the closure domain structure on the surface, which is illustrated in figure 1.9 (b). The surface is covered with the closure domains which are magnetized along the in-plane direction. The domains in the deeper region are magnetized along the surface-normal direction. The closure domains reduce the magnetostatic energy by closing the magnetic flux circuit. Özdemir *et al.* observed a triangle-shaped closure domain structure on the Fe_3O_4 $(1\bar{1}1)$ surface by the Bitter colloid technique, which is shown in figure 1.10. In their study, they also found, from the shape of the closure domains, that the magnetization direction of the closure domains is even more surface parallel. Again, this phenomenon is attributed to the magnetostatic energy. As shown in equation 1.22, the magnetostatic energy can be reduced by making the magnetization parallel to the surface. However, rotating the magnetization away from the original easy-magnetization axes costs magnetocrystalline anisotropy energy. Therefore, when the magnetocrystalline anisotropy energy is small, the magnetostatic energy rotates the magnetization of the closure domain to more surface-parallel direction than the original easy-axes. From a calculation that takes the magnetostatic energy, magnetoelastic energy and magnetocrystalline anisotropy energy, they estimated the angle θ between the magnetization direction and the [111] surface-normal direction as 2 °.

Peculiar magnetic structure has been also observed on Fe_3O_4 nanoparticles. Lima *et al.* [22] and Darbandi [23] reported that the spin direction of the Fe(A) and Fe(B) sites are non-collinear, which makes the saturation magnetization of the nanoparticles significantly smaller than that of the bulk. This may be due to the effect of the surface since the

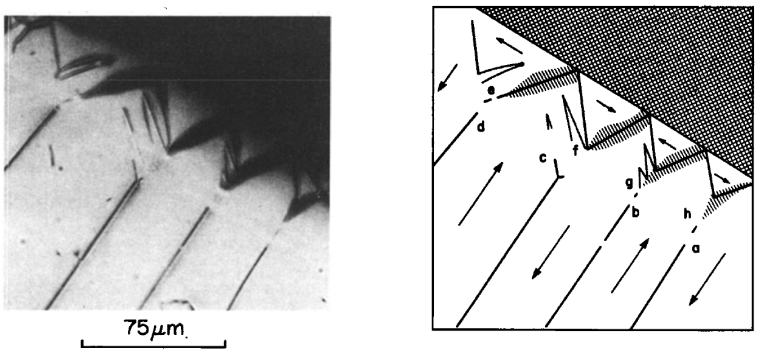

Figure 1.10: Closure domain patterns formed at the edge of the Fe_3O_4 single crystal where the (110) viewing plane intersects the (111) crystal surface [20]. The body domains are magnetized along the easy axis perpendicular to the $(1\bar{1}1)$ surface. The closure domains are magnetized along a direction more parallel to the $(1\bar{1}1)$ surface than the non-perpendicular easy magnetization axes.

contribution of the surface effect is larger in nanoparticles than larger samples. Krycka *et al.* observed the magnetic structure of Fe_3O_4 nanoparticles by polarization analyzed small angle neutron scattering (PASANS) and proposed a model shown in figure 1.11. In this model, the spin direction of the Fe(A) site near the surface deviates from the direction of the external field while that of the Fe(B) is directed along the external field. These results may indicate that the surface of Fe_3O_4 nanoparticles have large influence on the magnetic structure. However, for nanoparticles, it is difficult to prepare a well-defined stoichiometric sample, and the contribution of the size effect can not be excluded. Studies on the well-defined single crystal surface is necessary in order to clarify the effect of surfaces on the magnetic structure of Fe_3O_4.

1.2 Purpose of this study

The existence of band gap on the Fe_3O_4 (111) surface may indicate that the thermal behavior of the Verwey transition is different on the surface. There are two possible interpretations: the Verwey transition is inhibited or promoted on the (111) surface. Since the Verwey transition is a charge ordering transition, it is considered to be sensitive to the density of the Fe(B) t_{2g} electrons. We considered that the Verwey transition is influenced by the surface electronic states which may cause a change in the number of electrons in the Fe(B) t_{2g} state. We consider that the surface Verwey transition can be modulated by tuning the charge state of surface Fe(B) atoms. Therefore, the first purpose of this study is to clarify the electronic states of the Fe_3O_4 (111) surface and establish a method to modulate the charge state of the surface Fe(B) atoms by modifying the surface with atomic H and O_2.

Although Fe_3O_4 is a well-known ferrimagnet, the magnetic structure of the surface has not been clarified in detail since there are few methods that can directly probe the surface magnetic structure. As shown in sections 1.1.2, the magnetic structure and its thermal behaviors are largely dependent on the spin-orbis interaction and the exchange interaction

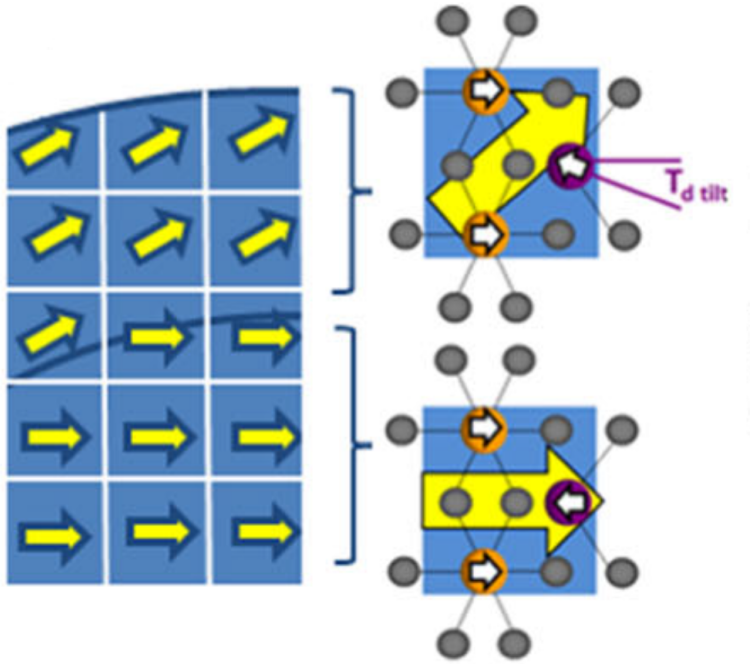

Figure 1.11: Near-edge section of a core-canted-shell model proposed by Krycka *et al.* [24]. Insets show constituent Fe(A) (purple) and Fe(B) (orange) sites; yellow arrows indicate the net local moments moments of these constituent Fe spins.

which may be different from the bulk on the surface. Since the electronic structure of the Fe_3O_4 (111) surface is different from the bulk, we can expect novel magnetic structure on the (111) surface. Based on these considerations, we aimed to clarify the magnetic structure and its thermal behavior of the Fe_3O_4 (111) surface.

Chapter 2

Experimental

2.1 Low-Energy Electron Diffraction

Low-energy electron diffraction (LEED) is a method that can probe the periodic structure of the surface by utilizing the diffraction of electrons. The de-Broglie wavelength λ of an electron with kinetic energy E can be written as

$$\lambda = \sqrt{\frac{h^2}{2m_0E}} \simeq \sqrt{\frac{150.4}{E}}(\text{Å}), \tag{2.1}$$

where h is the Planck constant and m_0 is the electron mass. In the LEED experiment, electron beam whose kinetic energy is 50 – 300 eV irradiates the sample. The de-Broglie wavelengths of these electrons are 1.78–0.72 Å. The electrons reflected by the surface interfere and form a diffraction pattern which reflects the information about the periodicity of the surface structure.

In the case of bulk sensitive diffraction experiments such as X-ray diffraction, the diffraction condition can be described using the reciprocal vectors. The reciprocal vectors can be written as

$$\vec{b_1} = 2\pi\frac{\vec{a_2}\times\vec{a_3}}{\vec{a_1}\cdot(\vec{a_2}\times\vec{a_3})}, \vec{b_2} = 2\pi\frac{\vec{a_3}\times\vec{a_1}}{\vec{a_2}\cdot(\vec{a_3}\times\vec{a_1})}, \vec{b_3} = 2\pi\frac{\vec{a_1}\times\vec{a_2}}{\vec{a_3}\cdot(\vec{a_1}\times\vec{a_2})} \tag{2.2}$$

where $\vec{a_1}$, $\vec{a_2}$ and $\vec{a_3}$ are the primitive translation vectors of the lattice, and $\vec{b_1}$, $\vec{b_2}$ and $\vec{b_3}$ are the reciprocal vectors. The reflected beam interferes constructively when the scattering vector K satisfies the Laue condition

$$\vec{K} = h\vec{b_1} + l\vec{b_2} + k\vec{b_3}, \tag{2.3}$$

where h, l and k are integers. In the case of LEED, however, the diffraction is sensitive to the surface because the mean-free-path of the low-energy electrons is 1–100 Å. In the case of the cubic lattice, for example, the (001) surface is perpendicular to $\vec{a_3}$. If we assume that all the electrons are reflected at the first layer of the surface, the reciprocal vector of the (001) surface can be written as

$$\vec{b_1} = 2\pi\frac{\vec{a_2}\times\vec{n}}{|\vec{a_1}\times\vec{a_2}|}, \vec{b_2} = 2\pi\frac{\vec{n}\times\vec{a_1}}{|\vec{a_1}\times\vec{a_2}|} \tag{2.4}$$

where $\vec{n}$ is the unit vector normal to the surface. Equation 2.4 shows that, in the case

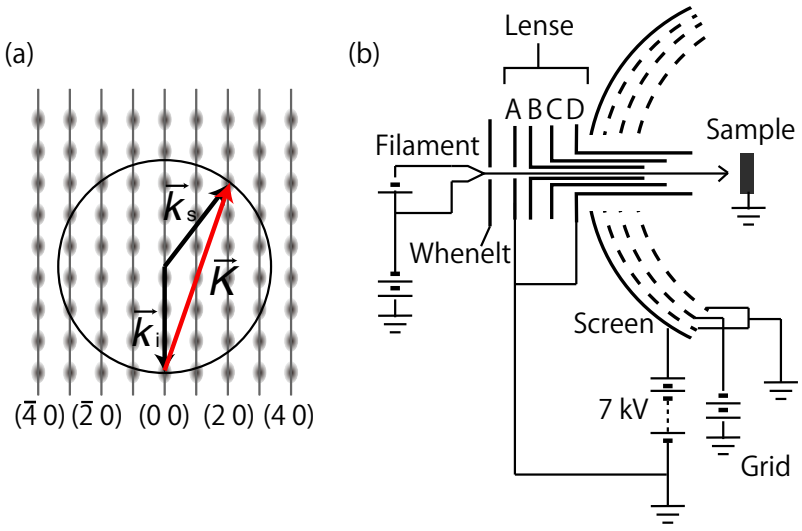

Figure 2.1: (a) A typical example of the Ewald construction of a quasi two-dimensional system and (b) the schematic view of a LEED apparatus. $\vec{k_i}$ is the wave vector of the incident wave, $\vec{k_s}$ is the scattered wave vector, and $\vec{K}$ is the scattering vector.

of two-dimensional systems, the reciprocal lattice is rod-shaped. Figure 2.1 (a) shows a typical example of the Ewald construction. The scattered wave $\vec{k_s}$ interferes constructively when the both ends of the scattering vector $\vec{K}$ coincide with the intersection of the Ewald sphere and the reciprocal rod.

To be precise, the structure along the surface-normal direction cannot be neglected because the mean-free-path of the electrons is a finite value. This gives rise to the dependence of the diffraction intensity on the incident electron energy which is called the I-V curve. The I-V curve contains information about the structure along the surface-normal direction. However, the I-V curve cannot be analyzed by the kinematic theory which takes into account only the single-scattering event and the Laue condition because the multiply-scattered electron also contribute to the diffraction intensity. Three-dimensional structure can be determined from the I-V curve by simulation of the multiple-scattering process on a structure model. The calculation includes the calculation of the phase shift of the scattered wave for each atom using the Muffin-tin potential, the calculation of scattering process within a single atomic layer, and finally the inter-layer multiple scattering. The calculation result is compared with the experiment result of the I-V curve in order to improve the structural model.

Figure 2.1(b) shows the schematic view of the LEED apparatus. The thermal electrons emitted from the tungsten filament are accelerated by the voltage applied to the filament, and focused onto the sample surface by the Whenelt and the lenses. The reflected electrons include the elastically scattered electrons which contribute to the diffraction spots, and inelastically scattered electrons which are observed as the background. The inelastic electrons, which have lower energy than the primary energy, are removed by the two grids. Only the elastically scattered electrons are accelerated by the screen voltage and observed as a LEED pattern.

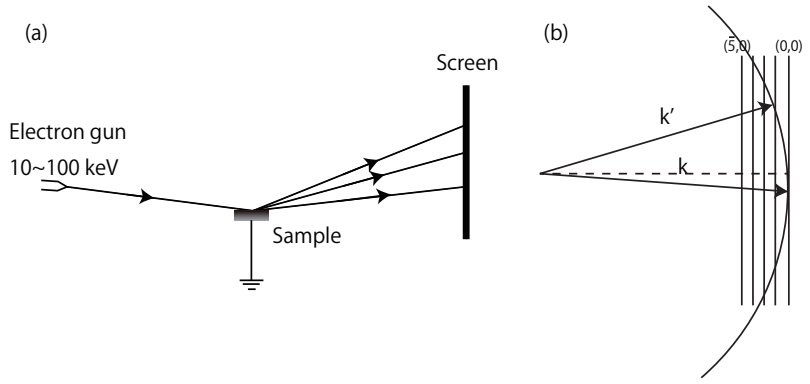

Figure 2.2: (a) The schematic illustration of the RHEED setup and (b) the corresponding Ewald construction.

2.2 Reflection High Energy Electron Diffraction

Reflection high energy electron diffraction (RHEED) is also a technique that probes the surface periodic structure by the diffraction of electrons. The energy of the incident electron is more than 10 keV, which is much higher than that of LEED. Although the mean-free-path of the high-energy electrons is larger than that of the low-energy electrons, the surface sensitivity of RHEED is similar to that of LEED since the electrons are incident under a grazing angle so that the penetrating depth of the electrons will be small compared to the mean-free-path. Figure 2.2 (a) shows the schematic illustration of the RHEED setup. The electrons with the energy of 10–100 keV are incident onto the sample under grazing angles (3°–5°) and the diffracted beam is observed by the fluorescent screen. Figure 2.2(b) illustrates the Ewald construction of the RHEED geometry. Because of the high electron energy, the Ewald sphere is much larger than that of LEED. The reciprocal rod and the Ewald sphere are smeared out due to the disturbance of the surface periodicity and to the spread of the incident beam, respectively. Thus the RHEED pattern consists of streaks which corresponds to the reciprocal rod intersected by the Ewald sphere.

2.3 Ultraviolet Photoemission Spectroscopy

Ultraviolet photoemission spectroscopy is a method used to investigate the electron density-of-states near the Fermi level and the work function. When electromagnetic wave irradiates the surface, it excites electrons which will be emitted from the surface as photo-electrons. By measuring the energy spectrum of the photo-electrons, we can obtain information about the electronic state inside the solid. Figure 2.3 (a) basic principle of UPS. The principle of UPS is often explained by the three-step model which consists of three independent processes.

- Optical excitation of an electron from an initial state to the final state inside the crystal.
- Propagation of the electron to the surface.

- Emission of the electron to the vacuum.

The first step is an electric dipole transition whose transition probability can be described by the golden-rule transition probability:

$$W_{fi} = \frac{2\pi}{\hbar} |\langle f, \boldsymbol{k}| H' |i, \boldsymbol{k}\rangle|^2 \delta(E_f(\boldsymbol{k}) - E_i(\boldsymbol{k}) - \hbar\omega) \tag{2.5}$$

where H' is the perturbation Hamiltonian, and $\langle f, \boldsymbol{k}|$ and $|i, \boldsymbol{k}\rangle$ are the wave functions of the final and the initial state. $E_f(\boldsymbol{k})$, $E_i(\boldsymbol{k})$ and $\hbar\omega$ are the energy of the final state, initial state, and the incident photon, respectively. The full Hamiltonian is given by

$$\begin{aligned} H &= H_0 + H' && (2.6)\\ &= H_0 + \frac{e}{2mc}(\boldsymbol{A}\cdot\boldsymbol{P} + \boldsymbol{P}\cdot\boldsymbol{A}) - e\Phi + \frac{e^2}{2mc^2}|A|^2, && (2.7) \end{aligned}$$

where H_0 is the original Hamiltonian without perturbation, $\boldsymbol{P}$ is the momentum operator,Φ is the scalar potential, and $\boldsymbol{A}$ is the vector potential. $|A|^2$ is small enough to be neglected. By choosing a gauge where $\Phi = 0$, the cross-section $\frac{d\sigma}{d\Omega}$ of the optical excitation can be written as

$$\frac{d\sigma}{d\Omega} \propto |\langle f, \boldsymbol{k}| \boldsymbol{A}\cdot\boldsymbol{P} + \boldsymbol{P}\cdot\boldsymbol{A} |i, \boldsymbol{k}\rangle|^2 \delta(E_f(\boldsymbol{k}) - E_i(\boldsymbol{k}) - \hbar\omega) \tag{2.8}$$

$$H = \frac{e}{2mc}(\boldsymbol{A}\cdot\boldsymbol{P} + \boldsymbol{P}\cdot\boldsymbol{A}). \tag{2.9}$$

The vector potential $\boldsymbol{A}$ can be written as

$$\boldsymbol{A} = \boldsymbol{A}_0 \exp(-i\omega t - i\boldsymbol{q}\cdot\boldsymbol{r}) \tag{2.10}$$

where $\boldsymbol{A}_0$ is the amplitude vector, $\boldsymbol{q}$ is the incident wave vector, and $\boldsymbol{r}$ is the position vector. Using the commutation relation $[\boldsymbol{A}, \boldsymbol{P}] = -i\hbar\nabla\cdot\boldsymbol{A}$, equation 2.8 can be written as

$$\frac{d\sigma}{d\Omega} \propto |\langle f, \boldsymbol{k}| 2\boldsymbol{A}\cdot\boldsymbol{P} - i\hbar\nabla\cdot\boldsymbol{A} |i, \boldsymbol{k}\rangle|^2 \delta(E_f(\boldsymbol{k}) - E_i(\boldsymbol{k}) - \hbar\omega). \tag{2.11}$$

We neglect the term $-i\hbar\nabla\cdot\boldsymbol{A}$ for simplicity. We should note that it cannot be neglected at the surface where $\boldsymbol{A}$ is discontinuous due to the difference of the dielectric constant of the solid and the vacuum. In addition, $\boldsymbol{A}$ can be regarded as a constant when the wave length of the incident light (58.4 nm in the case of He I) is large enough compared to the atomic distance. Then, the cross-section $\frac{d\sigma}{d\Omega}$ can be written as

$$\frac{d\sigma}{d\Omega} \propto |\langle f, \boldsymbol{k}| \boldsymbol{P} |i, \boldsymbol{k}\rangle \cdot \boldsymbol{A}_0|^2 \delta(E_f(\boldsymbol{k}) - E_i(\boldsymbol{k}) - \hbar\omega). \tag{2.12}$$

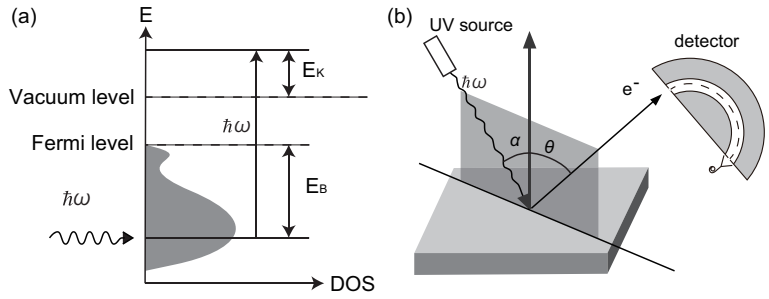

Figure 2.3: (a) A schematic illustration of the principle of the ultra-violet photoemission spectroscopy and (b) the schematic view of the UPS setup.

Using the commutation relation $[H_0, r] = -i(\hbar/2m)\boldsymbol{P}$, equation 2.12 can be written as

$$\frac{d\sigma}{d\Omega} \propto |\langle f, \boldsymbol{k}|\boldsymbol{r}|i, \boldsymbol{k}\rangle \cdot \boldsymbol{A}_0|^2 \delta(E_f(\boldsymbol{k}) - E_i(\boldsymbol{k}) - \hbar\omega). \tag{2.13}$$

This equation means that the perturbation Hamiltonian of the optical excitation is almost identical to the position operator or the electric dipole moment operator. The cross section is strongly dependent on the the symmetry of the initial and the final state.

The second step of the three-step model is the propagation of the excited electron to the surface. During this step, some of the electrons are inelastically scattered. These electrons lose the information of the energy of the initial state and can be observed in the spectrum as the background in the low-energy region.

The third step is the emission of electrons to the vacuum. Due to the two-dimensional periodicity of the surface, the momentum of the emitted electron satisfies

$$k_{ex,\parallel} = k_{f,\parallel} + G_{\parallel} \tag{2.14}$$

where $k_{ex,\parallel}$ and $k_{f,\parallel}$ are the in-plane components of the momentum of the emitted electron and the electron in the final state, respectively. $G_{\parallel}$ is an in-plane reciprocal vector. The information about the perpendicular component $k_{f,\perp}$ of the final state is lost during the third step due to the interaction with the surface potential. Using equation 2.14 and the energy conservation law, we can determine the momentum and the binding energy of the initial state from the measured energy and the emission direction of the photo-electron.

Since only the electrons whose energies are larger than the surface potential barrier can be observed as photoelectrons, the work function can be estimated from the minimum of the energy of the photoelectrons. The work function is estimated by

$$\Phi_{WF} = \hbar\omega - (E_{FL} - E_{cutoff}) \tag{2.15}$$

where E_{FL} and E_{Cutoff} are the energy of the photo-electron excited from the Fermi level and the lowest energy of the observed photo-electrons.

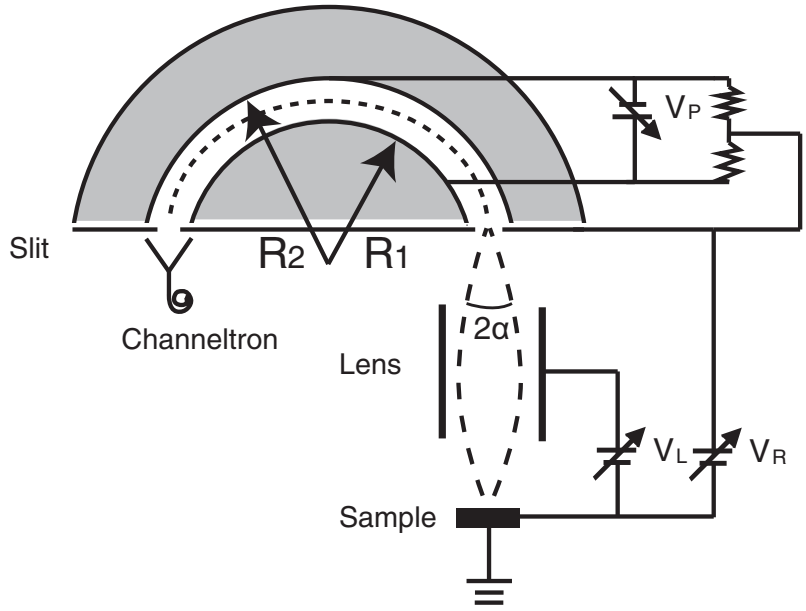

Figure 2.4: The schematic view of the hemispheric electron energy analyzer.

Measurement System

Figure 2.3 (b) shows the schematic view of the experimental setup of UPS. The incident light is the He I line (21.22 eV) produced by the helium discharge lamp. The He I light is produced when an electron excited to the 2p orbital de-excite to the 1s orbital. The energy of the photoelectrons is analyzed by the hemispheric electron energy analyzer. Figure 2.4 shows the schematic view of the hemispheric electron energy analyzer. The photoelectrons emitted from the surface are focused by the electric lens and introduced into the energy analyzer through the slit. The electrons that passed through the hemisphere are detected by a channeltron. The analyzer is composed of two hemispheres whose radii are R_1 and R_2 ($R_1 < R_2$). Voltage V_p is applied between the two hemispheres so that only the electrons with energy E_p can pass through the hemisphere. The energy E_p is written as

$$E_p = \frac{eV_p}{R_2/R_1 - R_1/R_2}, \tag{2.16}$$

and the energy resolution is given by

$$\Delta E = \left(\frac{\omega}{R_1 + R_2} + \alpha^2 \right) E_p \tag{2.17}$$

where ω is the width of the slit and α is the acceptance angle of the incoming photoelectrons. It is possible to obtain the energy spectra by sweeping V_p, but it also changes the energy resolution. Therefore, V_p is usually fixed. Instead, the slit and the hemisphere are biased to V_R, so that it is possible to resolve the electron energy without changing the resolution.

Figure 2.5 shows the sample holder used in the UPS experiments. The sample is fixed

on a molybdenum plate with tantalum jigs. The molibdenum plate is fixed to the copper plate which is thermally connected to the cryostat. The sample can be cooled down to 110 K with liquid nitrogen and warmed up to more than 1100 K by electron bombardment. The sample holder was mounted on the Vacuum Generator ESCA LAB II system which is composed of a ultra-high vacuum (UHV) chamber, a helium discharge lamp, an ion gun, an X-ray source (Al Kα line), and a hemispheric electron energy analyzer. The base pressure was $\sim 1 \times 10^{-10}$ mbar.

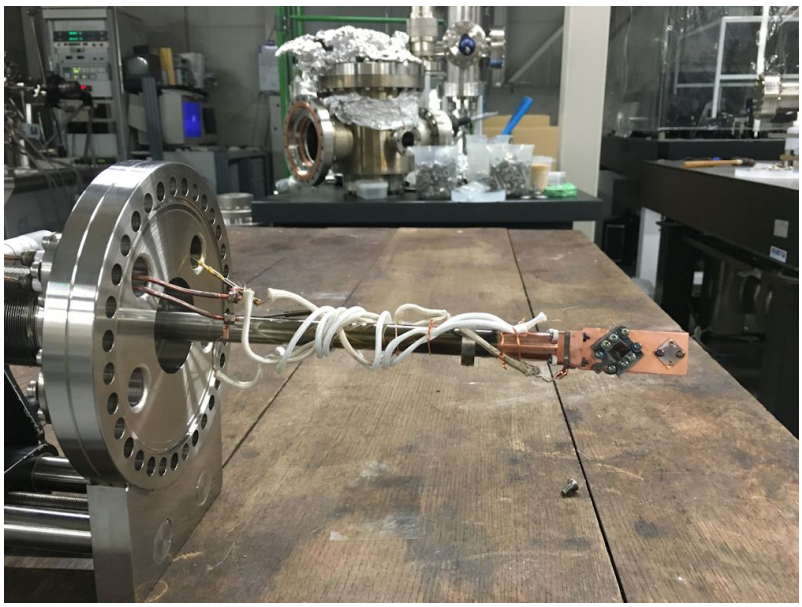

Figure 2.5: The sample holder used for the UPS and XPS experiments.

2.4 X-ray Photoemission Spectroscopy

X-ray photoemission spectroscopy is the method to investigate the electronic states by measuring the energy of the photoelectrons emitted by irradiating X-ray to the surface. XPS differs from UPS in that it can measure the binding energy of core-level electrons because the incident photon energy is much higher than UPS. From the kinetic energy of the observed photo-electrons, we can calculate the binding energy of the electrons in the initial state. From the binding energy of core level electrons, we can identify the chemical composition of the material. By carefully observing the binding energy, we can obtain the information about the chemical environment. In the Hartree-Fock approximation, one can define the single-electron binding energy of a particular electron state. The single-electron binding energy is determined by the electrostatic potential of the nucleus and the other $(N-1)$ electrons. When an electron is emitted from an N-electron system by photoexcitation, the remaining $(N-1)$ electrons relaxes. The energy E_{gain} that the emitted electron gains is written by

$$E_{gain} = \hbar\omega + (E_N - E_{N-1}) \tag{2.18}$$

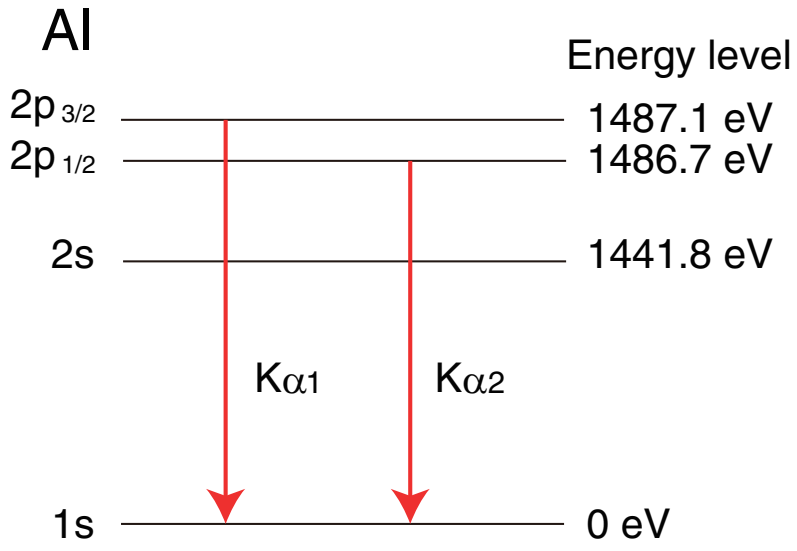

Figure 2.6: The energy structure of Al nuclei. The red arrows represent the Kα lines.

where $\hbar\omega$, E_N and E_{N-1} are the incident photon energy, total energy of the initial N-electron state, and the total energy of the final $(N-1)$-electron state. $(E_N - E_{N-1})$ includes the one-electron binding energy and the relaxation energy of the remaining $(N-1)$ electrons. Therefore, relaxation energy is transfered to the emitted electron. If we take the vacuum level for the origin of the energy axis, the kinetic energy of photo-electrons will be written as

$$E_k = E_{gain} - \phi \tag{2.19}$$

where ϕ is the work function. The chemical environment of the atoms determines the local electrostatic potential and the relaxation energy of the remaining $(N-1)$ electrons. Therefore, the kinetic energy of the photoelectrons provide information about the chemical environment.

2.4.1 Experimental Apparatus

X-ray Source

In the present study, the Al Kα line was used as the incident X-ray. Figure 2.6 shows the schematic illustration of the Al Kα transition. When a hole is generated in the 1s state of Al atoms by electron bombardment, electrons in the 2p state deexcite to the 1s state and emits X-ray. The 2p state is split into $2p_{3/2}$ and $2p_{1/2}$ states by spin-orbit interaction. The transitions from the $2p_{3/2}$ and $2p_{1/2}$ to the 1s state are called the Kα_1 and Kα_2 line, respectively. The the transition energy of the Kα_1 and Kα_2 line are 1487.1 eV and 1486.7 eV, respectively [25]. The transition between 1s and 2s is forbidden due to the selection rule of the electric dipole transition. There is also the transition between $3p$ and $1s$ (Kβ), but its intensity is about 1/100 of the Kα line.

Figure 2.8 shows the schematic illustration of the X-ray source. Thermal electrons are emitted from the negatively biased tungsten filament and are accelerated towards the

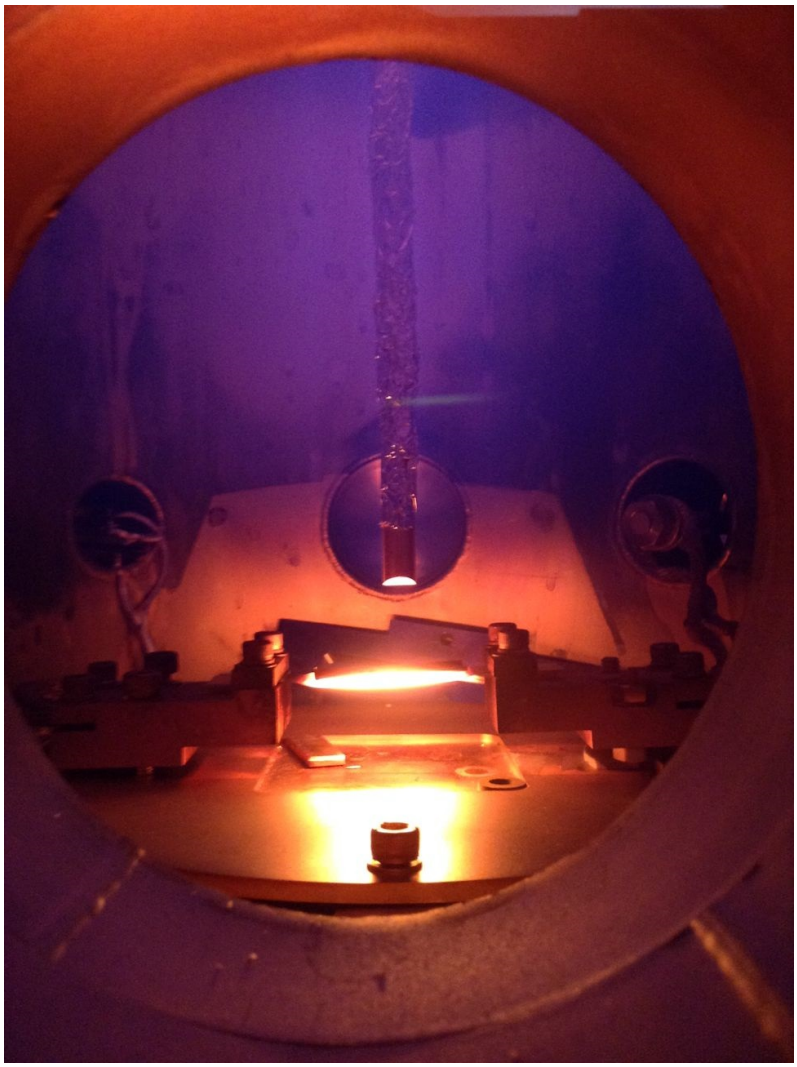

Figure 2.7: The experimental setup for ion plating.

target anodes which is biased to $\sim$ 10 kV. The target anode is made of copper and its tip is coated with Al which is deposited by ion plating. The target anode is cooled by water in order to avoid melting of the anode.

Ion Plating

The target of the X-ray source is irradiated to the electron beam during the measurement. Therefore, the deposited Al layer should be thermally connected more tightly to the copper anode than the normal vapor deposition since the Al layer deposited by normal vapor deposition will easily be evaporated and removed by the electron irradiation. In order to avoid this, the target material (Al) was deposited on the copper anode by ion plating. Figure 2.7 shows the experimental setup for ion plating. Al was evaporated from the electrically heated tungsten boat in the Ar partial pressure of 5–7 Pa. The Cu anode was biased to about -600 V and the distance between the Cu anode and the tungsten boat was 30–40 mm.

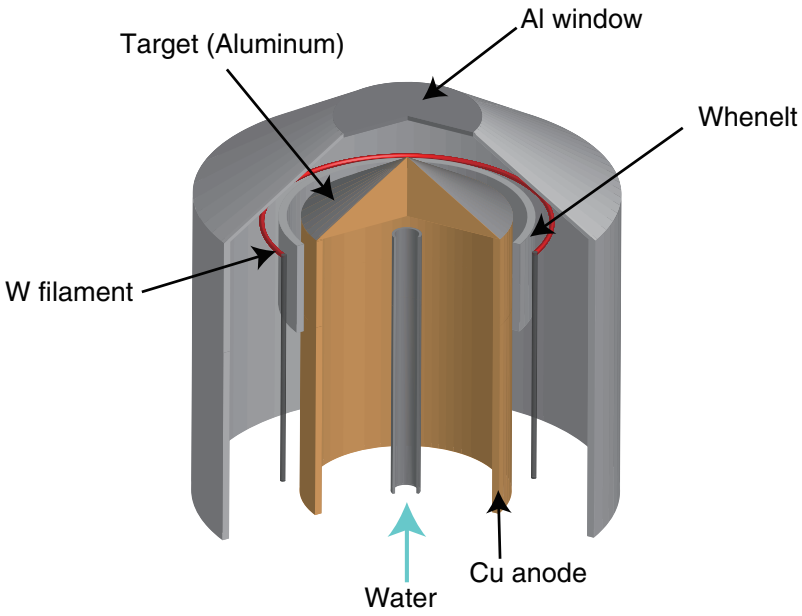

Figure 2.8: Schematic illustration of the X-ray source

2.4.2 Observed Binding Energies of Various Materials

Table 2.1 shows the observed binding energy of various materials [26]. The energy values shown in the table are the center of the range of energies exhibited by various chemical states of each element.

2.5 Transport Measurement with Micro Four-point Probe

The four-probe method is a technique to measure the conductivity of the sample. Figure 2.9 shows the schematic illustration of the 4-point probe measurement. A current is made flow between the outer two probes by a current source, and the voltage between the inner probes is measured with a voltmeter with the impedance large enough compared to the resistance of the sample. The resistance R of the sample is obtained by $R = V/I$ where I is the current flowing between the outer probes and V is the measured voltage between the inner probes.

As shown in figure 2.9, the current flows not only through the surface but also through the subsurface layer and the bulk. Generally, it is difficult to separate the contributions from these three channels. In many cases the surface electronic state causes changes in the electronic transport properties of the sub-surface region with a finite thickness, examples of which are the space-charge layer of semiconductor surfaces and the semi-conducting surface states on metal surfaces. In order to measure the conductivity of the surface and the subsurface, the contribution from the bulk should be as small as possible. One approach to this problem is to minimize the pitch of the probes [27]. As shown in figure 2.9, the contribution from the surface and subsurface region to the conductivity can be enhanced by making the probe spacing as small as the thickness of the subsurface layer

Table 2.1: Binding energy of various materials observed by Al Kα XPS [26].

Element	Observed Binding Energy (eV)							
	1s	2s	$2p_1$	$2p_3$	3s	$3p_1$	$3p_3$	Auger Lines
C	287							993
O	531	23						779,764,743
Cr		698	586	577	77	46	45	767,729
Fe		847	723	710	93	56	55	659,608,553
Ni		1009	873	855	112	69	67	548,542,482,476,410,393
Cu		1098	954	934	124	79	77	486,479,416,408,396,337,317

Element	Observed Binding Energy (eV)								
	3s	$3p_1$	$3p_3$	$3d_3$	$3d_5$	4s	$4p_1$	$p4_3$	Auger Lines
Mo	508	413	396	233	230	65	38		1068,1033

Element	Observed Binding Energy (eV)										
	4s	$4p_1$	$4p_3$	$4d_3$	$4d_5$	$4f_5$	$4f_7$	5s	$5p_1$	$5p_3$	Auger Lines
Ta	566	464	403	241	229	27	25	71	45	37	
W	594	491	425	257	245	36	34	77	47	37	

where the effect of the surface electronic states is large.

Experimental Apparatus

In this study, we used a micro four-point probes manufactured by capres A/S. Figure 2.10 is a photomicrography of the micro four-point probe. The probe pitch is 10 μm, and the width and the length of the probes is 6 μm and 30 μm, respectively.

The micro four-point probe is attached to the probe holder shown in figure 2.11 which is composed of a probe socket, a fine piezoelectric positioner and a coarse piezoelectric positioner. The maximum travel of the fine positioner is 24 μm. The coarse positioner can move by up to 6 mm by applying a saw-tooth wave voltage with the amplitude of 60 V. The four-point probe is approached to the sample by the coarse and fine positioners. The contact between the probe and the sample is detected by measuring the resistance between the probe and the sample.

Figure 2.12 shows the measurement unit of the micro four-point probe measurement. The sample is fixed to a sample holder composed of molybdenum and copper plates. The sample holder is fixed to the coldhead which can be cooled down with liquid nitrogen or helium. The sample temperature can be controlled by the heater attached to the coldhead.

The sample plate can be removed from the measurement unit with a transfer rod. The sample preparation is carried out in the preparation unit attached next to the measurement chamber equipped with a sputter ion gun and a tungsten filament for electron bombardment heating.

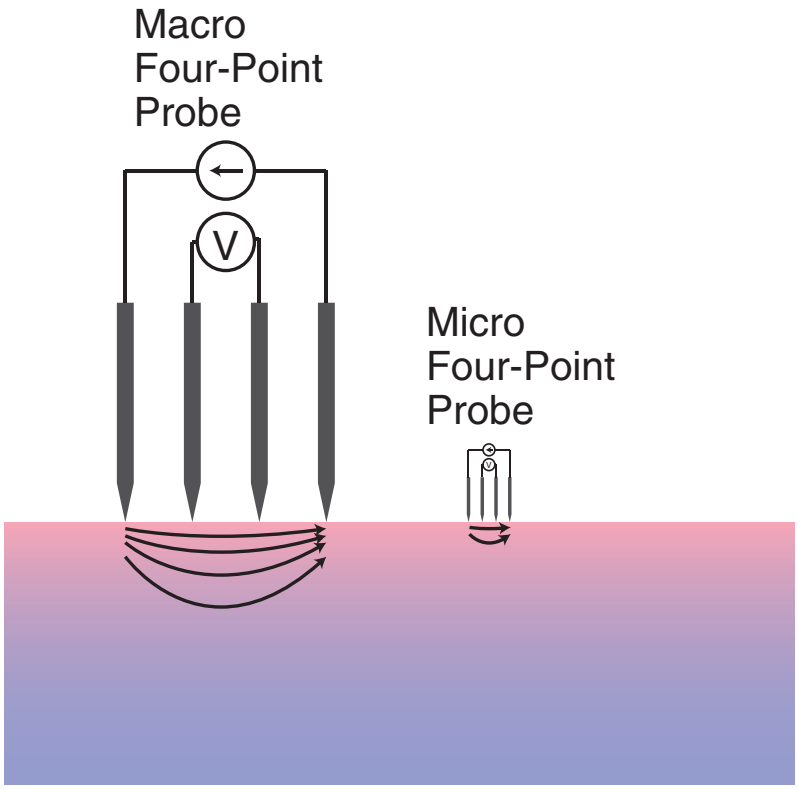

Figure 2.9: Schematic illustration of a four-point probe measurement. A constant current is made flow between the outer two probes and the voltage between the inner probes is measured. The measured conductance includes contribution from the surface, the subsurface, and the bulk regions. The contribution from the bulk region can be reduced by making the probe spacing small.

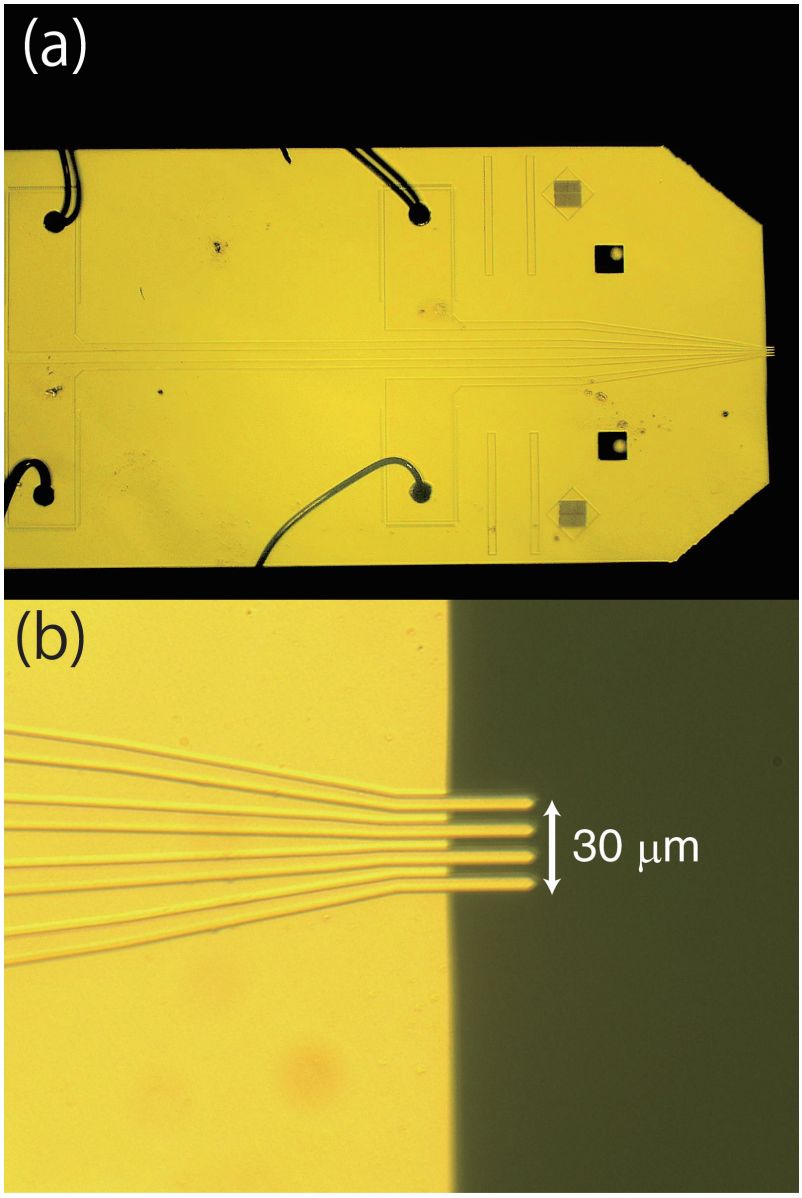

Figure 2.10: (a) the photomicrograph of the micro four-point probe and (b) the enlarge view of the tip of the electrodes.

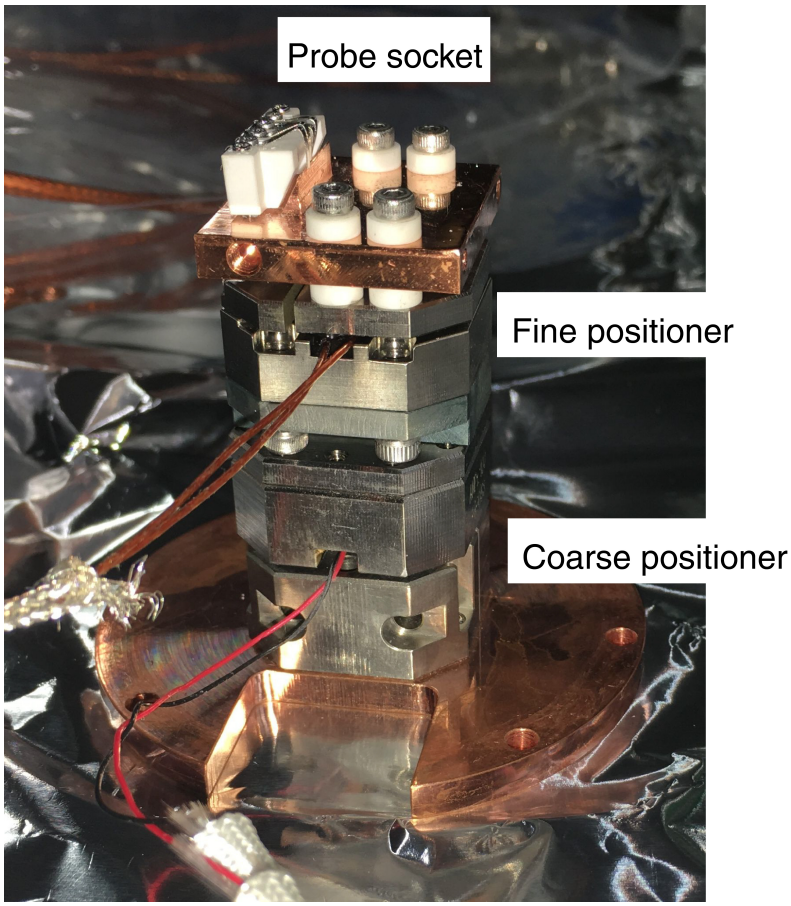

Figure 2.11: A picture of the measurement unit of the micro four-point probe measurement.

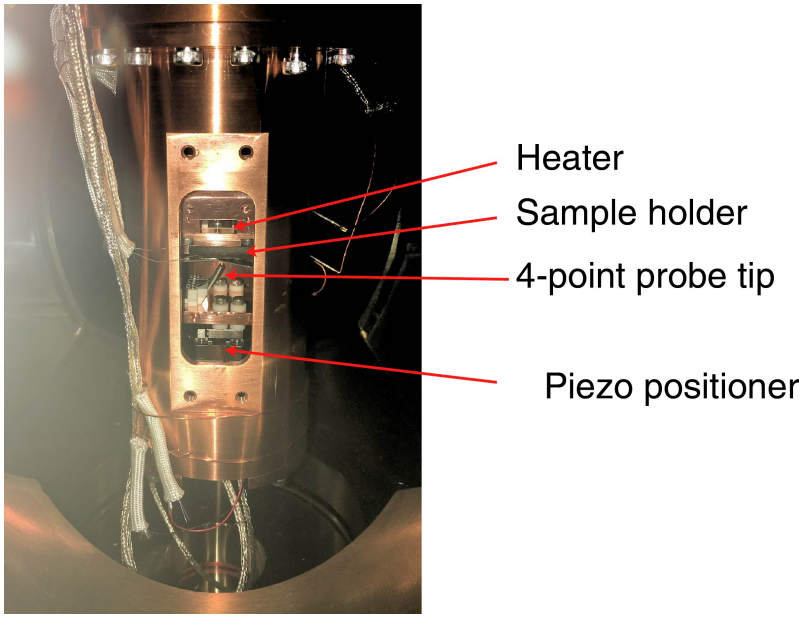

Figure 2.12: The measurement unit of the micro four-point probe measurement

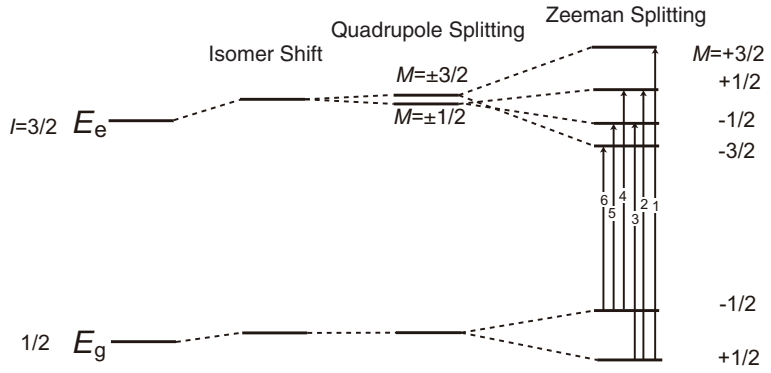

Figure 2.13: The energy structure of the ^{57}Fe nuclei.

2.6 Conversion Electron Mössbauer Spectroscopy

Conversion Electron Mössbauer Spectroscopy (CEMS) is a technique to obtain information about the internal magnetic field, the chemical environment, and the electric field gradient by measuring the energy spectrum of the nuclear excitation. The energy levels of the ^{57}Fe nuclei are influenced by the internal magnetic field, chemical environment, and the electric quadrapole interaction [28].

2.6.1 Hyperfine Structure

Figure 2.13 shows the nuclear level of ^{57}Fe nuclei. The nuclear spin quantum number I is $1/2$ for the ground state and $3/2$ for the first excited state. The energy difference between the ground state and the excited state is 14.413 keV. The energy of each level is weakly influenced by the chemical environment, electric field gradient, and internal magnetic field. These interactions are called the hyperfine interaction and the resulting energy shift of the nuclear levels is called the hyperfine structure. The chemical environment causes a shift of the ground and excited states, which is called the Isomer shift. In the presence of electric field gradient, the excited state splits into the $M = \pm 1/2$ and $M = \pm 3/2$ states, which is called the quadrupole splitting. In the presence of the internal magnetic field, all the M states of the ground and excited states are split, which is called the Zeeman splitting.

Isomer Shift

If we neglect the size of the nucleus, the electrostatic interaction of the nucleus with the electrons can be estimated by regarding the nucleus as a point charge. However, if we take the size of the nucleus into account, the electrostatic interaction will depend on the density of electrons inside the nucleus. Here, we assume that the charge density $e\rho(\boldsymbol{r_n})$ of the nucleus satisfies $\rho(\boldsymbol{r_n}) \neq 0$ for $R > \boldsymbol{r_n}$ and $\rho(\boldsymbol{r_n}) = 0$ for $\boldsymbol{r_n} \geq R$, where $\boldsymbol{r_n}$ is the position vector and R is the radius of the nucleus. $\boldsymbol{r_n} = 0$ corresponds to the center of the nucleus. If the function $\rho(\boldsymbol{r_n})$ is spherically symmetric, the interaction between the electron at $r_e \geq R$ and the nucleus is identical to the value estimated by the point-charge model. Here, $\boldsymbol{r_e}$ is the position vector of the electron. Therefore, the difference between the point-charge

model and the finite-radius model is attributed to the electrostatic interaction between the nucleus and the electrons at $\boldsymbol{r_e} < R$. The difference of the energy ΔE estimated by the two models is

$$\Delta E = -e^2 \int \int_{0 \leq r_n, r_e \leq R} \frac{\rho_n(r_n)\rho_e(r_e)}{|\boldsymbol{r}_n - \boldsymbol{r}_e|} d^3\boldsymbol{r}_n d^3\boldsymbol{r}_e - \left(-Ze^2 \int_{0 \leq r_e \leq R} \{\frac{\rho_e(r_e)}{r_e}\} d^3\boldsymbol{r}_e \right) \tag{2.20}$$

where $r_e = |\boldsymbol{r}_e|$, $r_n = |\boldsymbol{r}_n|$, and Z is the total charge of the nucleus given by

$$Z = \int \rho_n(r_n) d^3\boldsymbol{r}_n. \tag{2.21}$$

The spacial distribution of $\rho_e(r_e)$ at $r_e \leq R$ can be neglected because R is much smaller than the radius of the electron orbit. Therefore, we use the approximation $\rho_e(r_e) \simeq |\psi(0)|^2$, where $\psi(r)$ is the wave function of the electron. Based on this approximation, ΔE can be written as

$$\begin{aligned} \Delta E &= \frac{2\pi}{3} Ze^2 |\psi(0)|^2 \left\langle r_n^2 \right\rangle, \\ \left\langle r_n^2 \right\rangle &= \frac{1}{Z} \int r_n^2 \rho_n(r_n) d^3\boldsymbol{r}_n. \end{aligned} \tag{2.22}$$

$\left\langle r_n^2 \right\rangle$ corresponds to the radius of the charge distribution of the nucleus. ΔE is always larger than zero, which can be explained in the following way; If an electron is located inside the nucleus and its distance of the nucleus is r_e ($\geq R$), only the nuclear charge density $\rho_n(r_n)$ inside the sphere with the radius r_e contributes to the potential that the electron feels. Therefore the amount of the nuclear charge that contribute to the electron inside the nuclear is less than the total amount of nuclear charge. If we neglect the size of the nucleus, on the other hand, all the nuclear charge contribute to the potential of the electrons regardless of the position of the electron. Therefore, the total electrostatic energy in the finite-radius model is smaller than that of the point-charge model.

Here, we can see that ΔE depends on $|\psi(0)|^2$ and $\left\langle r_n^2 \right\rangle$. The electron density $|\psi(0)|^2$ depends on the chemical condition, which makes the excitation energy of the $^{57}Fe^{2+}$ and $^{57}Fe^{3+}$ different. $\left\langle r_n^2 \right\rangle$ depends on the energy level of the nucleus. This makes the size of the isomer shift of the ground and the excited states different, as shown in figure 2.13.

Electric Quadrupole Splitting

The shape of the nuclei is not a perfect sphere and the charge density of the nuclei has angular dependence. However, since the nuclei has finite angular momentum even at the ground state, the observed charge distribution of the nuclei is averaged over the time. It is known that, in the case of $I = 0$ and $I = 1/2$ state, the averaged charge distribution is spherically symmetric. For $I \geq 1$, the charge distribution lacks spherical symmetry.

Let us consider the electrostatic energy of a nucleus in an electrostatic field generated by the electrons. The electrostatic potential $V(x, y, z)$ satisfies

$$\nabla^2 V(x, y, z) = 0. \tag{2.23}$$

The Taylor series expansion of $V(x, y, z)$ is written as

$$V(x,y,z) = V(0,0,0) + x\frac{\partial V}{\partial x}\bigg|_0 + y\frac{\partial V}{\partial y}\bigg|_0 + z\frac{\partial V}{\partial z}\bigg|_0 \tag{2.24}$$

$$+ \quad \frac{1}{2}\left(x^2\frac{\partial^2 V}{\partial x^2}\bigg|_0 + y^2\frac{\partial^2 V}{\partial y^2}\bigg|_0 + z^2\frac{\partial^2 V}{\partial z^2}\bigg|_0\right) + \ldots \tag{2.25}$$

where $\frac{\partial V}{\partial x}\big|_0$ means the value at $(x, y, z) = (0, 0, 0)$. Here, we defined the x, y, and z axis so that they satisfy

$$\frac{\partial^2 V}{\partial x \partial y}\bigg|_0 = \frac{\partial^2 V}{\partial y \partial z}\bigg|_0 = \ldots = 0. \tag{2.26}$$

We assume that the x and y axes are geometrically identical;

$$\frac{\partial^2 V}{\partial x^2}\bigg|_0 = \frac{\partial^2 V}{\partial y^2}\bigg|_0 . \tag{2.27}$$

From the equation 2.23, we obtain

$$\frac{\partial^2 V}{\partial x^2}\bigg|_0 = \frac{\partial^2 V}{\partial y^2}\bigg|_0 = -\frac{1}{2}\frac{\partial^2 V}{\partial z^2}\bigg|_0 . \tag{2.28}$$

The electrostatic energy H_{el} can be written as

$$\begin{aligned} H_{el} &= \int e\rho_n(\boldsymbol{r})V(\boldsymbol{r})d^3\boldsymbol{r} \\ &= \int e\rho_n(\boldsymbol{r})V(0,0,0)d^3\boldsymbol{r} + \int e\rho_n(\boldsymbol{r})\left(x\frac{\partial V}{\partial x}\bigg|_0 + y\frac{\partial V}{\partial y}\bigg|_0 + z\frac{\partial V}{\partial z}\bigg|_0\right)d^3\boldsymbol{r} \\ &+ \int e\rho_n(\boldsymbol{r})\left(\frac{1}{2}\left(x^2\frac{\partial^2 V}{\partial x^2}\bigg|_0 + y^2\frac{\partial^2 V}{\partial y^2}\bigg|_0 + z^2\frac{\partial^2 V}{\partial z^2}\bigg|_0\right)\right)d^3\boldsymbol{r} \end{aligned} \tag{2.29}$$

where $\rho_n(\boldsymbol{r})$ is the charge density at the position $\boldsymbol{r}$. The first term does not depend on the shape of the nucleus. It is known that, within the experimental error, the nucleus has no electric dipole moment, which means that $\rho_n(\boldsymbol{r})$ satisfies $\rho_n(\boldsymbol{r}) = \rho_n(-\boldsymbol{r})$. The second term of the equation 2.29 is 0 because $\rho_n(\boldsymbol{r})$ is an even function and $\left(x\frac{\partial V}{\partial x}\big|_0 + y\frac{\partial V}{\partial y}\big|_0 + z\frac{\partial V}{\partial z}\big|_0\right)$ is odd with respect to $\boldsymbol{r}$. Therefore, the most contributing factor is the third term. Using the equation 2.28, H_{el} can be written as

$$H_{el} = \frac{1}{2}\frac{\partial^2 V}{\partial z^2}\bigg|_0 \cdot \frac{1}{2}e\int(2z^2 - x^2 - y^2)\rho(\boldsymbol{r})d^3\boldsymbol{r} \tag{2.30}$$

The charge distribution $\rho_n(\boldsymbol{r})$ depends on I and its z-component I_z. Here, we define the electric quadrupole moment Q as

Table 2.2: The parameters required for the derivation of the Zeeman splitting [29].

μ_0	μ_N	μ_B	$g_N(I = 1/2)$	$g_N(I = 3/2)$
$4\pi \times 10^{-7}$	5.05×10^{-27} J/T	9.27×10^{-24} J/T	0.180	-0.103

$$Q = \int (3z^2 - r^2) \cdot \rho_{n,I_z=I}(\boldsymbol{r}) d^3\boldsymbol{r} \tag{2.31}$$

where $\rho_{n,I_z=I}(\boldsymbol{r})$ is the charge distribution of the nuclei in the $I_z = I$ state. Q depends on I. The equation 2.30 can be written as

$$H_{el} = \frac{1}{2} \left.\frac{\partial^2 V}{\partial z^2}\right|_0 \cdot \frac{eQ}{I(2I-1)} \cdot \frac{1}{2}\{3I_z^2 - I(I+1)\}. \tag{2.32}$$

By defining the electric field gradient q as $eq = \left.\frac{\partial^2 V}{\partial z^2}\right|_0$, equation 2.32 can be simplified as

$$H_{el} = e^2 qQ \cdot \frac{3I_z^2 - I(I+1)}{4I(2I-1)}. \tag{2.33}$$

This shows that the size of quadrupole interaction of the nuclei depends on the electric field gradient and I_z^2. In the case of ^{57}Fe, the $I = 3/2$ state is split into two levels consisting of $I_z = \pm 3/2$ states and $I_z = \pm 1/2$ states as shown in figure 2.13.

Zeeman Splitting

The Zeeman splitting is due to the interaction between the nuclear spin and the electron spins which can be written as

$$\begin{aligned} H_1 &= \mu_0 g_e \mu_B \boldsymbol{s} \cdot \mathrm{rot}(\boldsymbol{\mu} \times \frac{\boldsymbol{r}}{r^3}) \\ &= \mu_0 g_e \mu_B \{(\boldsymbol{s} \cdot \nabla)(\boldsymbol{\mu} \cdot \nabla) - (\boldsymbol{s} \cdot \boldsymbol{\mu})\nabla^2\}(\frac{1}{r}). \end{aligned} \tag{2.34}$$

where g_e is the g-factor of electrons, μ_B is the Bohr magneton of the electron, $\mu_B \boldsymbol{s}$ is the magnetic moment of the electron spin, $\boldsymbol{r}$ is the position of the electron, and $\boldsymbol{\mu}$ is the magnetic moment of the nucleus. The size of the magnetic moment μ of the nucleus can be written as

$$\mu = g_N \mu_N I \tag{2.35}$$

where g_N is the g-factor of the nucleus, μ_N is the nuclear Bohr magneton of the nucleus, and I is the nuclear spin quantum number. The values used here are listed in table 2.2. μ_N is about $1/2000$ of the electron Bohr magneton because the mass of the nucleus is larger than that of the electron. In the case of ^{57}Fe, the values of g_N of the $I = 1/2$ ground state and $I = 3/2$ excited states have opposite sign. This explains why the states with larger M are energetically more stable for the ground states while, for the first excited states, states

with smaller M are more stable. H_1 can be written as

$$H_1 = \frac{8\pi}{3}\mu_0 g_N \mu_N g_e \mu_B((\boldsymbol{s}\cdot\boldsymbol{I})\delta(\boldsymbol{r}) - 2\mu_B\{\frac{(\boldsymbol{s}\cdot\boldsymbol{I})}{r^3} - \frac{3(\boldsymbol{I}\cdot\boldsymbol{r})(\boldsymbol{s}\cdot\boldsymbol{r})}{r^5}\}) \tag{2.36}$$

The second term corresponds to the dipole interaction with electrons at $r \neq 0$. The first term, which is called the Fermi contact interaction, is a contribution from the electrons whose wave functions satisfy $\psi(r = 0) \neq 0$. Since only s electrons satisfy this condition, the Fermi contact interaction depends on the density of s electrons at $r = 0$. The density of s electrons are spin-polarized due to the exchange interaction with the d electrons which give rise to the magnetic moment of the atom. Therefore, the internal magnetic field, which originates from the Fermi contact interaction, is parallel to the magnetic moment of the atom, which means that the quantization axis of the nucleus is parallel to the magnetic moment of the atom.

2.6.2 Magnetic Dipole Transitions

The magnetic dipole transition is a transition that is induced by the interaction of nucleus with the magnetic field of the electrostatic wave. Heitler *et al.* showed that the only the transitions with the change of the angular momentum $\Delta I = 0, \pm 1$ are allowed in the magnetic dipole transition. CEMS and NRS utilize the magnetic dipole transition between the $I = 1/2$ and the $I = 3/2$ states. The excitation (or de-excitation) probability of the magnetic dipole transition is given by

$$H_{f,i} \propto \left|\left\langle \Psi_f \left| g_N \mu_N \boldsymbol{I}\cdot\boldsymbol{B}\cos(\omega t)\right|\Psi_i\right\rangle\right|^2, \tag{2.37}$$

where Ψ_i and Ψ_f are the wave function of the initial and the final state, respectively, $\boldsymbol{B}$ is the magnetic field of the incident (emitted) X-ray, and ω is the frequency of the X-ray. If the quantization axis of the nuclear spin is parallel to the z axis, I_x and I_y can be written as

$$\begin{aligned} I_x &= \frac{I_+ + I_-}{2} \\ I_y &= \frac{I_+ - I_-}{2i} \end{aligned} \tag{2.38}$$

where I_+ and I_- are the raising and lowering operators. This indicates that the operator $\boldsymbol{I}\cdot\boldsymbol{B}$ mixes the two states with $\Delta M = \pm 1$ when $\boldsymbol{B}$ is not parallel to the quantization axis. When $\boldsymbol{B}$ is parallel to the quantization axis, M is the eigenvalue of the operator $\boldsymbol{I}\cdot\boldsymbol{B}$, which means that the transition between two states with different M is forbidden. To summarize, the selection rule of the magnetic dipole transition requires that the change of magnetic quantum number M is 0 or ± 1. In the case of ^{57}Fe, there are six allowed transition lines as shown in figure 2.13. These transitions are labeled as transitions 1 to 6 in order of the transition energy. The transitions 1 and 4 correspond to the $\Delta M = 1$ transitions, transitions 2 and 5 correspond to $\Delta M = 0$, and transitions 3 and 6 correspond

to the $\Delta M = -1$ transitions. When the magnetic field of the incident beam is parallel to the nuclear spin, only the $\Delta M = 0$ transitions are allowed and the $\Delta M = \pm 1$ transitions are forbidden. This gives rise to the dependence of line intensities on the nuclear spin directions relative to the magnetic field of the incident (or emitted) γ-ray, which is utilized in CEMS and NRS for the measurement of the magnetization direction.

Since the intensity of the magnetic dipole transition depends on the angle between the polarization of the incident γ-ray and the magnetization direction, the relative intensities of the transition $1-6$ depend on the magnetization direction of the sample. The relative intensities of the transitions $1-6$ are written as

$$\begin{aligned} W_1 = W_6 &= 3(1+\cos^2\theta_e)/2, \\ W_3 = W_4 &= (1+\cos^2\theta_e)/2, \\ W_2 = W_5 &= 2\sin^2\theta_e, \end{aligned} \tag{2.39}$$

where W_{1-6} is the relative intensity of transitions $1-6$ and θ_e is the angle between the magnetization direction and the X-ray incident direction. In case the sample is uniaxially magnetized, θ_e is the angle between the magnetization direction and the incident ray.

2.6.3 Mössbauer Effect

When an isolated ^{57}Fe nucleus decays from the $I = \frac{3}{2}$ state to the $I = \frac{1}{2}$ state, the momentum conservation law requires the nucleus to recoil since the emitted γ-ray has a momentum. Therefore, the energy of the emitted γ-ray is slightly smaller than the transition energy between the $I = \frac{1}{2}$ and $I = \frac{3}{2}$ states. The same phenomenon occurs when a γ-ray excites an isolated ^{57}Fe nucleus. The energy loss due to the recoil is written as [30]

$$R = \frac{\hbar^2\omega^2}{2c^2M}, \tag{2.40}$$

where R is the energy loss, $\hbar\omega$ is the energy of the emitted (absorbed) γ-ray, and M is the mass of the nucleus. In the case of ^{57}Fe nuclei, R is 1.95×10^{-3} eV which is much larger than the hyperfine splitting width of the ground and excited states. However, when the ^{57}Fe nucleus is trapped in a crystal, there is a possibility that the momentum is absorbed not by the single nucleus but by the whole crystal. In this case, the mass M in equation (2.40) is extremely large which makes the energy loss R negligible. This phenomenon is called the recoilless emission (absorption). The ratio P of the recoilless emission (absorption) to all the emission (absorption) can be written as [30]

$$P = \exp\left(\frac{-3R}{k\theta}\left[\frac{1}{4} + \left(\frac{T}{\theta}\right)^2 \int_0^{\theta/T} \frac{x}{e^x - 1} dx\right]\right), \tag{2.41}$$

where k is the Boltzmann constant and θ is the Debye temperature. The band width of the γ-ray emitted by the recoilless emission is approximately 4.7×10^{-9} eV [31], which is narrow enough to probe the hyperfine structure.

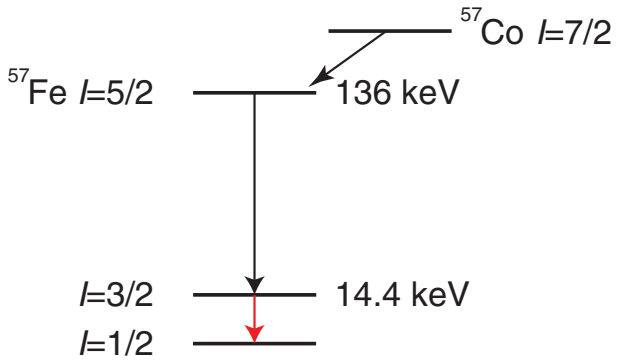

Figure 2.14: The energy diagram of the decay process of ^{57}Co nuclei.

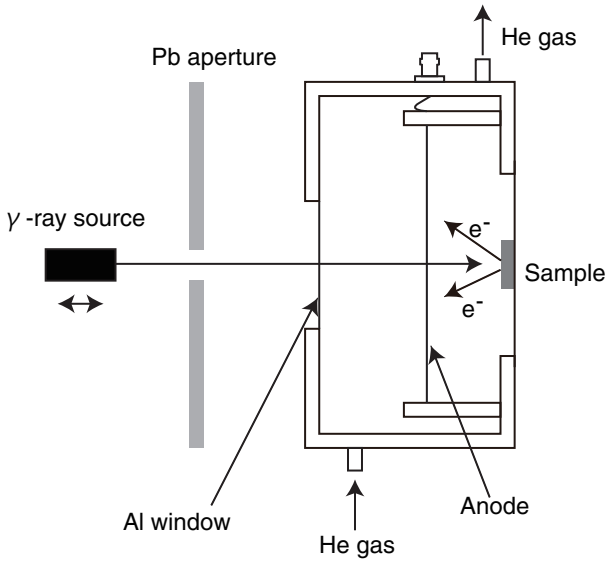

Figure 2.15: The schematic illustration of the measurement system of CEMS.

2.6.4 Measurement Systems

In CEMS, ^{57}Fe nuclei are excited by the γ-ray emitted from a ^{57}Co source. The decay process of ^{57}Co nuclei is shown in figure 2.14.The unstable ^{57}Co nuclei decay to ^{57}Fe $I = \frac{5}{2}$ state, which decay to $I = \frac{3}{2}$ state. Subsequently, the $I = \frac{3}{2}$ state decays to the $I = \frac{1}{2}$ state, emitting a 14.413 keV γ-ray or conversion electrons. Conversion electrons are the electrons that are emitted by the internal conversion which is a kind of the nuclear decay whose decay energy is transfered to the electron.

The energy of the incident γ-ray can be varied by moving the γ-ray source at various speeds. Moving the ^{57}Co γ-ray source at 1 cm/sec, for example, causes the Doppler shift of $\simeq$480 neV which is comparable with the size of hyperfine splitting of Fe_3O_4. When the energy of the γ-ray coincides with one of the transition lines of the target nuclei, the target will be excited to the $I = \frac{3}{2}$ state. The excited nuclei de-excite and release the energy in two ways. One is to emit a γ-ray and the other is to emit electrons which is called conversion electrons. CEMS utilizes the conversion electrons in order to detect the transition.

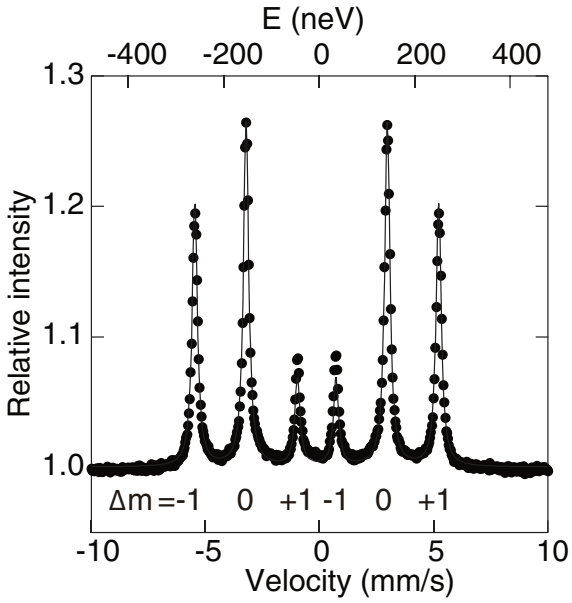

Figure 2.16: Conversion electron Mössbauer spectroscopy taken for ^{57}Fe film of 20 nm grown on SiO_2/Si(111) [32].

Figure 2.15 shows the schematic illustration of the CEMS measurement system. The sample is mounted in a chamber which is filled with mixed gas consisting of 90% helium and 10% methane. The conversion electron is detected by the proportional counter in which a gold wire biased to ~1.2 kV detects the conversion electrons.

Figure 2.16 shows a CEMS spectrum of a ^{57}Fe film of 20 nm grown on SiO_2/Si(111). The 6 peaks correspond to the transition 1 to 6 from the right side of the spectrum. The horizontal axis is the speed of the γ-ray source. The background signal is mainly due to the photoelectrons. Taking one spectrum takes about one week.

2.7 Nuclear Resonant X-ray Scattering

2.7.1 Theory

Nuclear resonant X-ray Scattering (NRS) is also a spectroscopic technique that utilizes the Mössbauer effect, but it differs from CEMS in that it measures the scattering of X-ray[33, 34, 35, 36, 37]. Also, since synchrotron radiation is used as the incident X-ray, the smallest available energy width of the incident X-ray is several meV which is larger than the size of the hyperfine structure. Therefore, the six excitations, shown in figure 2.13, occur simultaneously. The excited state is a collective excitation described as the coherent superposition of various excited states of all the nuclei of the crystal [38]. The photons emitted by the de-excitation interfere which results in the formation of quantum beats in the time spectra.

The intensities of the excitation lines have polarization dependence due to the selection rules of the magnetic dipole transition [39]. Let us consider the scattering of linearly-polarized X-ray with its electric field parallel to the surface as shown in figure 2.17. The

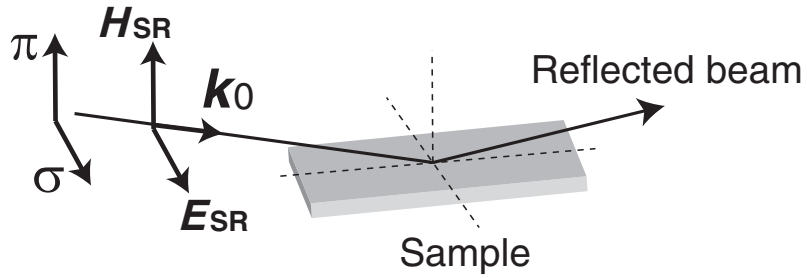

Figure 2.17: A typical geometry used in nuclear resonant scattering. $\boldsymbol{k}_0$ denotes the wavevector of the incident X-ray.

time-dependent scattering intensity $I(t)$ is described as [37]

$$\begin{aligned} I(t) &= \left\{ |[N]_{\sigma\sigma}|^2 + |[N]_{\sigma\pi}|^2 \right\} \chi^2 e^{-\chi t/\tau_0}, \qquad (2.42) \\ [N]_{\sigma\sigma} &= \frac{3}{16\pi} \left[F_{+1} + F_{-1} + (\boldsymbol{\pi}\cdot\boldsymbol{m})^2 (2F_0 - F_{+1} - F_{-1}) \right], \\ [N]_{\sigma\pi} &= \frac{3}{16\pi} \left[-i (\boldsymbol{k_0}\cdot\boldsymbol{m}) (F_{+1} - F_{-1}) - (\boldsymbol{\sigma}\cdot\boldsymbol{m}) (\boldsymbol{\pi}\cdot\boldsymbol{m}) (2F_0 - F_{+1} - F_{-1}) \right], \end{aligned}$$

with

$$\begin{aligned} F_{\Delta M} &= \int_{-\infty}^{\infty} f_{\Delta M}(\omega) e^{i\omega t} d\omega, \qquad (2.43) \\ f_{\Delta M}(\omega) &\propto \frac{2\pi f_{LM}\Gamma_0}{k_0(1+\alpha)(2I_g+1)} \sum_{m_i} \frac{C^2(I_g 1 I_e; m_i \Delta M)}{\hbar(\omega - \omega_{m_i \Delta M}) + i\Gamma_0/2}, \end{aligned}$$

where m_i is the magnetic quantum number of the initial state, ΔM is the change of the magnetic quantum number due to the excitation, N is the nuclear scattering length, τ_0 is the natural life time, $\boldsymbol{\pi}$ is the surface-normal unit vector, $\boldsymbol{k_0}$ is the incident wavevector, $\boldsymbol{\sigma}$ is the unit vector perpendicular to $\boldsymbol{k_0}$ and parallel to the surface, $\boldsymbol{m}$ is the unit vector parallel to the magnetization direction, I_g and I_e are the nuclear spins of the ground and excited states, f_{LM} is the Lamb-Mössbauer factor, Γ_0 is the natural linewidth of the transition, and α is the coefficient of internal conversion. $F_{\Delta M}$ is the intensity contribution corresponding to the transition with change of magnetic quantum number ΔM. The sum runs over all the ground state levels with magnetic quantum numbers m_i. $\omega_{m_i \Delta M}$ is the resonance energy of the magnetic quantum numbers m_i and $m_i + \Delta M$. $C(I_g 1 I_e; m_i \Delta M)$ is the Clebsch-Gordan coefficient given in the notation of Rose [37]. $[N]_{\sigma\sigma}$ corresponds to the probability that the nuclei absorb $\boldsymbol{\sigma}$-polarized X-ray and emit $\boldsymbol{\sigma}$-polarized γ-ray, and $[N]_{\sigma\pi}$ is the probability that the nuclei absorb $\boldsymbol{\sigma}$-polarized X-ray and emit $\boldsymbol{\pi}$-polarized γ-ray.

Equation 2.43 can be written as

$$F_0 = \frac{1}{3}\left(e^{i\omega_2 t} + e^{i\omega_5 t}\right) e^{-t/2\tau_0},$$

$$
\begin{aligned}
F_{+1} &= \left(e^{i\omega_1 t} + \frac{1}{3}e^{i\omega_4 t}\right)e^{-t/2\tau_0}, \\
F_{-1} &= \left(e^{i\omega_6 t} + \frac{1}{3}e^{i\omega_3 t}\right)e^{-t/2\tau_0},
\end{aligned} \tag{2.44}
$$

where ω_{1-6} is the frequency of the γ-ray corresponding to the deexcitation lines 1-6 shown in figure2.13. χ is the factor that reflects the speedup effect which is given by

$$
\chi = \frac{1}{4}\rho\sigma_0 f_{LM}|t_{02}|^2\frac{d}{\phi}, \tag{2.45}
$$

where ρ is the density of ^{57}Fe atoms, $|t_{02}|^2$ is the relative intensity of the standing wave resulting from the superposition of the incident and the reflected beam, d is the penetration depth of the evanescent field, and ϕ is the glancing angle. σ_0 is the nuclear absorption cross section at resonance [37].

The time-dependent intensity $I(t)$ consists of two main frequency components, $\omega_6 - \omega_1$, $\omega_4 - \omega_1 (= \omega_6 - \omega_3 = \omega_5 - \omega_2)$, and $\omega_3 - \omega_1 (= \omega_6 - \omega_4)$ which are labeled as $\omega_{1,6}$, $\omega_{2,5}$, and $\omega_{1,3}$, respectively. Figure 2.18 shows the dependence of the intensity of frequency components of the time spectra on the azimuthal angle of the incident beam. The relationship between the incident angle and the observable frequency component can be confirmed by equations 2.42 and 2.44. If $\boldsymbol{m}$ is perpendicular to the surface ($\boldsymbol{m} \parallel \boldsymbol{\pi}$), equation 2.42 becomes

$$
\begin{aligned}
I(t) &\propto |2F_0|^2\chi^2 e^{-\chi t/\tau_0} \\
&= \left\{\left|\frac{2}{3}e^{i\omega_2 t} + \frac{2}{3}e^{i\omega_5 t}\right|^2 e^{-t/\tau_0}\right\}\chi^2 e^{-\chi t/\tau_0}.
\end{aligned} \tag{2.46}
$$

This shows that the frequency component $\omega_{2,5}$ is observed and $\omega_{1,6}$ and $\omega_{1,3}$ are absent when $\boldsymbol{m} \parallel \boldsymbol{\pi}$. If $\boldsymbol{m}$ is parallel to the electric field of the incident X-ray ($\boldsymbol{m} \parallel \boldsymbol{\sigma}$), equation 2.42 becomes

$$
\begin{aligned}
I(t) &\propto |F_{+1} + F_{-1}|^2\chi^2 e^{-\chi t/\tau_0} \\
&= \left\{\left|\left(e^{i\omega_1 t} + e^{i\omega_6 t}\right) + \frac{1}{3}\left(e^{i\omega_3 t} + e^{i\omega_4 t}\right)\right|^2 e^{-t/\tau_0}\right\}\chi^2 e^{-\chi t/\tau_0}.
\end{aligned} \tag{2.47}
$$

In this case, all the three frequency components ($\omega_{1,6}$, $\omega_{2,5}$, and $\omega_{2,5}$) are present. If $\boldsymbol{m}$ is parallel to the incident wavevector $\boldsymbol{k}_0$,

$$
\begin{aligned}
I(t) &= \left\{|\,[N]_{\sigma\sigma}\,|^2 + |\,[N]_{\sigma\pi}\,|^2\right\}\chi^2 e^{-\chi t/\tau_0}, \\
[N]_{\sigma\sigma} &= \frac{3}{16\pi}\left[F_{+1} + F_{-1}\right], \\
&\propto \left[\left(e^{i\omega_1 t} + \frac{1}{3}e^{i\omega_4 t}\right) + \left(e^{i\omega_6 t} + \frac{1}{3}e^{i\omega_3 t}\right)\right]e^{-t/2\tau_0} \\
[N]_{\sigma\pi} &= \frac{3}{16\pi}\left[-iF_{+1} + iF_{-1}\right].
\end{aligned}
$$

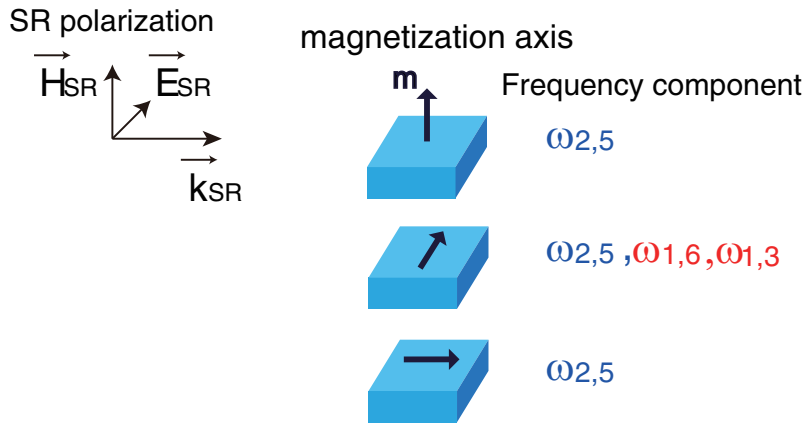

Figure 2.18: The relationship of the quantum-beat frequencies with the SR polarization and the magnetization direction.

$$\propto \left[e^{\frac{\pi i}{2}} \left(e^{i\omega_1 t} + \frac{1}{3} e^{i\omega_4 t} \right) + e^{\frac{-\pi i}{2}} \left(e^{i\omega_6 t} + \frac{1}{3} e^{i\omega_3 t} \right) \right] e^{-t/2\tau_0} \tag{2.48}$$

This shows that the scattered γ-rays with frequencies ω_1, ω_4 and ω_3, ω_6 are circularly polarized and their directions are opposite to each other. This means that the γ-rays with frequencies ω_1 and ω_6 (and also ω_3 and ω_4) do not interfere. Therefore, frequency component $\omega_{1,6}$ and $\omega_{1,3}$ are not observed. The interference between the γ-rays with frequencies ω_1 and ω_4 (or ω_3 and ω_6) is present because these waves have the same direction of circular polarization. This interference is observed as the component $\omega_{2,5}$ because the energy difference between the deexcitation line 1 and 4 (or 3 and 6) is identical to that of the deexcitation line 2 and 5.

These considerations are briefly summarized in the figure 2.18. If there is an in-plane magnetic anisotropy, the intensity of the $\omega_{1,6}$ component will vary with incident azimuthal angle, as shown in figure 2.18. Therefore, by observing the time spectra with various incident directions, we can detect the in-plane magnetic anisotropy.

As an example of azimuthal angle dependence of the frequency component of a sample with in-plane magnetic anisotropy, we show in figure 2.19 the NRS time spectra and the frequency spectra of ^{57}Fe film (20 nm) on ^{57}Fe$_x$Si$_{1-x}$/Si(111) with five azimuthal angles [32]. The peaks at 69–62 MHz and 124 MHz correspond to the $\omega_{2,5}$ and $\omega_{1,6}$ component, respectively. The quantum-beat frequency of 124 MHz are observed only when the incident direction is parallel to the $[1\bar{1}0]$ and $[1\bar{2}1]$ axis, indicating that the magnetization is mainly directed to $[\bar{1}12]$ direction.

Another advantage of NRS is that it can be used with grazing geometry. The probing depth of NRS, which is determined by the penetrating depth of the evanescent field, depends on the glancing angle. The penetrating depth of the evanescent field at the total-reflection angle is about 1 nm[40, 32]. Therefore, the probing depth of NRS is approximately 1 nm while that of CEMS is 45–60 nm which is determined by the escape length of the conversion electrons[28, 41, 42].

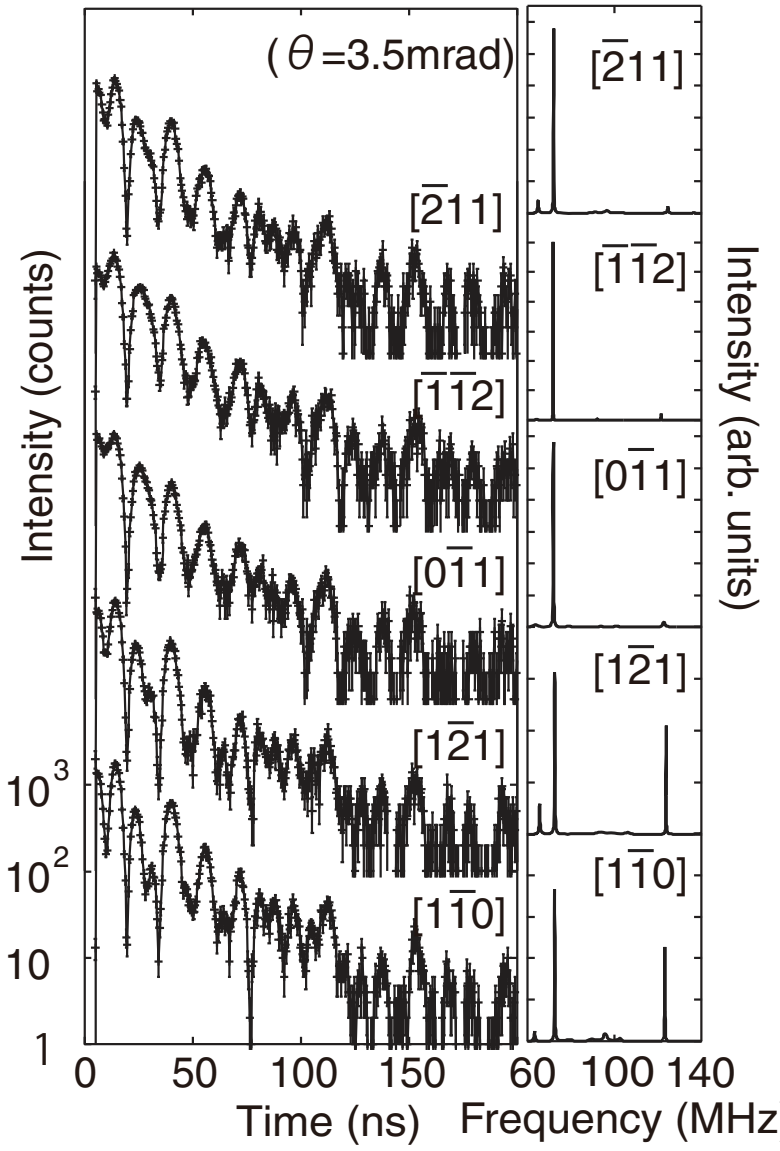

Figure 2.19: The NRS time spectra and the corresponding frequency spectra of ^{57}Fe film (20 nm) on $^{57}Fe_xSi_{1-x}$/Si(111) with five azimuthal angles [32].

Figure 2.20: The schematic view of the X-ray optics of the KEK PF-AR NE1A beamline.

2.7.2 Experimental Apparatus

X-ray source

The NRS experiments were conducted in the PF-AR NE1A beamline of High Energy Accelerator Research Organization (KEK). The X-ray is generated by introducing 6.5 GeV electron beam to the wiggler which produces linearly-polarized X-ray. Figure 2.20 shows geometry of the monochromator and the focusing lens of the beamline. The X-ray produced by the wiggler is monochromatized by the Si (111) monochromator to several eV and further by the high-resolution monochromator. The energy width of the monochromatized X-ray is $\sim$ 6.5 meV. The monochromatized X-ray is focused by the focusing mirror. The beam widths along the horizontal and the vertical direction are several mm and several 10 μm, respectively.

UHV Systems

The NRS experiments were carried out using home-made sample holders. Three sample holders with different structures were made: the sample holder for the azimuthal-angle-dependent NRS measurement, the low-temperature NRS measurement, and the high-temperature NRS measurement. Figure 2.21 is the picture of the sample holder designed for the room-temperature NRS experiment. The sample is fixed by the jigs made of alumina. The sample can be heated up to a temperature higher than 1000 K by electron bombardment from the filament behind the sample. The sample holder is mounted on the rotary feedthrough. The jigs and screws are designed to be lower than the surface of the sample so that the X-ray can irradiate the surface at grazing incidence geometry with any azimuthal angle.

Figure 2.22 is the picture of the sample holder designed for the high-temperature NRS measurement. The sample is mounted on the Mo plate which is connected to the Cu plate. The Cu plate is thermally connected to the cryostat which can be cooled with liquid nitrogen or helium. The sample can be heated up to 500 K by flowing current to the W filament behind the sample plate. It is possible to heat the sample to a temperature higher than 1000 K by means of electron bombardment by applying negative bias to the filament. This sample holder is mounted on a rotary feedthrough so that we can rotate the sample to select the incident azimuthal angle. The sample holder used for the low temperature NRS measurement was similar to this, but was slightly different in that the thermal contact with the cryostat was better.

Figure 2.23 shows the experimental apparatus of the NRS experiment. The sample

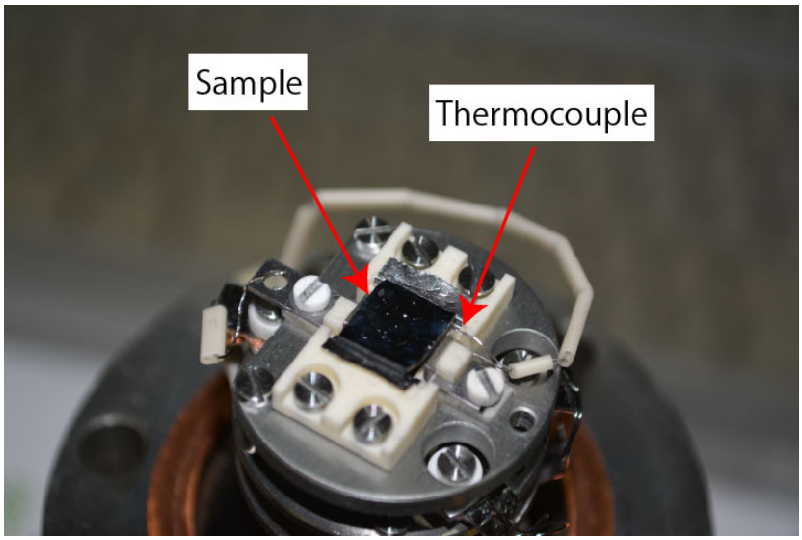

Figure 2.21: The sample holder designed for the room-temperature NRS experiment.

holder is mounted on a cubic chamber which is equipped with two beryllium windows and a sputter ion gun. The cubic chamber is evacuated by a turbo molecular pump and a titanium sublimation pump through a twisting bellows [43]. The twisting bellows is necessary because we cannot measure the glancing-angle-dependence of reflectivity if the sample holder is connected to the pump with normal bellows since normal bellows cannot be twisted. The twisting bellows makes it possible to scan the glancing angle. The base pressure of the whole UHV system was less than 1×10^{-9} mbar which is below the lower measurement limit of the cold-cathode ionization gauge used in the experiment.

X-ray detection and Signal Processing

The scattered X-ray is detected by four avalanche photo diodes (APD). The size of the APD is 5×5 mm and the four APDs are piled up along the direction of the reflected beam. Figure 2.24 is the picture of the signal processing system used in the NRS experiments. Figure 2.25 shows the block diagram of the signal processing system of NRS.The signals from APDs are converted to TTL signals by a discriminator. The output from the discriminator is divided into two lines. One of the two lines is combined by an OR gate and counted by a scaler. The output of this scaler, which is called the prompt intensity, corresponds to the intensity of the beam reflected at the surface without delay. The other line from the discriminator is input to a coincidence unit which extracts the “delay” signal using the VETO signal. The VETO signal is a rectangular pulse which is in the “on”-state only when the prompt signal is observed. The VETO signal is generated from the revolution of electrons in the accumulation ring. The delay signal is input to the “start” terminal of the time-to-amplitude converter (TAC), which measures the time between the “start” and “stop” signals and converts it to the voltage. The stop signal is also generated from the revolution of the accumulation ring. The output from the TAC is summed up by a multi-channel analyzer (MCA) and recorded as a time spectrum.

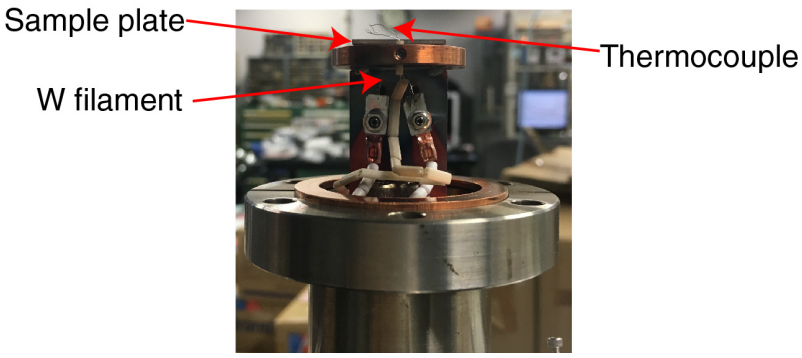

Figure 2.22: The sample holder for the high-temperature NRS experiment.

Time Resolution

The time resolution of the detector used in NRS experiments was checked by observing the pulse shape of the intensity of the prompt light. The original time width of the prompt light is 100 ps which is determined by the width of the bunches in the accumulation ring. Figure 2.26 shows the shape of the prompt signal intensity. The left axis is the intensity and the bottom axis is the time. The full width at half maximum (FWHM) of the prompt signal estimated by Gaussian fitting was 0.57 ns.

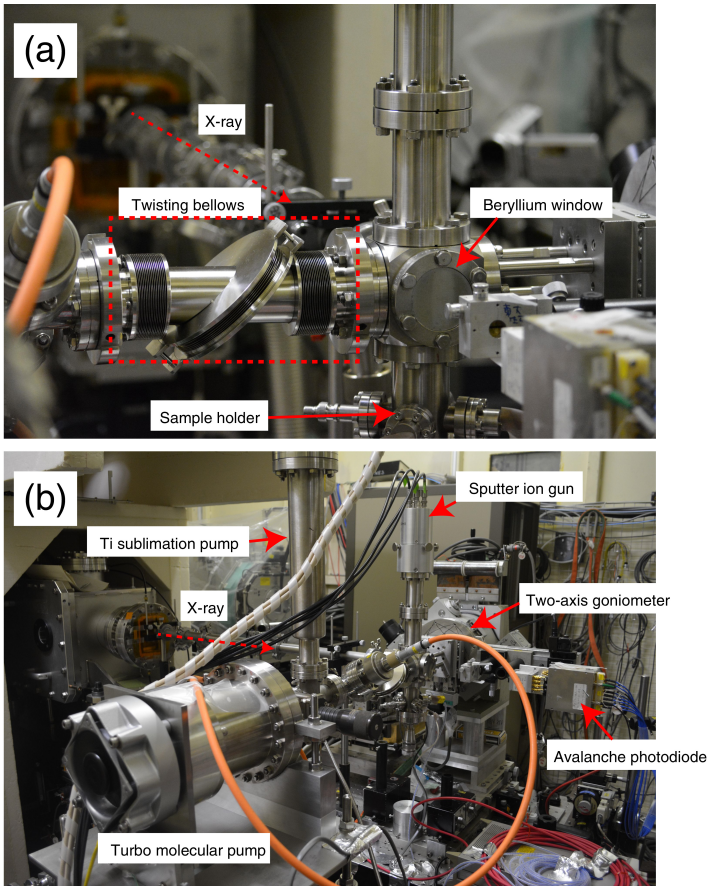

Figure 2.23: A picture of the experimental apparatus of the NRS experiment. (a) is the view from the direction parallel to the X-ray direction

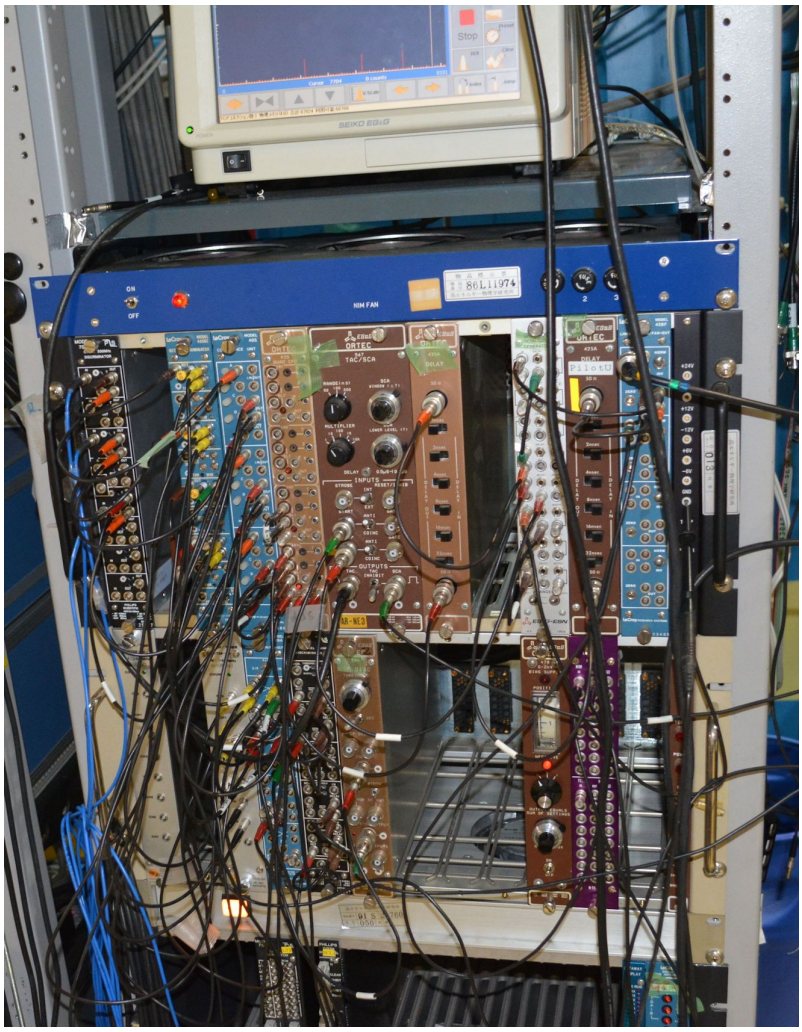

Figure 2.24: The signal processing system used in the NRS experiments.

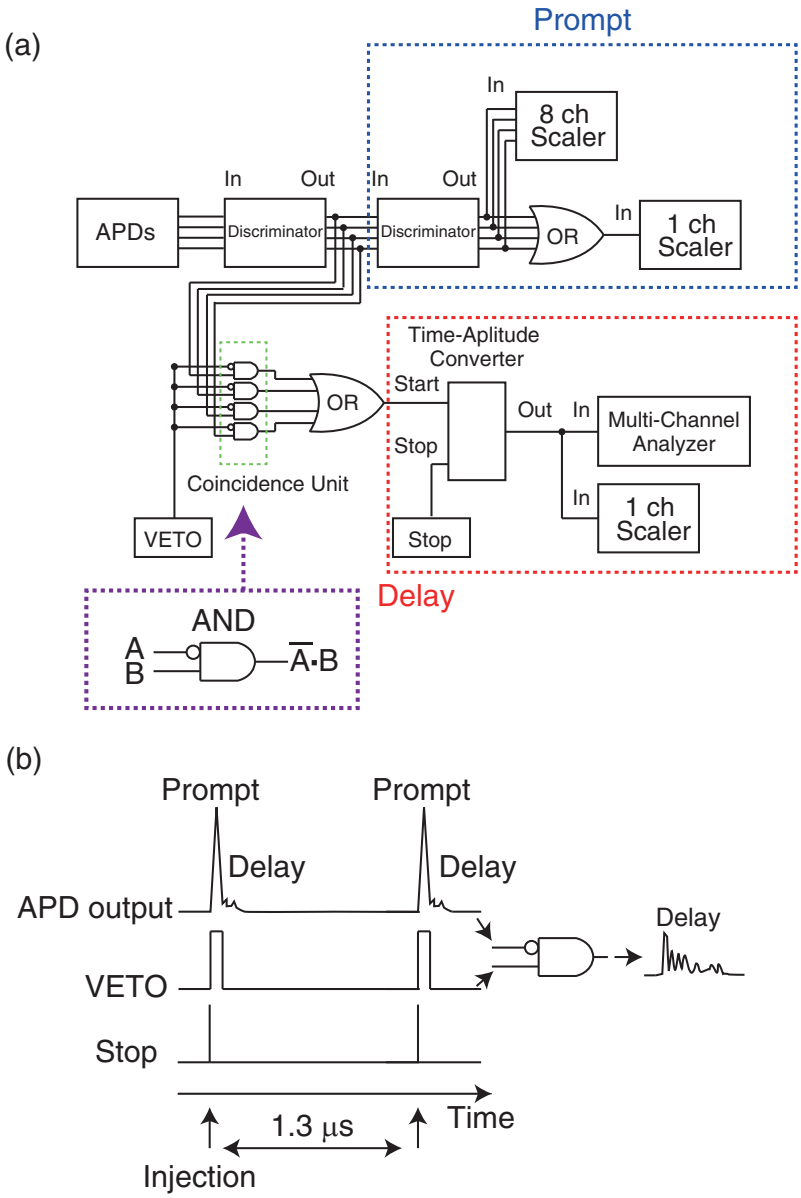

Figure 2.25: (a) The block diagram the signal processing system and (b) the schematic illustration of the APD output, VETO signal, and stop signal.

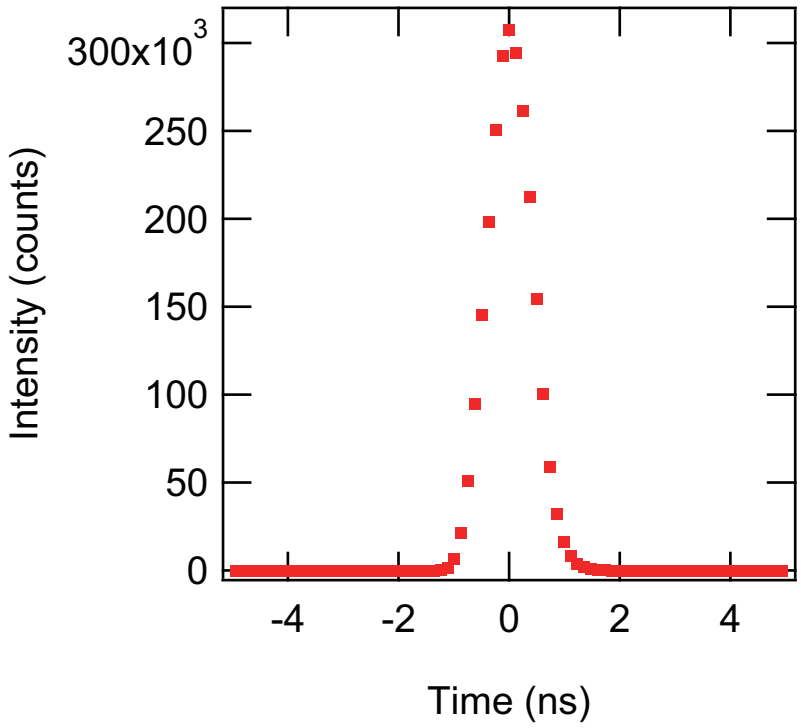

Figure 2.26: The time dependence of the prompt signal intensity.

Chapter 3

Results and Discussions

3.1 Electronic Structure of the Fe_3O_4 (111) Surface

3.1.1 Termination of the Fe_3O_4 (111) Surface

Figure 3.1 (a) shows the stacking sequence of Fe_3O_4 along the [111] direction. There are six possible bulk terminations along the [111] direction. Each layer is labeled as Fe(A)1, O1, Fe(B)1, O2, Fe(A)2 and Fe(B)2. All the bulk terminations are polar. The density of atoms in each layer written in figure 3.1 is calculated by defining that the density of O atoms as 1 ML.

Figure 3.2 shows the dependence of the surface free energy on the oxygen chemical potential with various terminations reported by L. Zhu *et al.* [44]. Fe_{tet1}-O1, Fe_{oct2}-Fe_{tet1}-O1, and O1-Fe_{oct1} termination correspond to Fe(A)1, Fe(B)2, and O1 termination in figure 3.1, respectively. This result shows that the Fe(A)1, Fe(B)2 and O1 layer may be the most stable termination.

It has been reported by STM studies that the Fe_3O_4 (111) surface annealed at 1050 K in UHV is oxygen poor due to the desorption of oxygen. Figure 3.3 shows STM images of the UHV-annealed surface observed by Paul *et. al* [45]. The UHV-annealed Fe_3O_4 (111) surface consists of two structures. One is the region represented by r in figure 3.3. In this region, the periodicity of the corrugation is 6.2 ± 1.1 Åwhich is in good agreement with the bulk Fe(A)1 layer within the experimental error. This structure can be assigned to the Fe(A)1 termination shown in figure 3.1 (a), and we call this region the Fe(A)1-terminated region. The atomic arrangement of the Fe(A)1 termination is shown in figure 3.1(b). The other is the region with superstructures represented by s1 and s2 with a periodicity of 52 ± 6 Å. This region is considered to be the oxygen-poor region since it appears after annealing in UHV and disappears by annealing in O_2. Figure 3.4 shows the detail structure of superstructure s2, which is explained by the combination of Fe(A)1-termination, Fe(B)1-termination, and $Fe_{1-x}O$ islands which are represented by the black dots, small gray points, and the framed region, respectively in figure 3.4 (b). The structure s1 and s2 are considered to be the positive and negative replicas of each other, and the only difference between them is that the Fe(A)1-terminated domain is deepened in superstructure s1 while it is elevated in superstructure s2. The superstructures s1 and s2 are oxygen-poor due to the oxygen desorption during the UHV-annealing, while the Fe(A)1-terminated region is stoichiometric due to the diffusion of oxygen from the bulk. Paul *et al.* showed that the Fe(A)1-terminated region occupies 90% of the UHV-annealed surface and the other 10 % is occupied by superstructures s1 and s2 [45]. The reason why the structures s1 and s2 are stable in oxygen-poor conditions is not clarified.

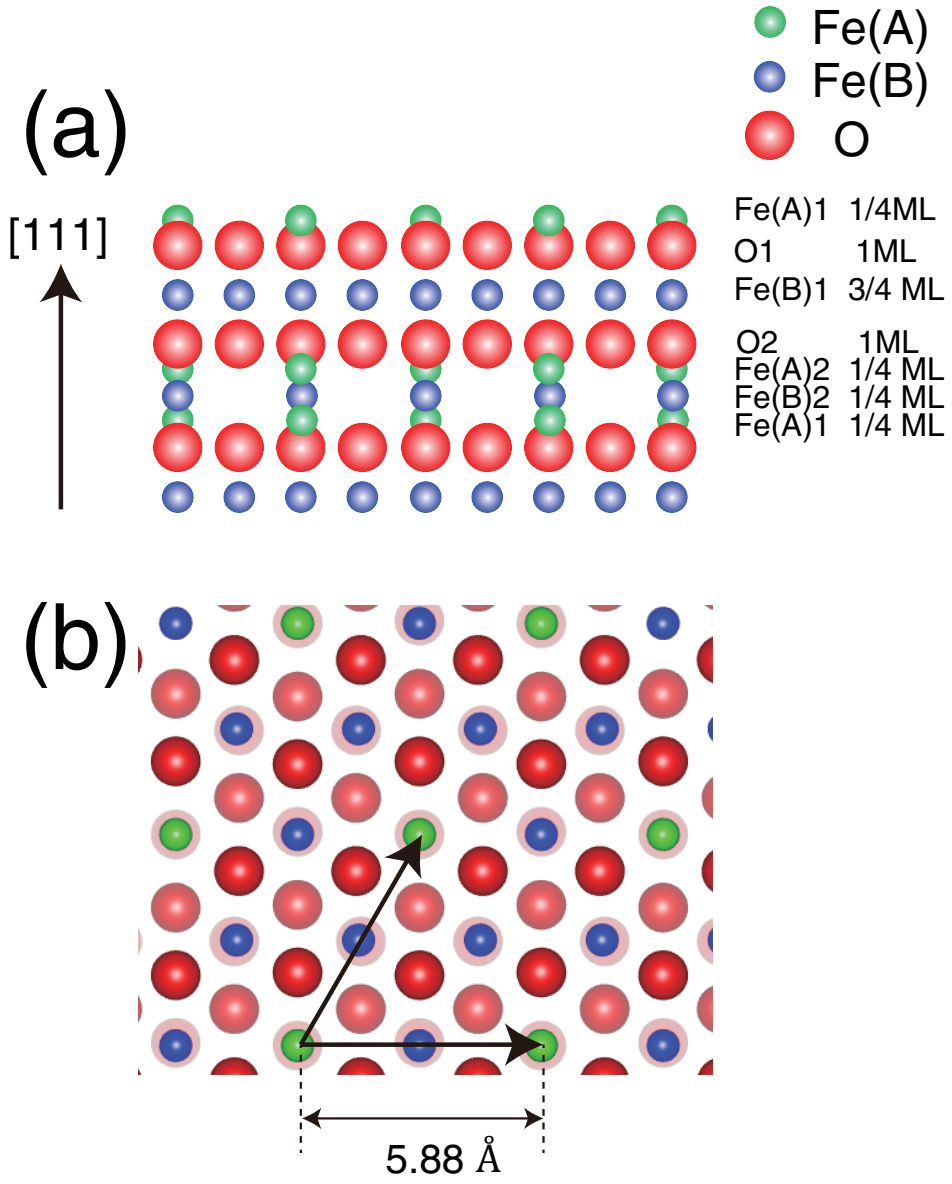

Figure 3.1: (a) Stacking sequence of Fe_3O_4 along the [111] direction. The viewing direction is along the $[1\bar{2}1]$ direction. The blue, green, and red balls represent the Fe(B), Fe(A), and oxygen atoms. The six possible bulk terminations are shown. Here, the atom density of the closed-packed oxygen layer is defined as 1 ML.(b) Top view of the Fe(A)1 termination. The upward direction corresponds to the $[1\bar{2}1]$ direction. The topmost Fe(A) atoms are arranged in a hexagonal structure with a lattice constant of 5.88 Å.

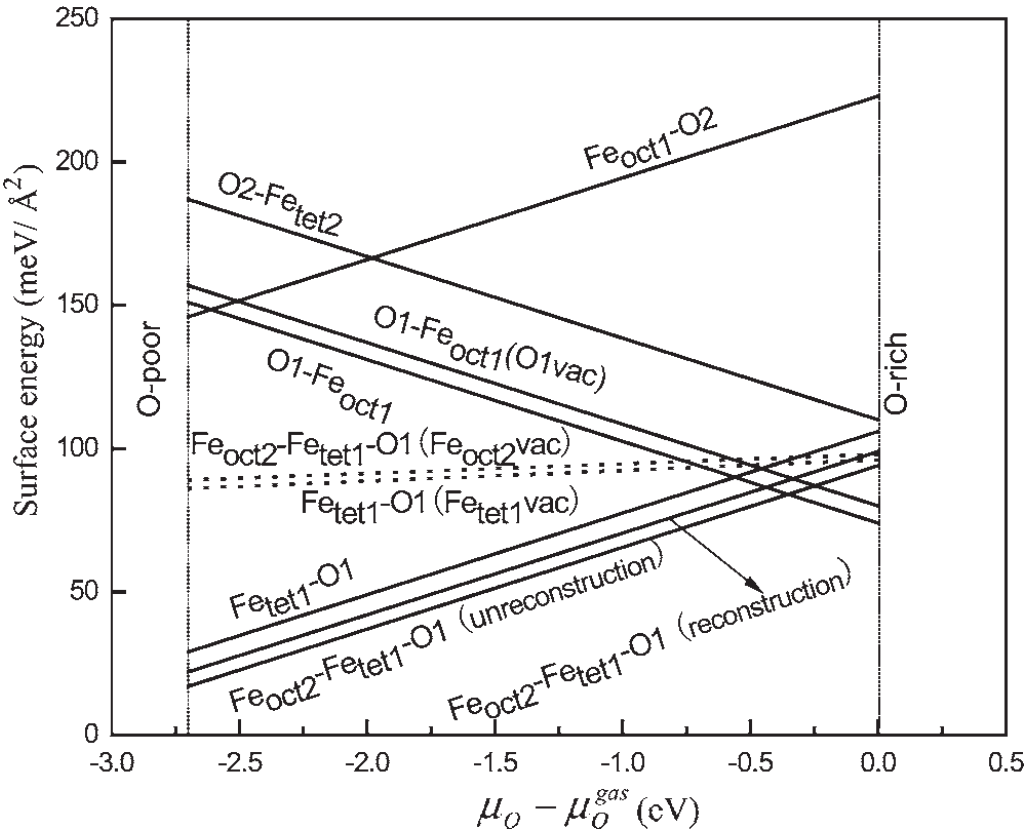

Figure 3.2: The surface free energy as a function of the chemical potential $\mu_0 - \mu_0^{gas}$ of oxygen for various terminations. The dotted vertical lines indicate the allowed range of the oxygen chemical potential [44].UHV conditions (10^{-10} mbar) corresponds to ~ -2 eV.

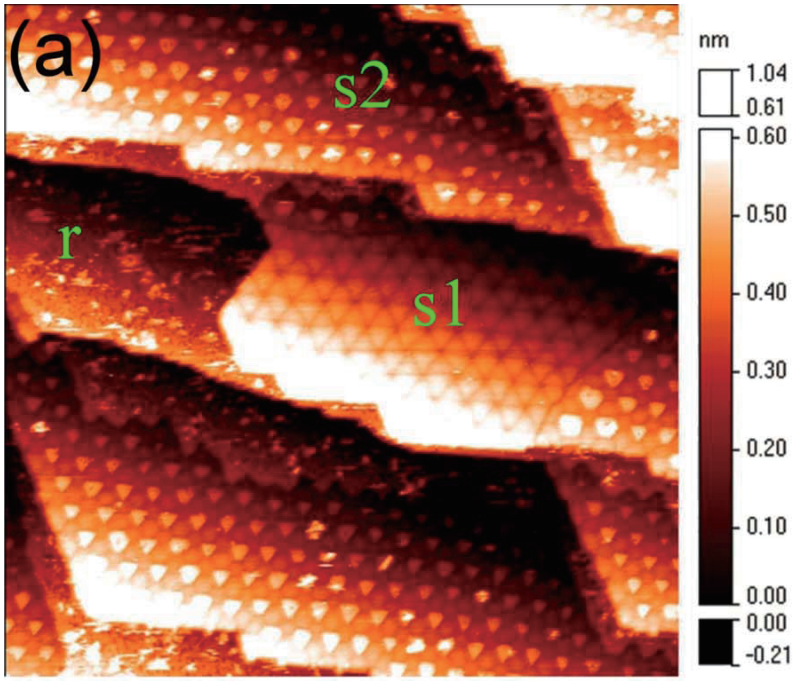

Figure 3.3: 134×134 nm^2 STM image of a UHV-annealed surface with superstructures (s1, s2) and Fe(A)1-terminated region (r) observed by Paul *et. al* [45]. The tunneling current was fixed at 0.2 μA and the gap voltage was set to -2 V [45].

The superstructures s1 and s2 can be removed by annealing at 1000 K in an oxygen partial pressure of 5×10^{-6} mbar. Figure 3.5 shows the STM image of the Fe_3O_4 (111) surface after UHV annealing and O_2 annealing observed by Paul *et. al* [45]. The termination of this surface is assigned to the Fe(A) layer by studies using STM and LEED [46, 47].

3.1.2 Sample Preparation

In this study, the (111) surface cut and polished from a natural Fe_3O_4 single crystal was used. The crystal orientation of the surface was checked by the Laue method. The cleanliness of the surface was checked by X-ray photoemission spectroscopy (XPS) with Al-K_α X-ray ($h\nu$ = 1486.6 eV) before mounting the sample to the UPS chamber. The XPS spectrum of the air-exposed sample, shown in figure 3.6, showed peaks derived from impurities such as carbon (285 eV) and argon (242 eV, 244 eV and 320 eV). The existence of argon is because of the Ar sputtering conducted before the XPS measurement in order to roughly clean the surface. The carbon is considered to be derived from air.

After the XPS measurement, the sample was mounted on the sample holder, and . Firstly, the impurity on the surface was removed by Ar^+ ion sputtering. The Ar^+ ions are accelerated to 1 keV towards the sample by a sputter ion gun. After sputtering, the sample was annealed in UHV at 1000 K for 10 min order to recover the atomic flatness. Here, we call this surface the UHV-annealed surface. The cleanliness of the UHV-annealed surface was again checked in-situ by XPS with Al-K_α X-ray ($h\nu$ = 1486.6 eV). The result, shown in figure 3.7, shows that the carbon impurities were removed by the preparation. The

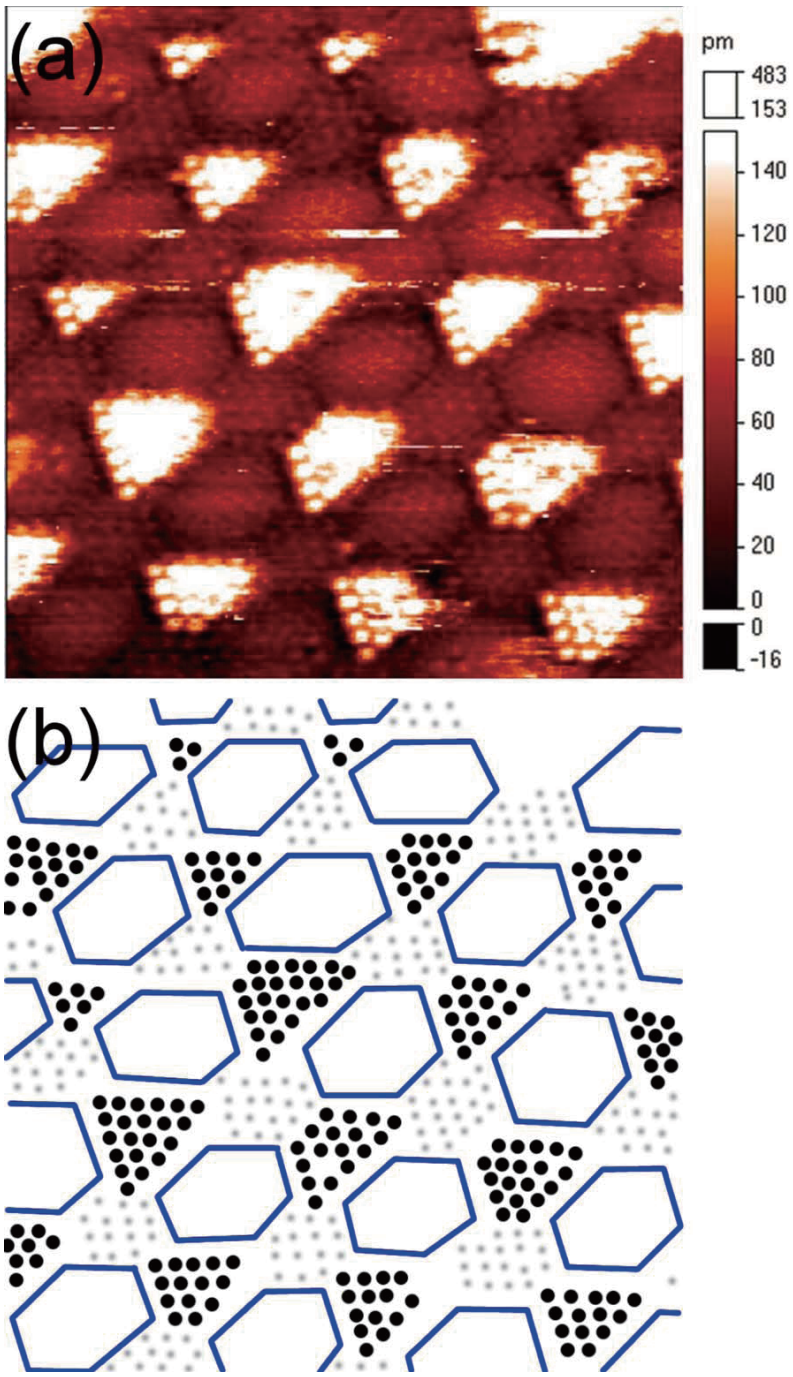

Figure 3.4: (a)21 × 21 nm^2 STM image of the superstructure s2. (b) Schematic for the atomic arrangement of STM image shown in (a): the black dots, the small Grey points, and the framed region are assigned to the Fe(A)1 layer, Fe(B)1 layer, and the islands with $Fe_{1-x}O$-like configuration, respectively [45].

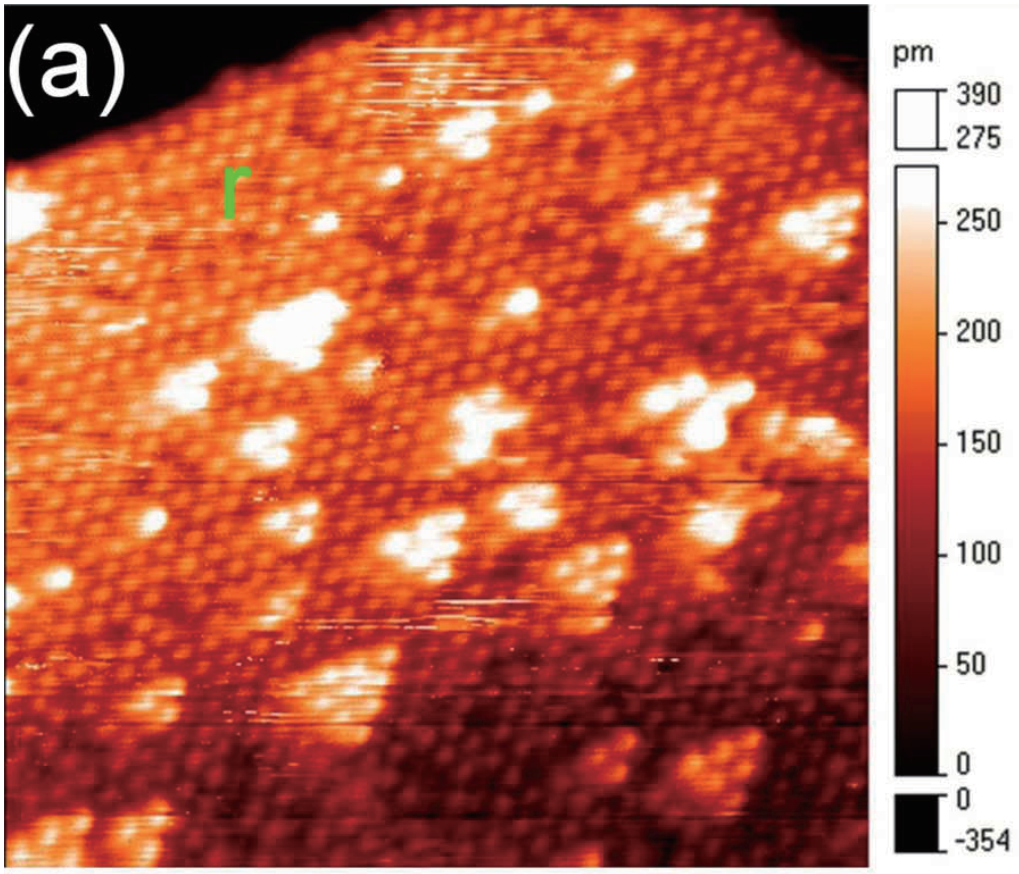

Figure 3.5: 20×20 nm^2 STM image of a surface with Fe(A)1-terminated region (r) observed by Paul *et. al* [45]. The tunneling current and the gap voltage were 0.1 nA and 1 V, respectively. The bright triangular features can be assigned to adsorbates.

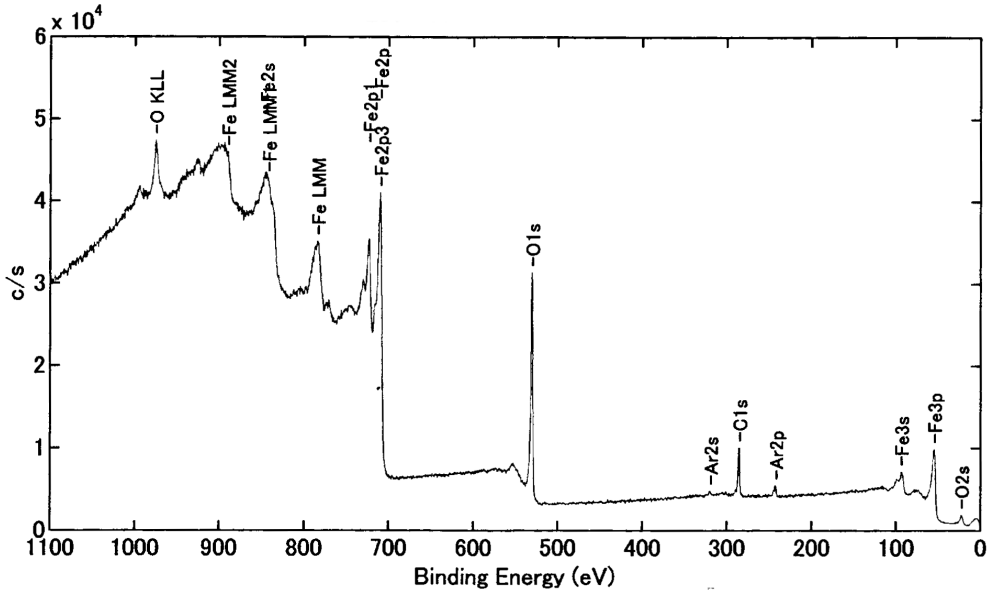

Figure 3.6: The XPS spectrum of the air-exposed Fe_3O_4 (111) surfaces.

other component such as Mo, Ta, and Cr in figure 3.7 are derived from the jigs, screws and the sample plate. In this measurement, the energy resolution was not good enough to identify the valency number of Fe ions by the chemical shift.

The previous study [45] showed that, after UHV-annealing, the surface consists of 90% Fe(A)1-terminated region and 10% superstructure region. They also showed that the superstructure region can be removed by annealing in O_2. Based on their considerations, the sample was annealed in an oxygen partial pressure of 5×10^{-6} mbar for 10 minutes after UHV-annealing. During cooling down, the oxygen supply was stopped when the sample temperature reached 700 K in order to avoid the desorption of oxygen. Here, we call this surface the "regular" surface. The regular surface is expected to be terminated by the Fe(A)1 layer.

Figure 3.8 (a) shows the LEED pattern of the UHV-annealed Fe_3O_4 (111) surface taken in another UHV chamber. Satellites are observed around each spot, indicating the presence of superstructure with a lattice constant 6 - 8 times as large as the unit cell of the unreconstructed Fe_3O_4 (111) surface. This is considered to be derived from the superstructures shown in figures 3.3 and 3.4. The LEED pattern of the regular surface, shown in figure 3.8(b), showed 1×1 pattern. The periodicity estimated from the distance between the spots corresponds to a lattice constant of 5.8 ± 0.3 Å, which is in good agreement with the periodicity of the Fe(A)1 layer (5.88 Å) calculated from the bulk lattice constant. The red arrows represent the primitive translation vector of the LEED pattern. Figure 3.8 (c) shows the schematic view of the Fe(A)1 termination and the reciprocal vector that corresponds to the vectors shown in figure 3.8 (b).

Figure 3.9 (a) shows the UPS spectra of the Fe_3O_4 (111) surfaces before the O_2 annealing (labeled as UHV-annealed) and after O_2 annealing (labeled as O_2-annealed). The measurement was conducted at room temperature, and the helium I line (21.22 eV) was used as the incident light. For all UPS results, the intensity was normalized by measuring

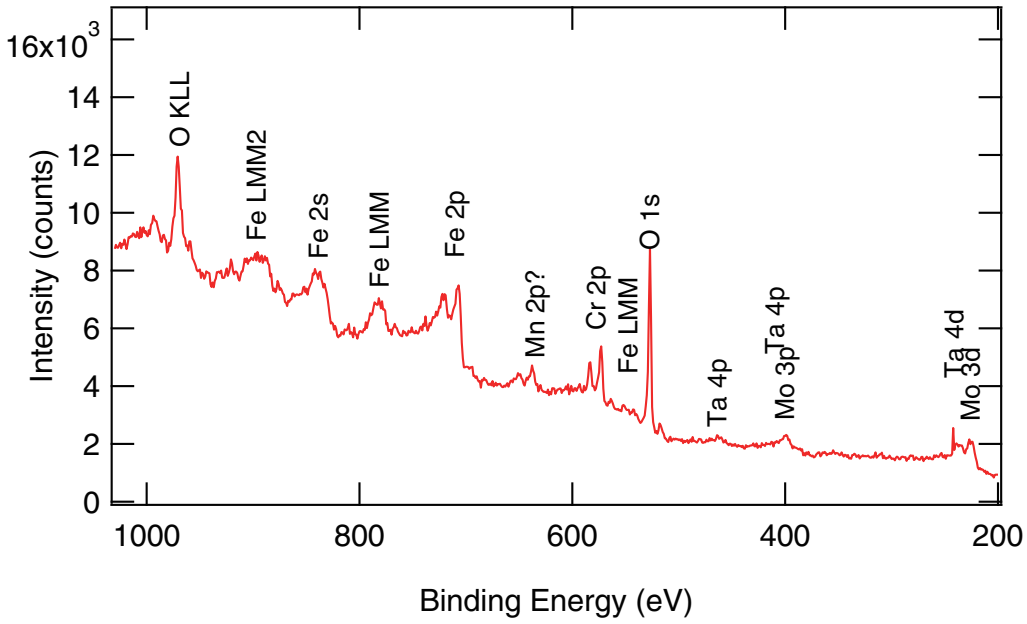

Figure 3.7: The XPS spectrum of the Fe_3O_4 (111) surface after Ar^+ sputtering and annealing.

the Au spectra right after measuring Fe_3O_4. The UPS spectra of Fe_3O_4 (111) surfaces have peaks at −0.6 eV, −2.8 eV, −4.3 eV and −5.8 eV, which are in good agreement with the previous studies [48, 49]. Figure 3.10 shows the spin-projected electron density of states of Fe_3O_4 obtained by the calculation within the framework of local-spin-density approximation to the density-functional theory [50]. The upper and the lower graph show the density-of-states of the up-spin and the down-spin electrons, respectively. The Fermi surface is formed by the down-spin Fe(B) t_{2g} state. The density-of-states at 1–4 eV below the Fermi level is attributed to the down-spin Fe(A) 3d state and up-spin Fe(B) 3d state. The density-of-state at 4–8 eV below the Fermi level is derived from the O 2p state.

Figure 3.9 (b) shows the cutoff of the low-energy electrons. The cutoff of the UHV-annealed surface has two steps which indicates the existence of two domains with different work function, which are labeled cutoff 1 and 2 in figure 3.9(b). The position of the cutoff is determined by the inflection point of the spectrum. The calculated work functions for cutoff 1 and 2 are 4.95 eV and 4.22 eV, respectively. On the other hand, the O_2-annealed Fe_3O_4 (111) surface has one cutoff. The work function was 5.03 eV which is close to the work function of cutoff 1 of the UHV-annealed surface. This indicates that the cutoff 2 of the UHV-annealed surface disappeared after the O_2-annealing. Therefore, we assign the cutoff 1 of the UHV-annealed surface to the Fe(A)1-terminated region and cutoff 2 to the superstructures (s1 and s2) shown in figure 3.3. The size ratio of the cutoff (cutoff 1:cutoff 2 $\simeq$ 6 : 1) was in good agreement with the previous report that the Fe(A)1-terminated region and the superstructures occupy 90% and 10% of the UHV-annealed surface [45]. Figure 3.9 (c) shows the features near the Fermi level. The peak at 0.6 eV is assigned to the down-spin electron of the Fe(B)-3d t_{2g} orbital [51]. The Fe(B)-3d t_{2g}-derived intensity decreased after the O_2 annealing. This indicates that the surface Fe(B) atoms are oxidized by the O_2 annealing. Figure 3.9 (c) shows the subtraction of

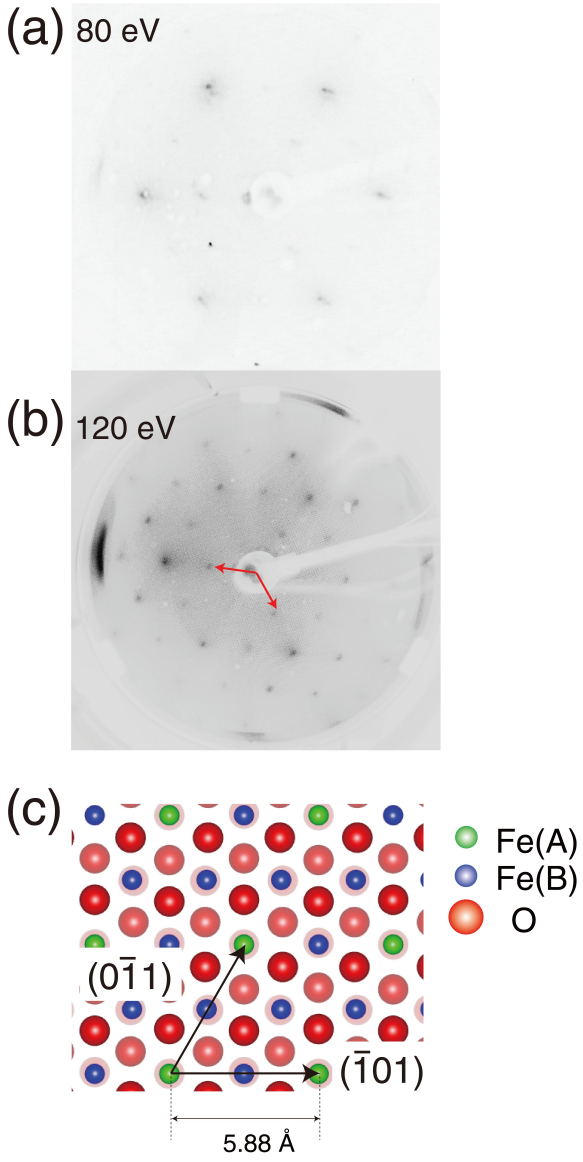

Figure 3.8: The LEED patterns of the regular(a) the UHV-annealed Fe_3O_4 (111) surface with $E = 80$ eV at 412 K and (b) the regular surface with $E = 120$ eV at 410 K. The red arrows in (b) represent the primitive translation vector of the LEED pattern. The corresponding vector is represented by the arrows in (c).

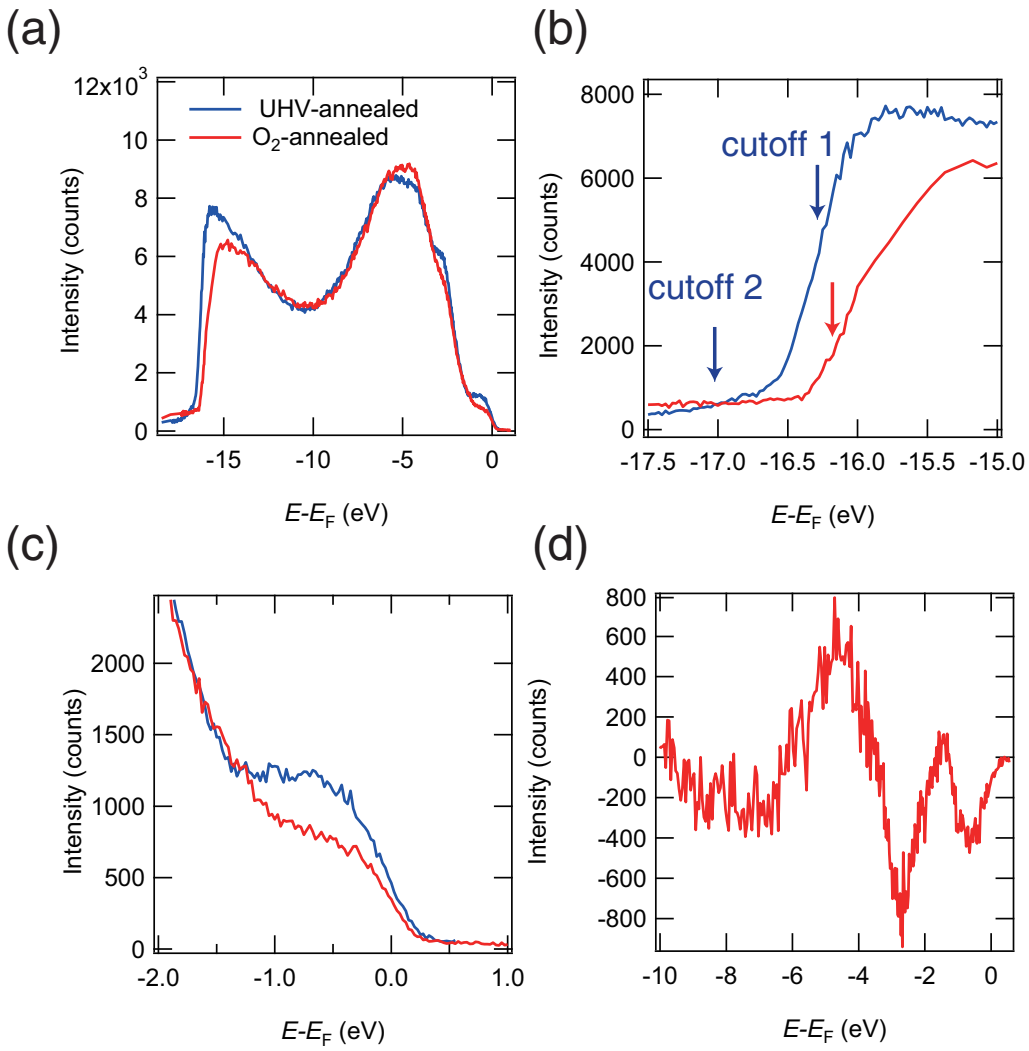

Figure 3.9: The UPS spectra of the Fe_3O_4 (111) surface after Ar^+ sputtering and annealing (blue line) and after Ar^+ sputtering, annealing, and O_2 annealing (red line). (a) shows the whole spectra, (b) shows the cutoff, (c) shows the features near the Fermi level, and (d) shows the subtraction of the spectrum of the regular surface from the UHV-annealed surface. The arrows in (b) shows the position of the cutoff.

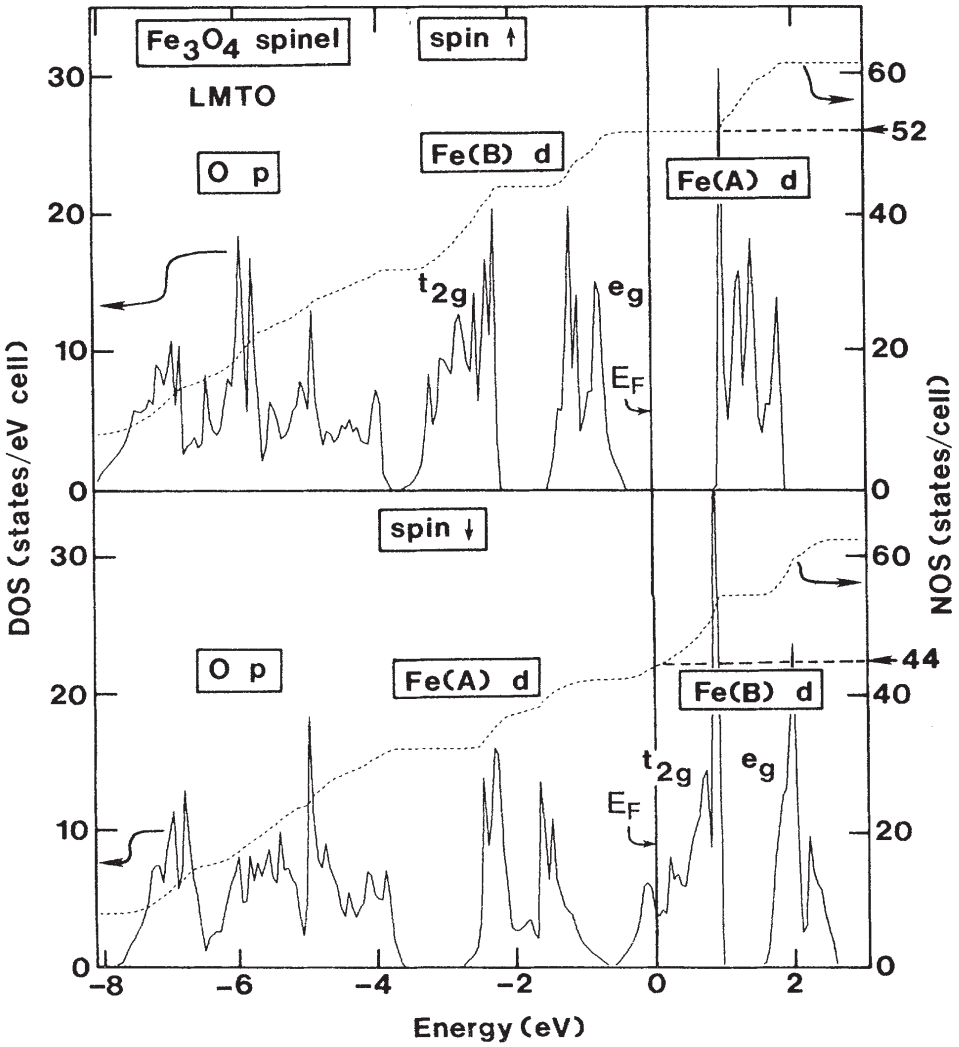

Figure 3.10: Spin-projected one-electron density of states and numbers of states of Fe_3O_4 [50].

the spectrum of the regular surface from the UHV-annealed surface. It can be seen from the figure that the intensity around −0.6 eV and −2.7 eV decreased and the intensity at −6.2 – −3.3 eV increased after O_2 annealing. The decrease of intensity at −0.6 eV is attributed to the decrease of Fe(B)-3d t_{2g} electrons due to the electron transfer from the Fe(B)-t_{2g} orbital to oxygen. Intensity around −2.7 eV is derived from the Fe(A) 3d and Fe(B) 3d orbital and intensity at −6.2 – −3.3 eV is derived from the O 2p orbital. This means that the composition ratio Fe/O decreased after O_2-annealing. This is consistent with the previous report [45] which claimed that that the UHV-annealed surface includes a superstructure region which is oxygen-poor due to the desorption of oxygen while the regular (O_2-annealed) surface is terminated by the stoichiometric Fe(A)1 layer.

3.1.3 Modification of the Electronic States of the Regular Surface

After annealing in O_2, we investigated the change of the UPS spectrum by atomic hydrogen and oxygen exposure at room temperature. Firstly, the reaction between the O_2 annealed (regular) surface and atomic hydrogen was investigated. Secondly, the changes by oxygen exposure were investigated. Finally, the effect of atomic hydrogen exposure to the O_2-exposed regular surface was investigated.

H+H_2 exposure

Figure 3.11 (a) shows the UPS spectra of the the regular Fe_3O_4 (111) surface with various amount of H+H_2 exposure. The atomic hydrogen is generated by heating a tungsten filament to 1700°C in a hydrogen atmosphere of 1.3×10^{-7} mbar. Figure 3.11 (b) shows the features near the cutoff of the UPS spectra. The cutoff shifts to the low-energy side with increasing hydrogen exposure. This indicates that the work function decreased from 5.03 eV to 4.50 eV by H+H_2 exposure, as shown in figure 3.11(c). Figure 3.11 (d) shows the Fe(B) t_{2g}-derived peak. The intensity at -0.6 eV did not change within the experimental error, which means that the ratio Fe^{2+}/Fe^{3+} of the Fe(B) site did not change. The intensity at E=-10 – -3 eV decreased uniformly after H+H_2 exposure.

O_2 exposure

Figure 3.12 shows the change of the UPS spectra of the regular Fe_3O_4 (111) surface by 100 L O_2 exposure at room temperature. Here, we call this surface the regular+O_2 (100 L) surface. The position of the cutoff did not change after the O_2 exposure which indicates that the work function did not change significantly. The intensity of the Fe(B) t_{2g}-derived peak, shown in figure 3.12 (c), decreased and the intensity around 2.8 eV increased after the oxygen exposure . The decrease of the Fe(B) t_{2g}-derived peak indicates the adsorbed oxygen took the electron from the Fe(B) t_{2g} orbital.

H+H_2 exposure after O_2 exposure

Figure 3.13 shows the change of the UPS spectra of the regular+O_2 (100 L) surface by atomic hydrogen exposure. The cutoff energy shifted to the lower energy by atomic hydrogen exposure as shown in figure 3.13(b). The work function, shown in figure 3.13 (c), decreased from 5.22 eV to 4.65 eV. The intensity of the Fe(B) t_{2g}-derived peak in figure 3.13 (d) increased by H exposure. The intensity at -0.6 eV increased by 53 % after exposing to 100 L of H+H_2. This means that electrons were doped to the Fe(B) t_{2g} orbital. The intensity at E=-10 – -3 eV decreased uniformly after H+H_2 exposure.

3.1.4 Comparison with the UHV-annealed Surface

The final step of the preparation procedure of the regular surface is O_2 annealing. After O_2 annealing, we kept supplying O_2 until the sample was cooled down to 700 K in order to avoid the creation of oxygen vacancies. However, there is a concern that the exposure to oxygen during cooling down may generate oxygen-terminated regions [52] which is terminated by the closed-packed oxygen layer. Therefore, in order to confirm that the

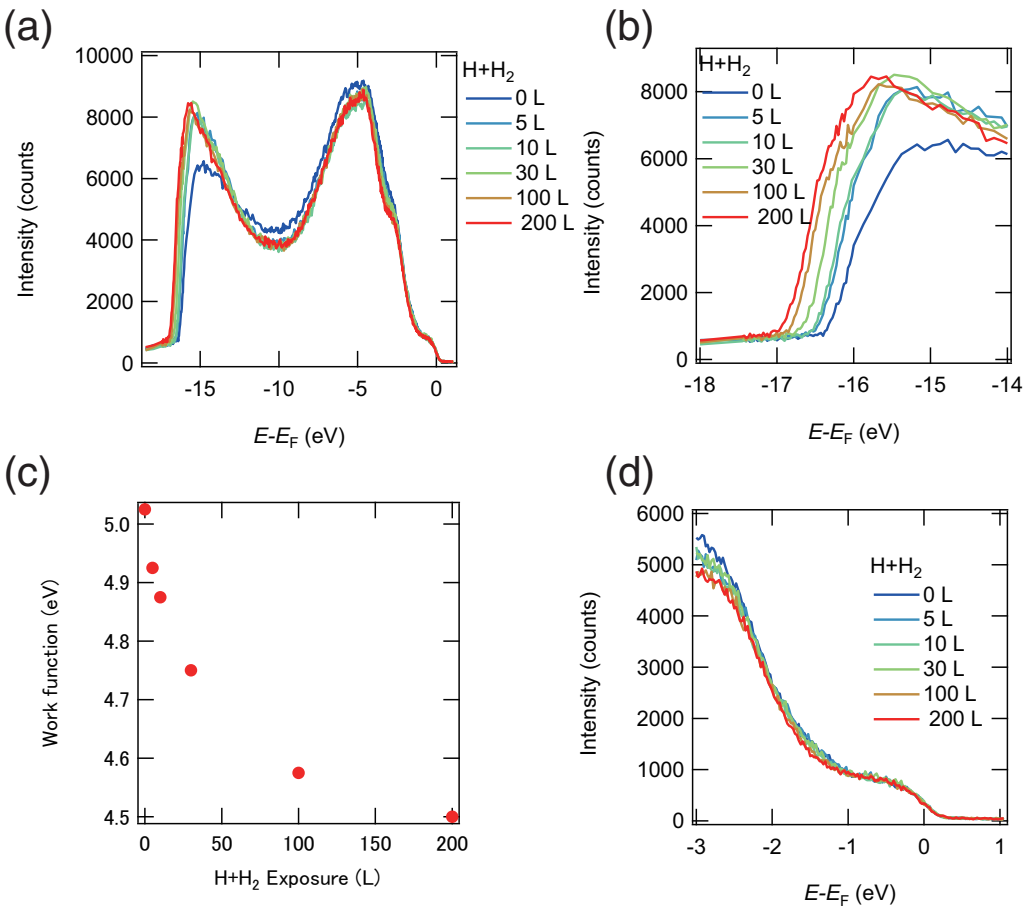

Figure 3.11: The change of the UPS spectra of the regular Fe_3O_4 (111) surface by $H+H_2$ exposure. (a) the whole spectra, (b) the cutoff (c) the dependence of the work function on $H+H_2$ exposure, and (d) the evolution of the Fe(B) t_{2g}-derived peak by $H+H_2$ exposure.

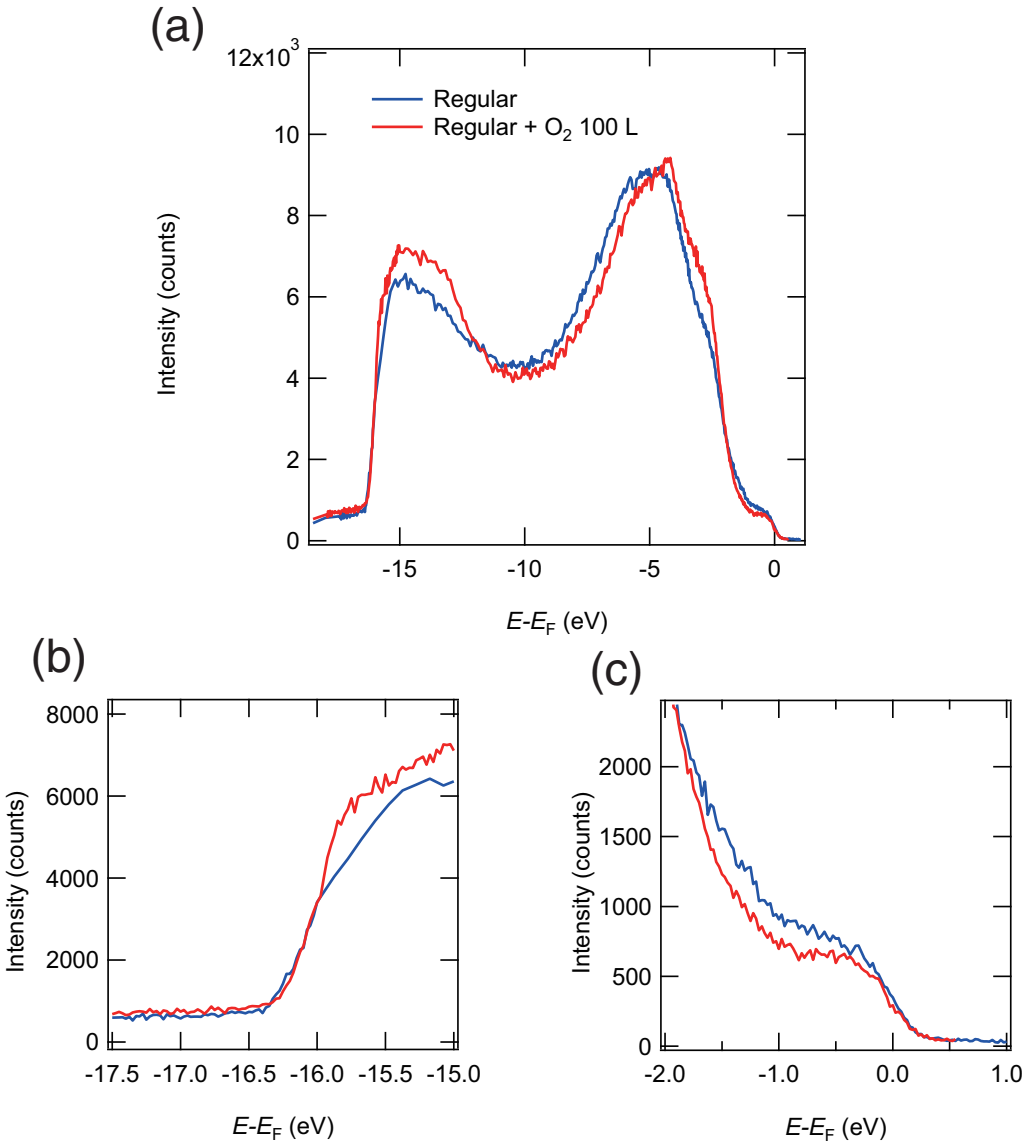

Figure 3.12: The UPS spectra of the regular Fe_3O_4 (111) surface (blue line) and the regular surface after exposing to 100 L O_2 (red line). (a) shows the whole spectra, (b) shows the cutoff, and (c) shows the features near the Fermi level.

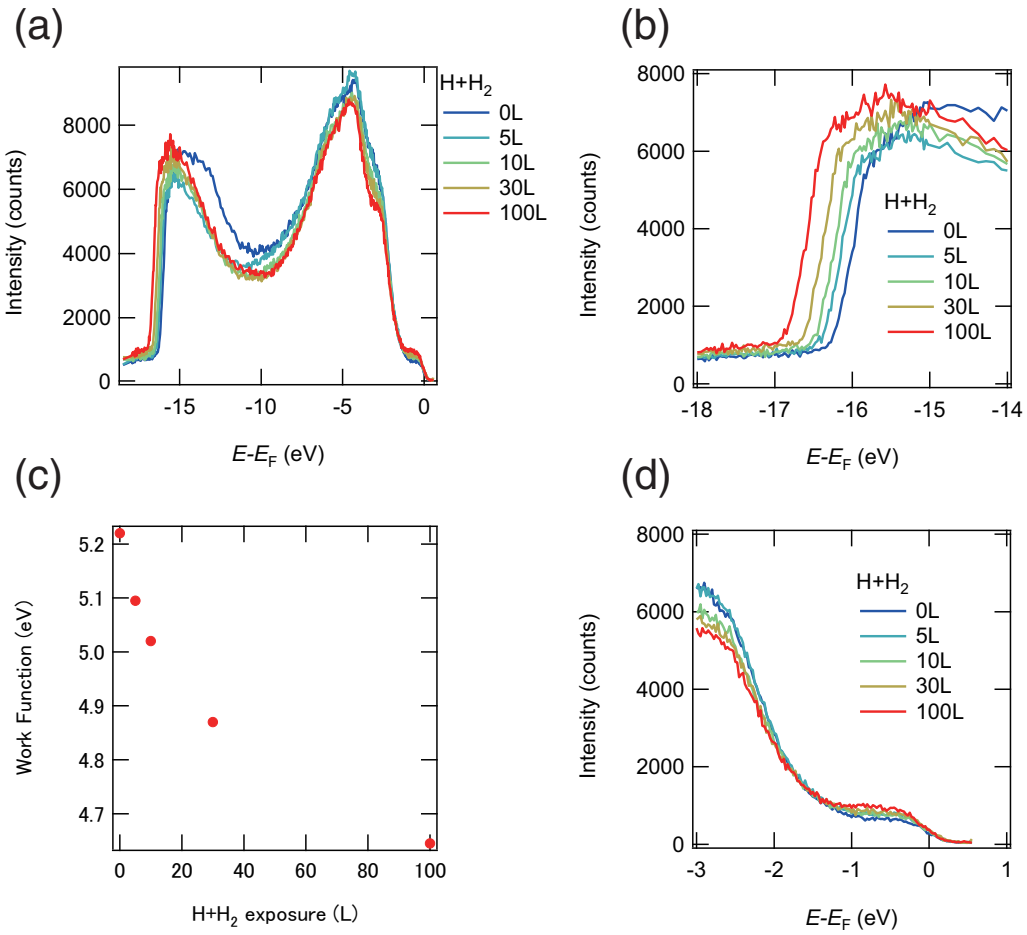

Figure 3.13: The change of the UPS spectra of the 100L O_2-deposited regular Fe_3O_4 (111) surface by atomic hydrogen exposure.

regular surface is terminated by Fe(A), we repeated the same procedures, $H+H_2$ exposure, O_2 exposure, and $(O_2)+(H+H_2)$ exposure, on the UHV-annealed surface, because it is experimentally confirmed that about 90% of the UHV-annealed surface is covered with Fe(A)1 termination and it is less likely to have oxygen-terminated region than the regular surface.

$H+H_2$ exposure

Figure 3.14 shows the change of the UPS spectra of the UHV-annealed Fe_3O_4 (111) surface by atomic hydrogen exposure. The cutoff of the low-energy electrons consists of two edges, as shown in 3.14(b). The position of the cutoff 1, which is considered to be derived from Fe(A)1-terminated region, shifts to lower energy by $H+H_2$ exposure. The work function estimated from the inflection point of the cutoff is shown in figure 3.14 (c), which shows monotonic decrease from 4.95 eV to 4.55 eV. Figure 3.14 (d) shows the Fe(B) t_{2g}-derived peak. The intensity at -0.6 eV did not change within the experimental error. The intensity at E=-10 – -3 eV decreased uniformly after $H+H_2$ exposure. These results are similar to the results of $H+H_2$ exposure on the regular surface.

O_2 exposure

We prepared an UHV-annealed surface again to observe the change of the UPS spectrum by oxygen exposure. Figure 3.15 shows the UPS spectra of the UHV-annealed surface before and after 100 L O_2 exposure. The peak at -5.8 eV decreased after O_2 exposure while the peak at -4.3 eV did not change significantly. As shown in figure 3.15 (b), cutoff 2 seems to disappear after the O_2 exposure, which indicates that the work functions of the superstructure region became indistinguishable from the Fe(A)1-terminated region. The Fe(B) t_{2g}-derived peak, shown in figure 3.15 (c) decreased after the O_2 exposure, which indicates that the surface Fe(B) atoms are oxidized by the oxygen adsorption. These changes induced by the O_2 exposure are in common with the regular surface.

$H+H_2$ exposure after O_2 exposure

After exposing the UHV-annealed surface to 100 L O_2, we exposed $H+H_2$. The cutoff of the low-energy electrons shifts to the lower energy, as shown in figure 3.16 (b). The work function estimated from the cutoff, shown in figure 3.16 (c), decreases from 5.10 eV to 4.52 eV. This is similar to the result of $H+H_2$ on the O_2-exposed regular surface. The intensity of the Fe(B) t_{2g}-derived peak in figure 3.13 (d) increased by H exposure. The intensity at -0.6 eV increased by about 20 % after exposing 100L $H+H_2$. The intensity at E=-10 – -3 eV decreased uniformly after $H+H_2$ exposure. This is also in common with the result of the regular surface.

So far, we could find no significant difference between the regular surface and UHV-annealed surface except for the existence of the superstructure region in the UHV-annealed surface which is observed as a shoulder of the low-energy cutoff. Therefore, by comparing the results of the regular and the UHV-annealed surface, we could confirm that the regular Fe_3O_4 (111) surface, prepared by Ar^+ sputtering, UHV-annealing, and O_2 annealing, is identical to the Fe(A)1-terminated region of the UHV-annealed surface.

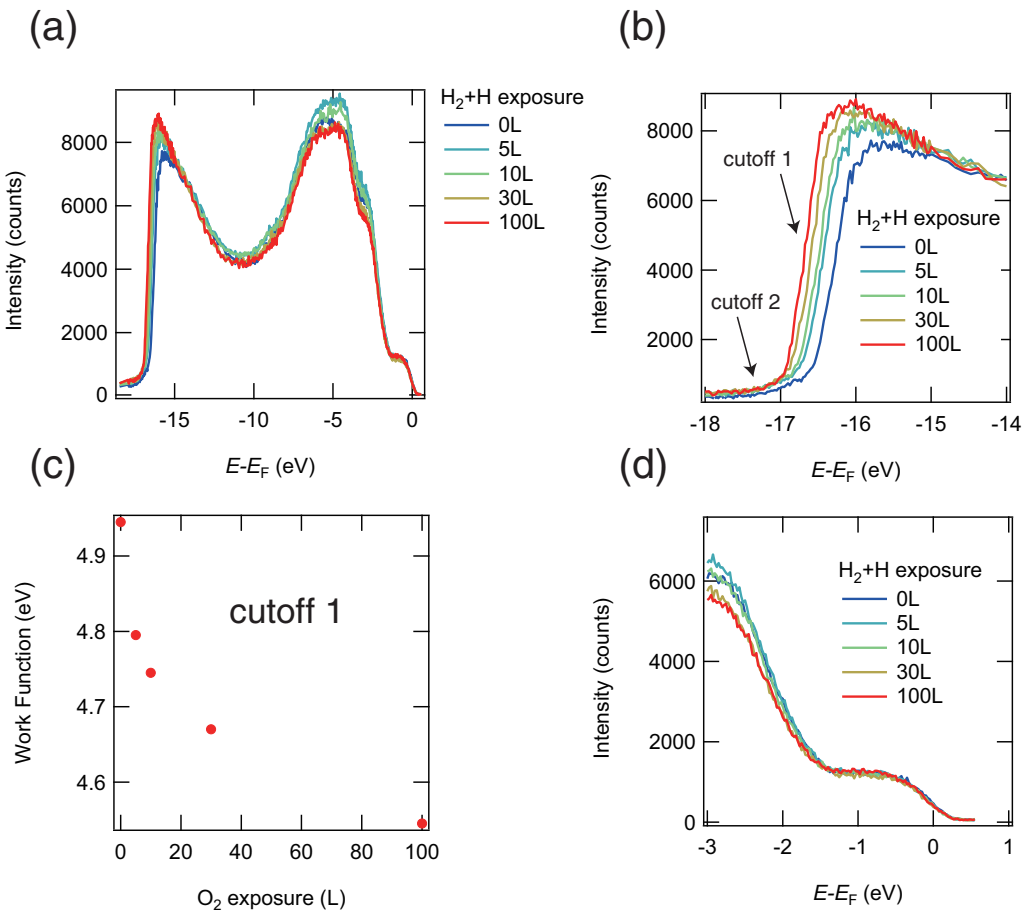

Figure 3.14: The change of the UPS spectra of the UHV-annealed Fe_3O_4 (111) surface by atomic hydrogen exposure. (a) shows the whole spectra, (b) shows the cutoff (c) shows the dependence of the work function estimated from the cutoff 1 on $H+H_2$ exposure, and (d) shows the Fe(B) t_{2g}-derived peak.

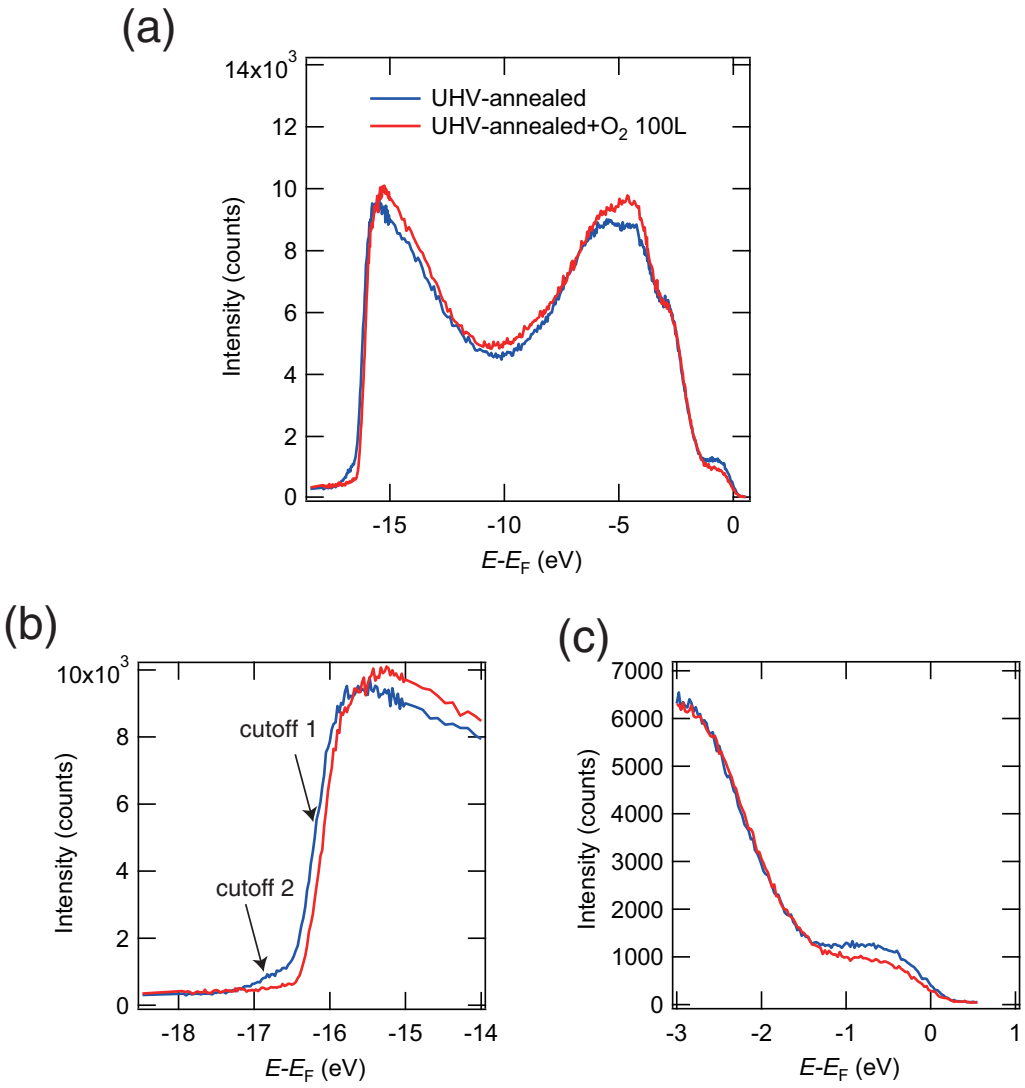

Figure 3.15: The change of the UPS spectra of the UHV-annealed surface by 100 L O_2 exposure. (a) shows the whole spectra, (b) shows the cutoff, and (c) shows the features near the Fermi level.

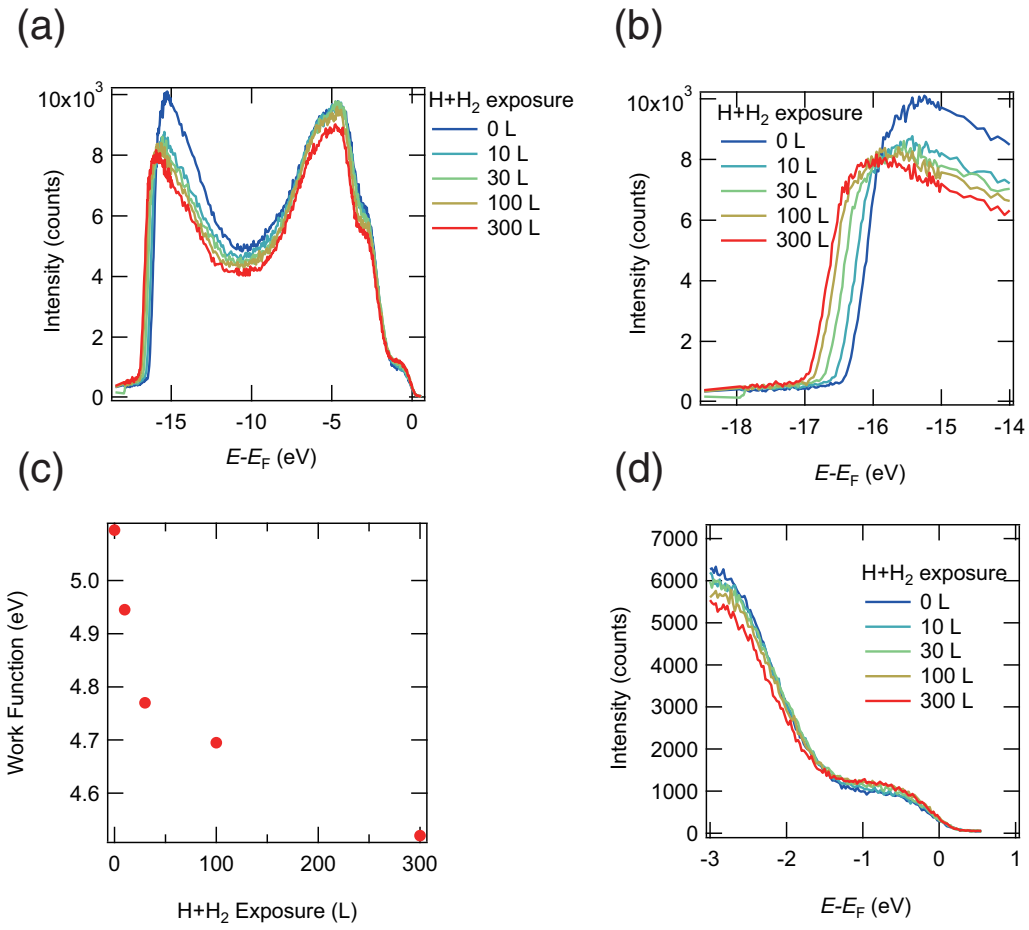

Figure 3.16: The change of the UPS spectra of the 100L O_2-deposited UHV-annealed Fe_3O_4 (111) surface by atomic hydrogen exposure.

3.1.5 Discussion

The change of work function by the $H+H_2$ exposure is the evidence of H adsorption on the surface. One possible mechanism of the change of the work function is the formation of electric dipole by the ionized adsorbates. If the adsorbed H is ionized, it will cause change in the Fe(B) t_{2g}-derived peak in the UPS spectrum. In the case of the reported results on the hydrogen exposure on the Fe_3O_4 (001) surface [17, 19], the hydrogen atom adsorbs on surface O atoms. Parkinson *et al.* [17] reported that the number of electrons in the Fe(B) t_{2g} state increases after H adsorption. Figure 3.17 show the UPS and the XPS spectrum of the Fe_3O_4 (001) surface before and after the atomic H exposure. In the UPS spectra, the Fe(B) t_{2g}-derived peak near the Fermi level increases dramatically by H exposure. In the XPS spectra, the intensities at 709 eV and 711.4 eV are the contribution of Fe^{2+} and Fe^{3+} cations, respectively. The result shows that the intensity at 711.4 eV increases which indicates that the amount of Fe^{2+} increases by H adsorption. This means that, on the (001) surface, the adsorbed H atom reduces the surface Fe(B) atoms which results in the increase of Fe(B) t_{2g}-derived peak in the UPS spectra. In the present results of the Fe(A)-terminated surface, the intensity of the Fe(B) t_{2g}-derived peak did not change. This means that the hydrogen did not release its electron since if the H atom releases its electron, the electron is likely to be doped to Fe(B) t_{2g} orbital. Therefore, the charge transfer model is not the appropriate model to explain the decrease of work function in the present case. Another possibility is that the hydrogen adsorbs on the surface covalently as an neutral atom. In the case of the covalent bonding, the bonding energy is attributed to the formation of the bonding state, not the Coulomb attraction between anions and cations. Therefore, in the case of covalent bonding, charge transfer from H 1s to the substrate is not necessary. This may explain the absence of changes in the Fe(B) t_{2g}-derived peak after H exposure on Fe(A)-terminated surface.

The change of work function is often explained by the change of electric dipole moment at the surface by adatom adsorption. The work function is defined as the minimum energy to remove an electron in the bulk to the vacuum, and is influenced by the surface dipole moment. If an adatom creates a dipole whose positive end is directed to the vacuum side, the potential barrier of outgoing electrons decreases which decreases the work function.

Although the present results indicate that the bonding between the surface and H is covalent and not ionic, there is a possibility that the covalent bonding generates a dipole moment. A similar phenomenon was reported for alkali atom adsorption by the first-principle calculation study by Ishida *et al.* [53]. The decrease of work function can be explained by the formation of dipole due to the polarization of Na atom due to the covalent bonding, not by forming an anion-cation pair by the ionic bonding. Figure 3.18 shows the contour plot of the calculated difference charge $\delta\rho(\boldsymbol{r}, \theta)$ of the chemisorbed Na atom on a jellium surface reported by ref [53]. The calculation was based on the local-density-functional theory combined with the norm-conserving pseudopotential. The difference charge is the change of charge distribution induced by the bonding of jellium and Na which is written as

$$\delta\rho(\boldsymbol{r}, \theta) = \rho(\boldsymbol{r}, \theta) - [\rho_{jel}(\boldsymbol{r}) + \rho_{jel}(\boldsymbol{r}, \theta)] \tag{3.1}$$

where $\rho(\boldsymbol{r}, \theta)$, $\rho_{jel}(\boldsymbol{r})$ and $\rho_{jel}(\boldsymbol{r}, \theta)$ are the electron charge densities of the Na-covered jel-

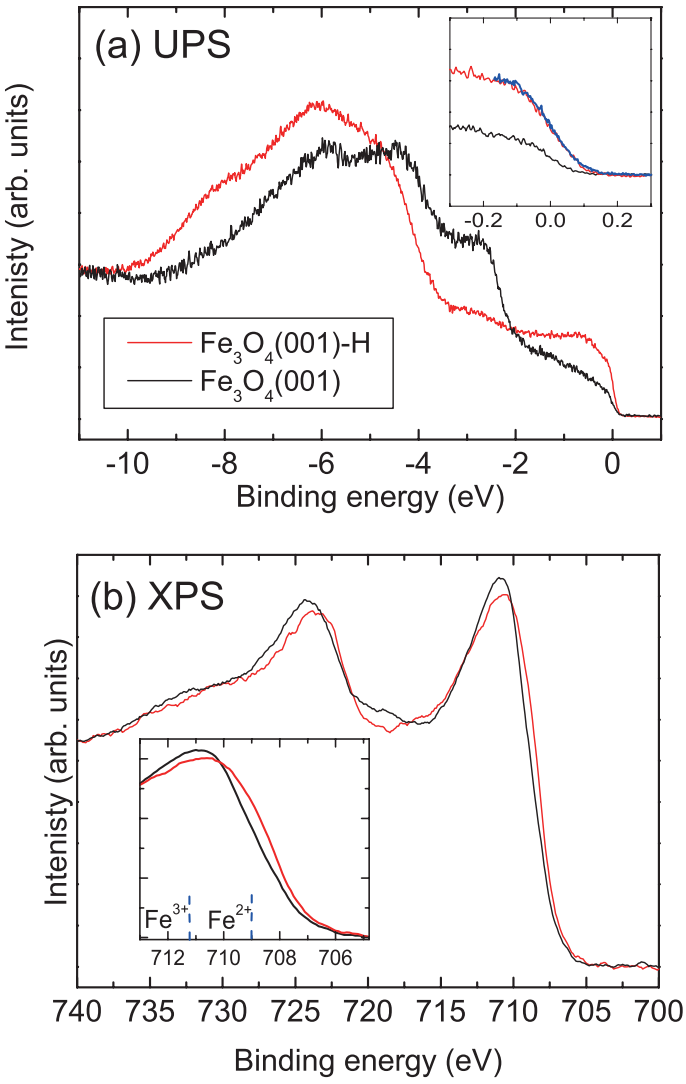

Figure 3.17: (a) UPS and (b) XPS spectrum of the Fe_3O_4 (001) surface before and after the atomic H exposure [17].

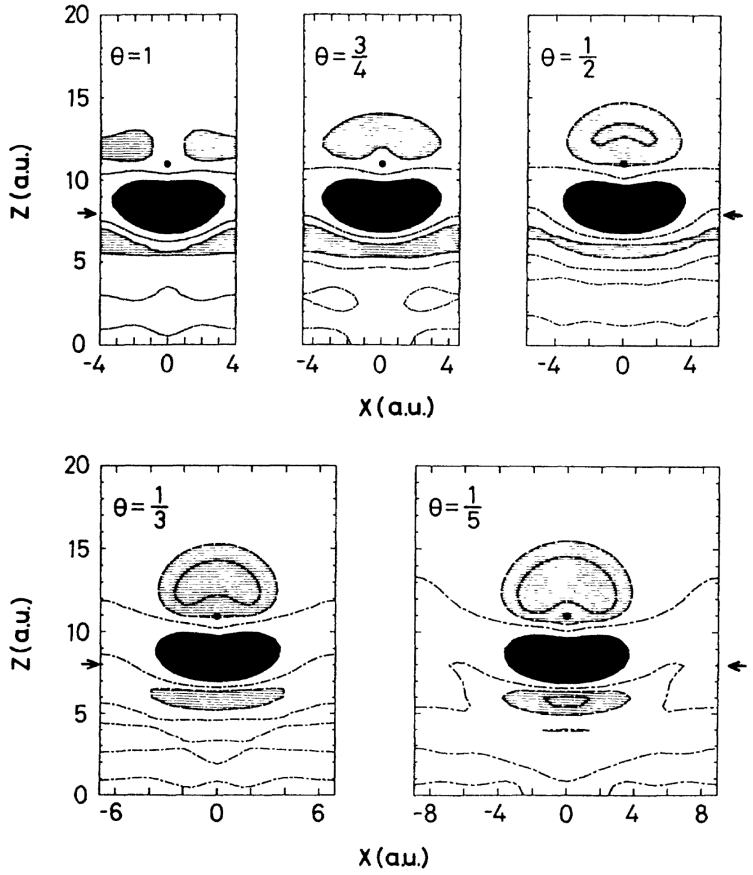

Figure 3.18: The contour plot of the calculated difference charge of the chemisorbed Na atom on a jellium surface [53].

lium, isolated jellium and the unsupported Na layer, respectively. θ denotes the coverage of Na. The solid circle shows the position of the Na atom and the arrow shows the jellium edge. The shaded and hatched area designate the regions where $\delta\rho(\boldsymbol{r},\theta) \geq 0.001$ a.u. (accumulation of the electron density) and $\delta\rho(\boldsymbol{r},\theta) \leq -0.0005$ a.u. (depletion of the electron density), respectively. The dashed-dotted curves correspond to $\delta\rho(\boldsymbol{r},\theta) = 0$. An electric dipole is formed around the neutral Na adatom due to the polarization of electron density of the Na atom. They considered that the origin of the polarization of the Na atom is due to the hybridization of the adatom and the substrate orbital. Our results on the H adsorption on the Fe(A)-terminated surface resembles this report in that there is no charge transfer while the work function decreases. The decrease of work function means that the dipole is formed with its positive end is directed to the vacuum side.

Figure 3.19 (a) shows a possible model of H adsorption on the Fe(A)-terminated surface. On the Fe(A)-terminated surface, Fe(A)1 and O1 atoms face the vacuum. Therefore, the H atom can be adsorbed on the Fe(A)1 or O1 atoms. The H atom is electrically polarized which cases decrease in the work function. A possible origin of the polarization is the hybridization of the H 1s orbital and the substrate orbital. Also there is possibility that the H 1s orbital is mixed with the H 2p orbital due to the perturbation by the electric field

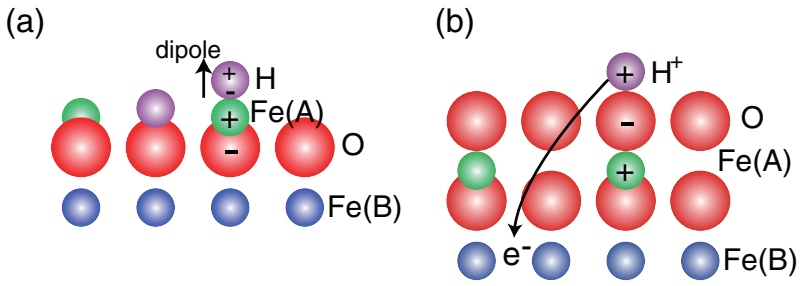

Figure 3.19: A possible model of H adsorption on Fe(A)-terminated surface. The blue, green, and red balls represent the Fe(B), Fe(A), and oxygen atoms.

from the substrate. Further investigation using the first-principle calculation is necessary to clarify in detail the mechanism of the H adsorption.

In the case of the O_2-exposed Fe(A)-terminated surface, the Fe(B) t_{2g}-derived peak increases by H+H_2 exposure. This indicates that the hydrogen provides an electron to the Fe(B) t_{2g} orbital, which means that the H adatom is ionized. In this case, the change of work function can be explained by the dipole formation by the H^+ adatom. The difference between the H adsorption mechanisms of the Fe(A)-terminated and the O_2-exposed Fe(A)-terminated surfaces is considered to be due to the difference in the amount of O atoms on the surface. Berdunov *et al.* reported that the Fe_3O_4 surface covered by a closed-packed O layer can be obtained by Ar^+ sputtering, annealing in UHV at 1000 K, annealing at 950 K in oxygen partial pressure of 1×10^{-6} mbar, and cooling down to room temperature in the oxygen atmosphere. Although this preparation procedure differs from our study in that they expose O_2 while cooling after annealing while we expose O_2 at room temperature, there is possibility that the O atoms are adsorbed on the Fe(A) termination. One of the possible models of H adsorption on the O_2-exposed Fe(A)-terminated surface is shown in figure 3.19 (b). Here, we supposed that a closed-packed O layer is formed by O_2 exposure. An ionized H atom is adsorbed on the O atom. The bonding between the H and O is ionic. The released electron of H atom is provided to the Fe(B) t_{2g} orbital.

3.2 Transport measurement

We investigated the effect of O_2 and H exposure on the surface electric resistance of the Fe(A)-terminated Fe_3O_4 (111) surface. The electric resistance was measured by micro four-point probe measurement. The Fe_3O_4 (111) surface was prepared by Ar^+ sputtering, annealing in UHV at 900 K for 10 min and annealing at 900 K in an O_2 partial pressure of $5\times10^{-}4$ Pa for 10 min. This surface is considered to be Fe(A)-terminated. The preparation was conducted in the preparation room of the chamber. During the preparation, the chamber was evacuated by a turbo molecular pump and a rotary pump. After preparation, we turned off the turbo molecular pump and the rotary pump since they case vibration noise. Simultaneously, we started evacuating the chamber with an ion pump. Subsequently, the sample was transfered to the measurement unit shown in figure 2.11. After cooling down the sample to the room temperature, we approached the micro four-point probe. Unfortunately, we noticed that two of the electrodes were broken during approaching. Therefore

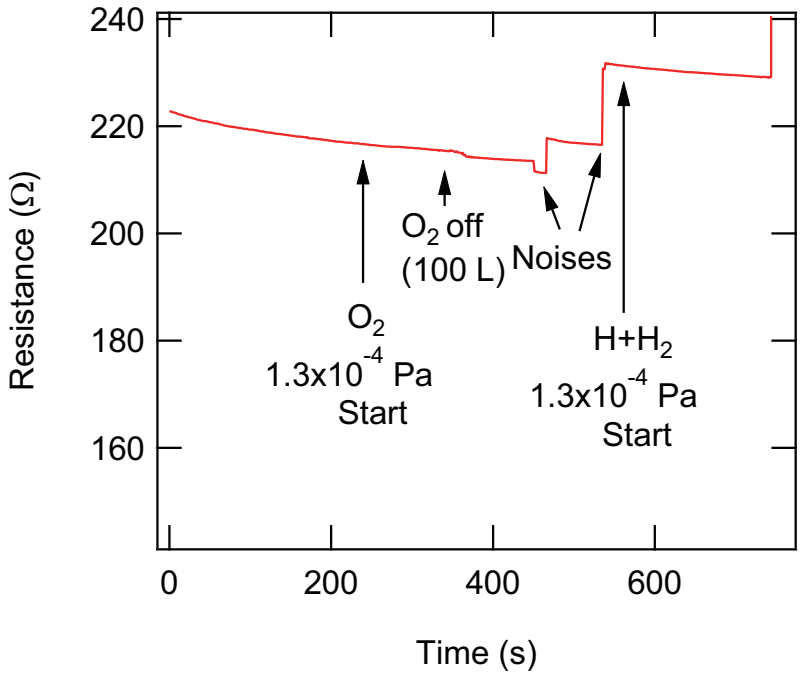

Figure 3.20: The evolution of the electric resistance of the Fe_3O_4 (111) surface by O_2 and H exposure.

we started measuring the resistance with two-probe method.

Figure 3.20 shows the evolution of the electric resistance of the Fe_3O_4 (111) surface by O_2 and H exposure at 300 K. The bottom axis is the time and the left axis is the electric resistance.The measurement was started at a time of 0 sec. At 240 sec, we introduced 1.3×10^{-4} Pa O_2 to the chamber. After exposing 100 L of O_2, we stopped the O_2 supply. At 560 sec, we introduced 1.3×10^{-4} Pa H_2 to the chamber. Atomic H was obtained by flowing 5A electric current to a tungsten filament with a diameter of 0.2 mm located 235 mm away from the sample. The jumps of the resistance at 450 sec, 535 sec and 743 sec are electrical noises due to the experimental errors. In this results, we did not find a significant change in the resistance by the O_2 and $H+H_2$ exposure.

3.3 Low-Energy Electron Diffraction

We investigated the temperature dependence of the surface structure by observing the LEED IV curve. The experiment was conducted with a home-made sample holder which can cool the sample to 15 K by liquid He and to 82 K by liquid N_2.

The (111) surface of a Fe_3O_4 single crystal was cleaned by Ar^+ sputtering, annealing at 1000 K, and annealing at 1000 K in an oxygen atmosphere of 5×10^{-6} mbar [45]. We consider that this surface is a stoichiometric Fe(A)1-terminated Fe_3O_4 (111) surface. Figure 3.21 is the LEED pattern of the Fe(A)1-terminated Fe_3O_4 (111) surface (a) below (89 K) and (b) above (410 K) the Verwey temperature. Both LEED patterns exhibit an unreconstructed 1×1 structure, and there is no significant difference between the two LEED patterns.

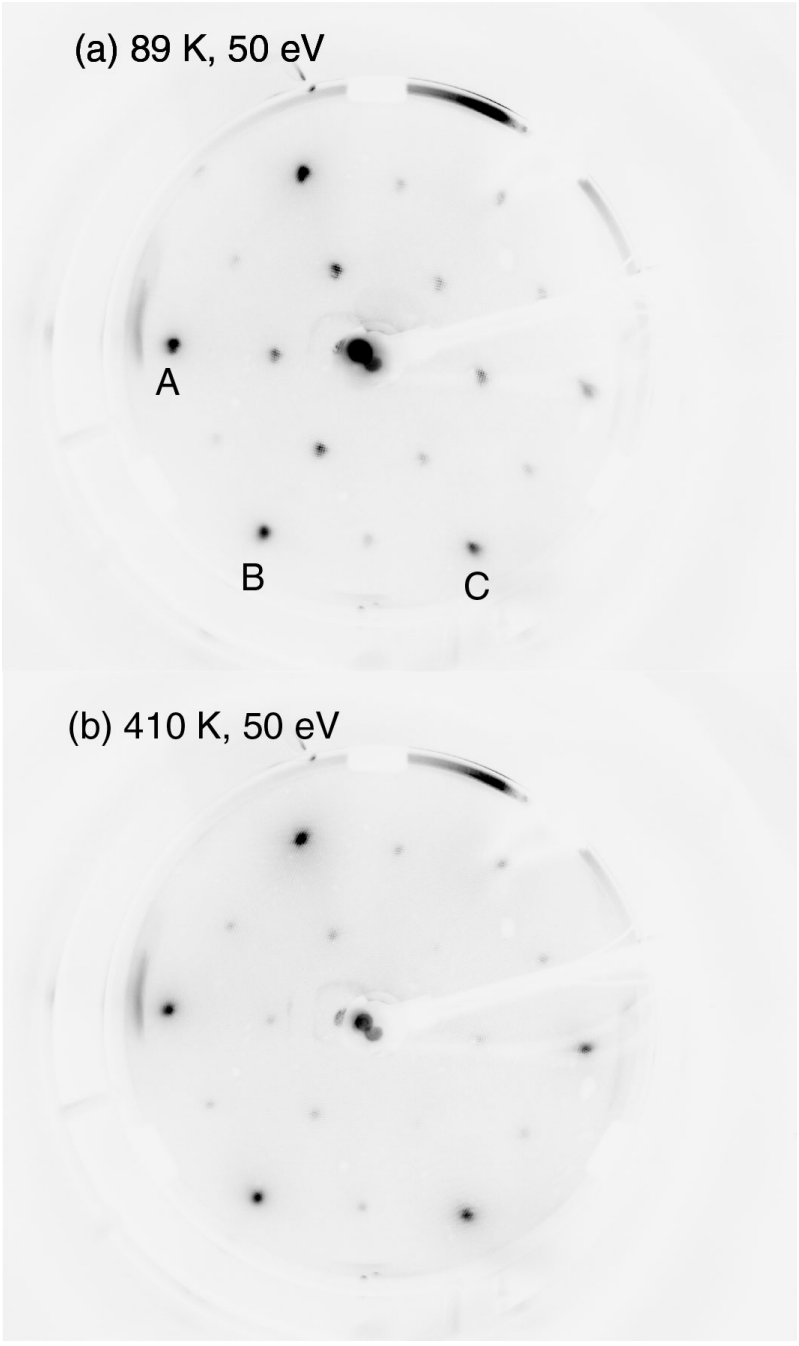

Figure 3.21: LEED pattern of the Fe(A)1-terminated Fe_3O_4 (111) surface (E = 50 eV) at (a) 89 K and (b) 410 K.

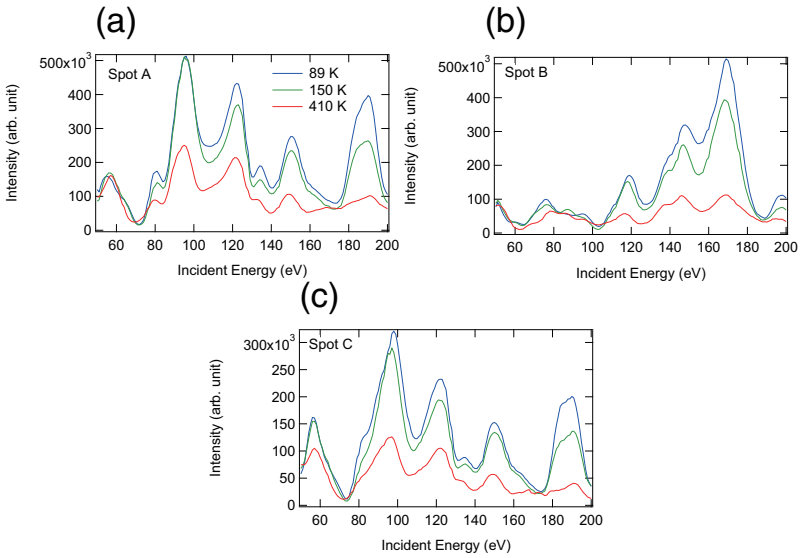

Figure 3.22: LEED-IV curves of the Fe(A)1-terminated Fe_3O_4 (111) surface at 85, 150–169 and 410 K for the spots A–C shown in figure 3.21 (a).

Figure 3.22 shows the LEED-IV curves of the Fe(A)1-terminated Fe_3O_4 (111) surface at 85, 150–169 and 410 K. The left and the bottom axes are the intensity and the incident electron energy. The three graphs correspond to the LEED spots labeled as spots A–C in figure 3.21 (a). The IV curve of spots A and C are similar. This means these spots are crystallographically equivalent. This is consistent with the fact that the Fe_3O_4 (111) has three-fold symmetry. The intensity decreases as the temperature increases. This is considered to be due to the Debye-Waller factor. No significant difference was observed between the peak position of the IV curve above and below the Verwey temperature. This may indicate that the surface structure does not change at the Verwey temperature. However, further studies including calculations of the multiple scattering are necessary in order to obtain the structural information from the IV curve.

3.4 Magnetic Structure of the Fe_3O_4 (111) Surface

In this study, we investigated the magnetic structure of the Fe_3O_4 (111) surface by CEMS and NRS. We observed the NRS spectra at room temperature to estimate the in-plane magnetic anisotropy. Furthermore, we investigated the temperature dependence of the internal magnetic field by high- and low-temperature NRS. We conducted CEMS experiments at room temperature in order to further clarify the magnetic structure.

3.4.1 Sample Fabrication

Since NRS and CEMS utilize the Mössbauer effect of ^{57}Fe, these methods selectively probe ^{57}Fe atoms. In this study, we used two samples. One is the Fe_3O_4 (111) surface with a natural isotope ratio which includes 98% ^{56}Fe and 2% ^{57}Fe. The other is the Fe_3O_4 (111) surface on which an epitaxial 4 nm $^{57}Fe_3O_4$ layer is deposited. In the case of CEMS whose

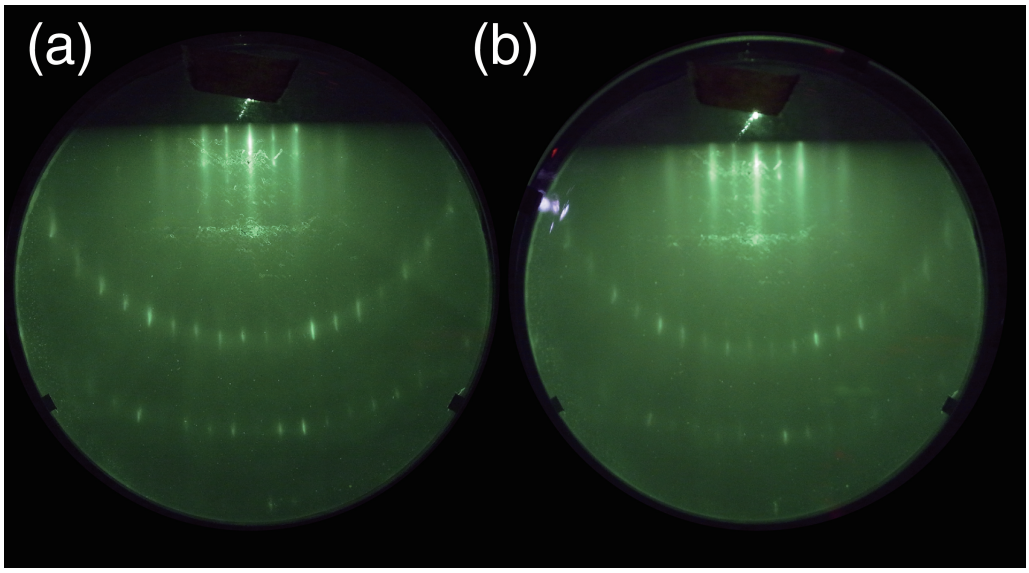

Figure 3.23: RHEED patterns ($E = 15.3$ keV) of (a) the Fe(A)-terminated and (b) the $^{57}Fe_3O_4$(4 nm)-deposited Fe_3O_4 (111) surfaces.

probing depth is 40–60 nm, it is possible to discuss the depth-dependence of the magnetic structure by comparing the spectra of the natural sample and the $^{57}Fe_3O_4$-deposited sample. For NRS whose probing depth is $\sim$ 2 nm, we used the $^{57}Fe_3O_4$-deposited sample in order to obtain higher signal intensity because the signal intensity is proportional to the density of ^{57}Fe atoms.

The 4 nm $^{57}Fe_3O_4$ layer was deposited on the (111) surface of a natural Fe_3O_4 single crystal in an ultra-high-vacuum (UHV) chamber with a base pressure of 1×10^{-10} mbar. The (111) surface of a Fe_3O_4 single crystal was cleaned by Ar^+ sputtering, annealing at 1000 K, and annealing at 1000 K in an oxygen atmosphere of 5×10^{-6} mbar [45]. The sample prepared by this procedure has a stoichiometric Fe(A)-terminated surfaces, which has been confirmed by STM studies[45, 54]. After cleaning, 4 nm of a $^{57}Fe_3O_4$ epitaxial layer was grown by depositing ^{57}Fe under an oxygen pressure of 8×10^{-6} mbar. The evaporation rate was approximately 0.2 nm/min, and the sample temperature was kept at 550 K. After deposition, the sample was annealed in UHV at 800 K for 10 min [55]. The surface crystallinity was checked by reflection high-energy electron diffraction (RHEED) before and after deposition. Figure 3.23 shows the RHEED pattern before and after deposition. No change in the RHEED pattern was observed except for the increase in the background intensity which is considered to be due to the disturbance of the surface crystallinity.

3.4.2 Nuclear Resonant X-ray Scattering

Reflectivity Measurement

The dependence of the X-ray reflectivity on the incidence angle was observed prior to the NRS measurement in order to determine the incidence angle. Figure 3.24 (a) shows the experimental geometry for the reflectivity curve measurement and the time spectrum

measurement. The slit is for defining the reflection angle and for cutting the noise photons reflected by the sample holder. The slit and the detector are mounted on the 2θ arm, and the sample is mounted on the θ arm of the goniometer. The reflectivity curve measurement is carried out by repeating the cycles of rotating the θ arm by 0.005°, rotating the 2θ arm by 0.01° and counting the APD signal for 50 sec. The positions and the directions of the sample, detector, slit, and the goniometer are carefully adjusted in advance so that the incident X-ray constantly irradiate the sample and the reflected X-ray strikes the APDs while sweeping the incidence angle. The resonantly scattered X-ray can be observed as the delay signal. The intensity of the delay signal peaks near the critical angle for the total reflection where the intensity of the evanescent field is maximum [37, 56]. The critical angle for the total reflection can be estimated by [34]

$$\phi_c = \left[n\lambda^2 r_0 Z/\pi \right]^{\frac{1}{2}} \tag{3.2}$$

where n is the atomic density, λ is the wavelength of the incident beam, r_0 is the classical electron radius, and Z is the atomic number. The classical electron radius r_0 is 2.8×10^{-15} m. We used the values $n = 9.45 \times 10^{28}$ m^{-3}, $Z = 33.14$ and $\lambda = 8.60 \times 10^{-11}$ m. Z was calculated by taking the average of all the components in the unit formula. λ is calculated from the photon energy (14.413 keV). From equation 3.2, the ϕ_c of Fe_3O_4 is estimated to be 0.18°.

Figure 3.24 (b) shows an example of the dependence of the prompt and delay signal intensity on the angle of incidence with the incidence direction parallel to the [10$\bar{1}$] direction. It takes about three hours to obtain this spectrum. The intensity of the delay signal peaks at 0.18° which is in good agreement with the estimation by equation 3.2.

Azimuthal Angle Dependence of the Time Spectra

The azimuthal angle dependence of the time spectra of the nuclear resonant scattered X-ray was observe in order to investigate the in-plane magnetic anisotropy. The time spectra was obtained for six incident azimuthal directions which are parallel to the [01$\bar{1}$], [11$\bar{2}$], [10$\bar{1}$], [2$\bar{1}\bar{1}$], [1$\bar{1}$0], and [1$\bar{2}$1]. The measurement was conducted without the sample preparation procedure since sputtering and annealing reduces the signal intensity drastically. The reflectivity measurement was conducted before the each time spectrum measurement in order to set the glancing angle at the critical angle for the total reflection where the delay signal intensity is maximum. The glancing angle determined by the reflectivity curve was 0.12–0.3°.

Figure 3.25 shows the time spectra of the air-exposed $^{57}Fe_3O_4$(4 nm)-deposited Fe_3O_4 (111) surface with six incident azimuthal angles. Each measurement required about 10 hours. The spectra exhibit clear oscillations of quantum beats. The decay time of the time spectra includes contributions of the natural life time of the $I = 3/2$ first excited state and the speed-up effect due to the dynamical effect (cf. equations 2.42 and 2.45). The time spectra was frequency-analyzed by the maximum entropy method (MEM) [57]. Figure 3.26 shows the NRS frequency spectra obtained by MEM. Since the intensity is weak in the $t > 140$ ns region, we used the data pints at 0 ns<t< 140 ns for the MEM calculation. Therefore, it is difficult to distinguish the two peaks whose interval is less than $1/140$ ns^{-1}($\simeq$7.1 MHz).

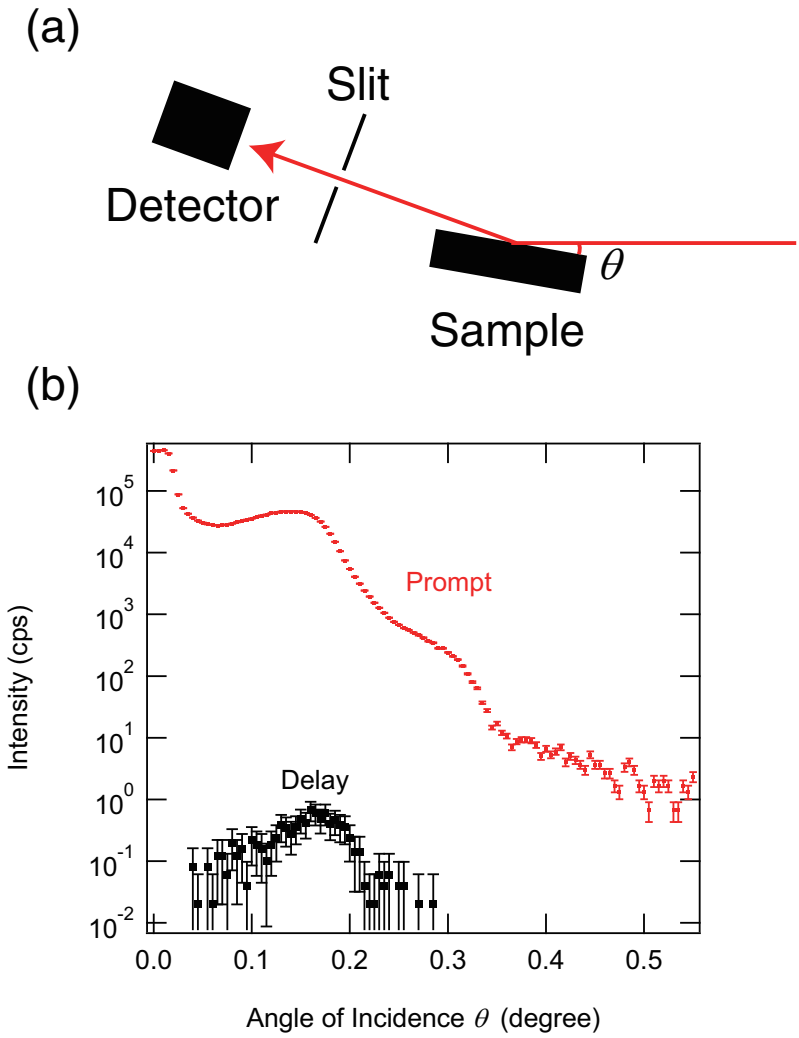

Figure 3.24: (a) The experimental geometry for the reflectivity measurement. (b) The dependence of the prompt and delay signal intensity on the angle of incidence. The red and the black line show the intensity of the prompt and the delay signal, respectively.

Based on the discussion in section 2.7, we focus on the $\omega_{1,6}$ and $\omega_{2,5}$ component of the frequency spectra (cf. Figure 2.13 and 2.18). Using the hyperfine magnetic field B_{hf} and equation 2.35, the Zeeman splitting can be written as $\mu_N g_N (I = 1/2) I_z B_{hf}$ and $\mu_N g_N (I = 3/2) I B_{hf}$ for the ground and the excited states, respectively. The frequency of the quantum beat oscillation can be written as

$$\begin{aligned} \omega_{i,j} &= \Delta E_{i,j}/\hbar \\ \Delta E_{1,6} &= (\mu_N g_N (I = 1/2) \times 1 - \mu_N g_N (I = 3/2) \times 3) \times B_{hf}, \\ \Delta E_{2,5} &= (\mu_N g_N (I = 1/2) \times 1 - \mu_N g_N (I = 3/2) \times 1) \times B_{hf}, \\ \Delta E_{1,3} &= (-\mu_N g_N (I = 3/2) \times 2) \times B_{hf}., \end{aligned} \tag{3.3}$$

where $\omega_{i,j}$ is the beat angular frequency due to the interference of the transition lines i and

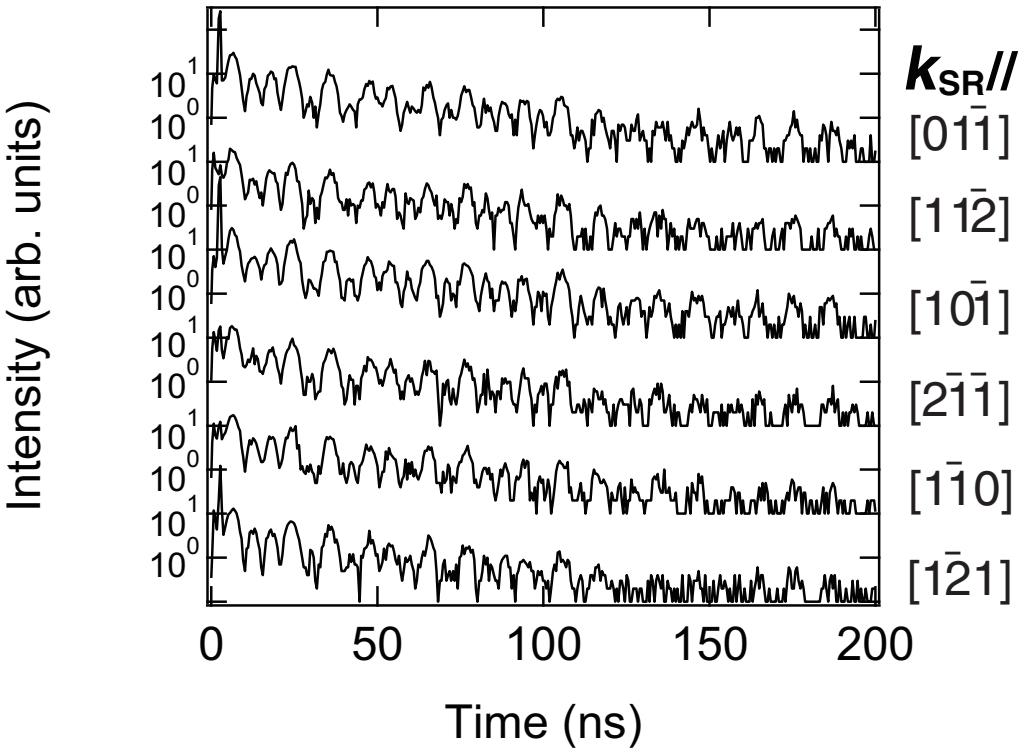

Figure 3.25: The NRS time spectra of the $^{57}Fe_3O_4$(4 nm)-deposited Fe_3O_4 (111) surface taken with six incident azimuthal directions.

j, h is the Planck constant, and $\Delta E_{i,j}$ is the energy difference between the transition lines i and j. Using the values of μ_N and g_N shown in table 2.2 and the reported values for B_{hf} which are 48.80 T and 45.73 T for the Fe(A) and Fe(B) site [58], respectively, the peaks corresponding to $\omega_{1,6}$, $\omega_{2,5}$, and $\omega_{1,3}$ components are expected to appear at 181.8 MHz, 105.3MHz, and 76.6 MHz for the Fe(A) site, and 170.3 MHz, 98.7 MHz, and 71.8 MHz for the Fe(B) site, respectively.

The frequency spectra shown in figure 3.26 have peaks at 71 MHz, 98–100 MHz, 103–105 MHz, 171-174 MHz, and 180-184 MHz. The first component agrees well with the expected value of $\omega_{1,3}(=\omega_{4,6})$ for the Fe(B) site. The second and the third peaks are assigned to the $\omega_{2,5}$ component of the Fe(B) and Fe(A) site, respectively. The fourth and the fifth peaks are assigned to the $\omega_{1,6}$ component of the Fe(B) and Fe(A) site, respectively. The $\omega_{1,3}$ component for the Fe(A) site was not observed. The possible explanation is that the difference of the $\omega_{1,3}$ values of the Fe(A) and Fe(B) sites, which is estimated to be 4.8 MHz, is smaller than the resolution of the frequency analysis ($\simeq$7.1 MHz). The hyperfine magnetic field B_{hf} estimated from the observed frequency $\omega_{1,6}$ is 48.8 ± 0.5 T and 46.3 ± 0.4 T. These values are in good agreement with the previous reports [58, 39]. This is the evidence that the deposited layer is a stoichiometric Fe_3O_4 layer.

Figure 3.27 shows the azimuthal angle dependence of the intensity of the NRS frequency components of the $^{57}Fe_3O_4$(4nm)/Fe_3O_4 (111) surface. As shown in section 2.7, if there is an in-plane magnetic anisotropy, the intensities of the $\omega_{1,6}$ and $\omega_{1,3}$ components will have strong azimuthal angle dependence: The $\omega_{1,6}$ and $\omega_{1,3}$ components will be intense when the magnetization direction of the surface is parallel to the electric field of

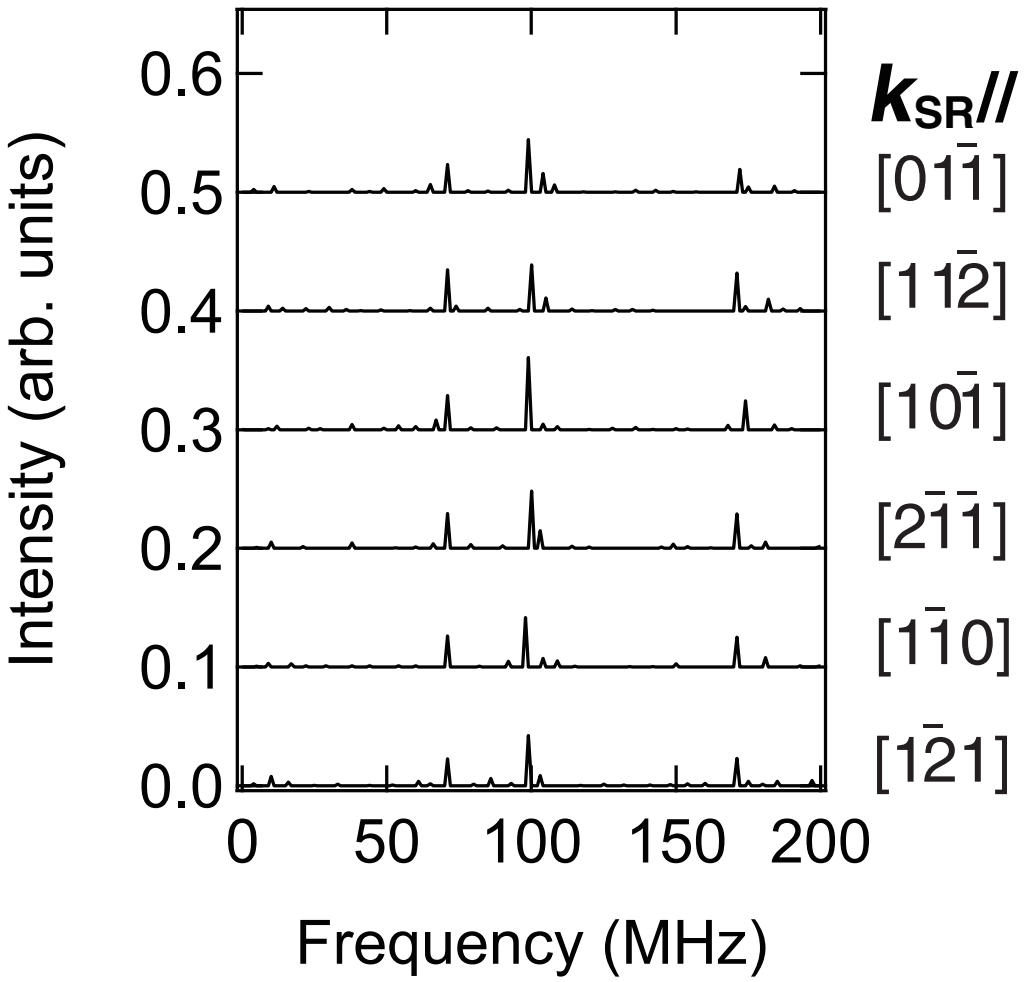

Figure 3.26: The azimuthal angle dependence of the NRS frequency spectra obtained by analyzing the time spectra with the maximum entropy method.

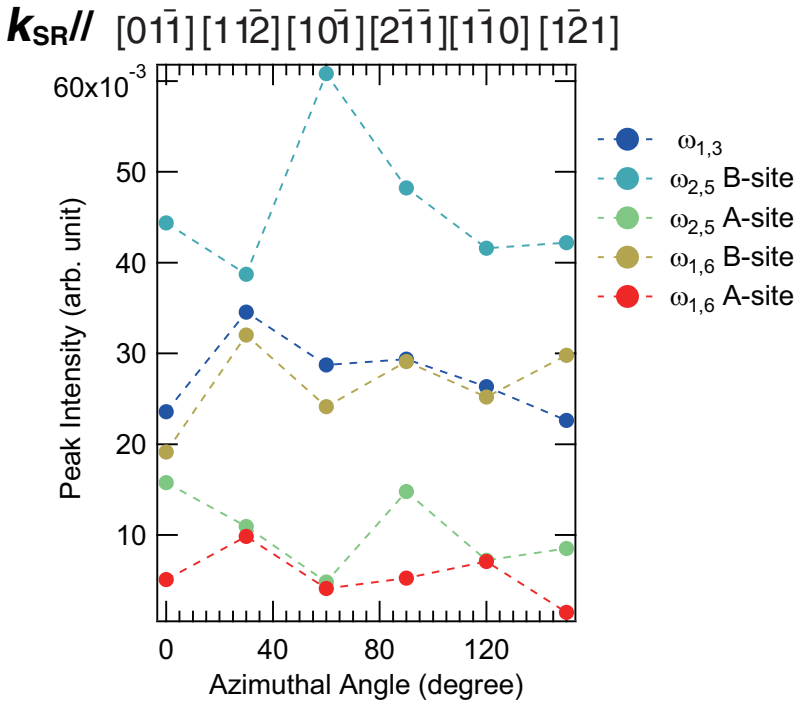

Figure 3.27: Azimuthal angle dependence of the intensity of the NRS frequency components of the $^{57}Fe_3O_4$(4nm)/Fe_3O_4 (111) surface.

the incident X-ray. However, the intensities of $\omega_{1,6}$ and $\omega_{1,3}$ components shown in figure 3.27 does not have clear azimuthal angle dependence. Although the exact direction of surface magnetization is unknown, it is likely that there are three non-perpendicular magnetization directions on the Fe_3O_4 (111) surface since the crystal structure and also the bulk easy-magnetization axes of Fe_3O_4 has three-fold symmetry along the [111] axis. The absence of azimuthal angle dependence indicates that the domains with three non-perpendicular magnetization directions are equally dominant on the surface.

Temperature Dependence of NRS Spectra

Figure 3.28 shows the time spectra of the nuclear resonant scattered X-ray taken at 85 K, 297 K and 500 K. The data of 85 K and 297 K were taken with the sample holder for the low-temperature NRS sample holder and the 500 K data was taken with high-temperature NRS sample holder. In order to avoid the desorption of oxygen, the measurement at 500 K was conducted in the oxygen partial pressure of $1 \times 10^{-}4$ Pa. The frequency of the quantum beat varies with the temperature. Figure 3.29 shows the corresponding frequency spectra obtained by maximum entropy method (MEM) analysis. For 85 K, peaks appeared at 177 and 187 MHz which are considered to correspond to the $\omega_{1,6}$ component of the Fe(B) and Fe(A) sites. For 297 K, peaks appeared at 171 and 184 MHz. On the other hand, for 500 K, three peaks appeared at 156, 164, and 178 MHz. The internal magnetic field B_{hf} was estimated from these frequencies. The error bar due to the uncertainty of the MEM analysis was 0.7 T. Figure 3.30 shows the temperature dependence of the internal magnetic field B_{hf} obtained from the present experimental data and the bulk

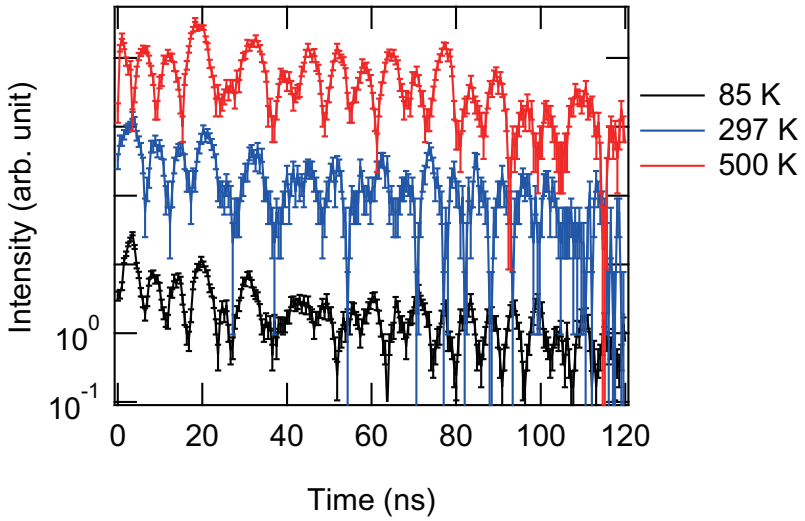

Figure 3.28: The NRS time spectra of the air-exposed $^{57}Fe_3O_4$(4nm)/Fe_3O_4 (111) surface at 85 K, 297 K and 500 K

internal magnetic field measured by transmission Mössbauer spectroscopy on powdered Fe_3O_4 reported by Häggström *et al.* [59]. The original Mössbauer spectra are shown in figure 3.31. In their study, they claimed that the component of Fe(B) consists of two components which derives from two magnetically inequivalent Fe(B) sites. The two Fe(B) which are denoted as Fe(B_a) and Fe(B_b) in figure 3.30 have different internal magnetic field due to the difference in the magnetic dipole interaction.

As shown in figure 3.30, the values of B_{hf} agree well with the previous report for 85 K and 297 K, but deviate significantly at 500 K, which suggest that the phase transition of the Fe_3O_4 (111) surface is different from the bulk. It is difficult for MEM analysis to distinguish the two components of B_{hf} whose interval is smaller than 1.9 T which corresponds to the inverse of the time window ($1/140$ ns$^{-1}\simeq$7.1 MHz). This explains the reason why the Fe(B_a) and Fe(B_b) components are not resolved in the NRS data for 85 and 297 K in figure 3.30. For 500 K, three frequency components were detected. On possible interpretation is that the the two peaks of Fe(B) were resolved at 500 K: The difference between the internal magnetic field of the surface Fe(B_a) and Fe(B_b) sites is larger at 500 K than 297 and 85 K. There is also a possibility that the existence of three peaks is due to the difference of the internal magnetic field between the surface and the bulk: The smallest B_{hf}(=41.8 T) is derived from the bulk Fe(B) site, the middle component (44.0 T) is from the bulk Fe(A) site or the surface Fe(B) site, and the largest B_{hf}(=47.9 T) is from the surface Fe(A). It is obvious that the component at B_{hf} = 47.9 T is larger than any of the bulk components, which clearly indicates the existence of a surface magnetic structure whose internal magnetic field is larger than the bulk.

3.4.3 CEMS

Figure 3.32 (a) and (b) show the CEMS spectra of natural and $^{57}Fe_3O_4$(4 nm)-deposited Fe_3O_4 (111) surfaces, respectively. The incident γ-ray direction was parallel to the [111] direction. The spectra consist of 12 peaks which are assigned to the six excitation lines

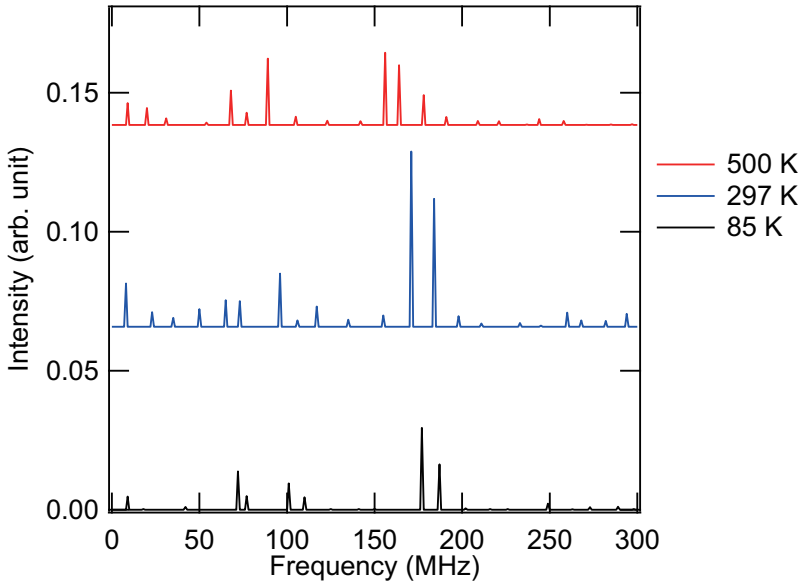

Figure 3.29: The frequency spectra of the NRS time spectra of the air-exposed $^{57}Fe_3O_4$(4nm)/Fe_3O_4 (111) surface at 85 K, 297 K and 500 K.

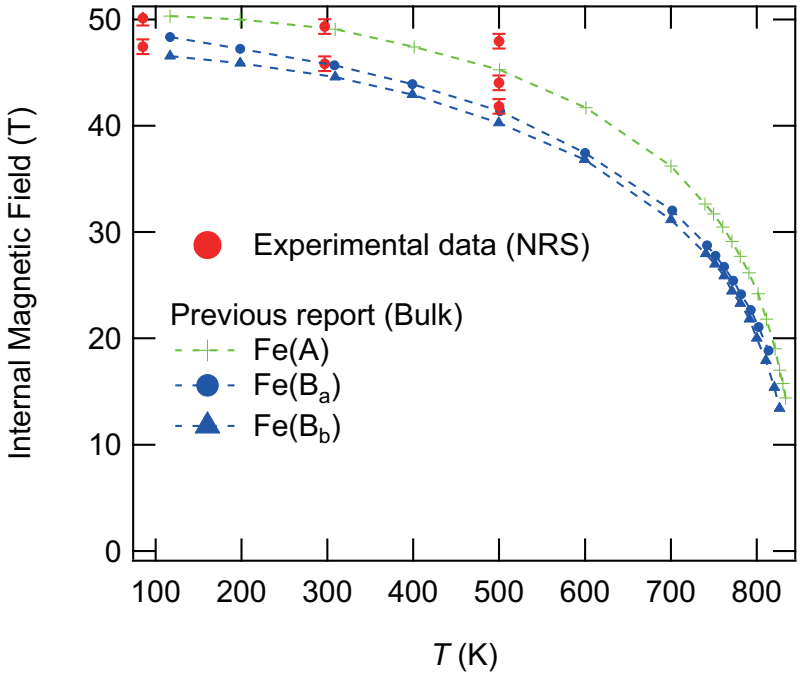

Figure 3.30: The temperature dependence of the internal magnetic field B_{hf}. Black points show the values estimated from the NRS spectra. Dotted lines show the data of the previous report [59].

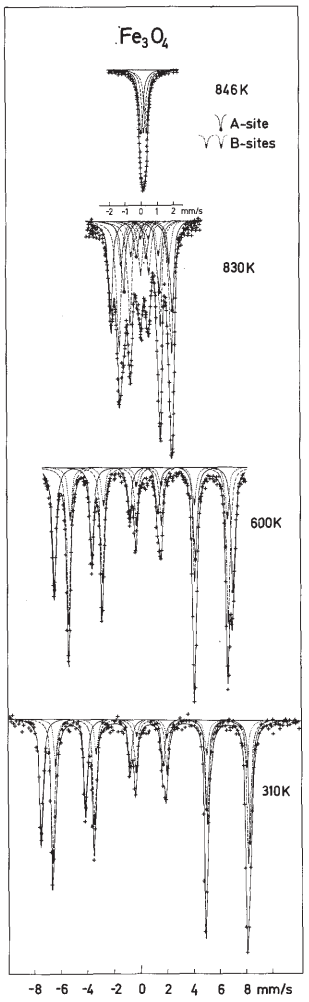

Figure 3.31: Mössbauer spectra of powder Fe_3O_4 recorded at 310 K, 600 K, 830 K and 846 K [59].

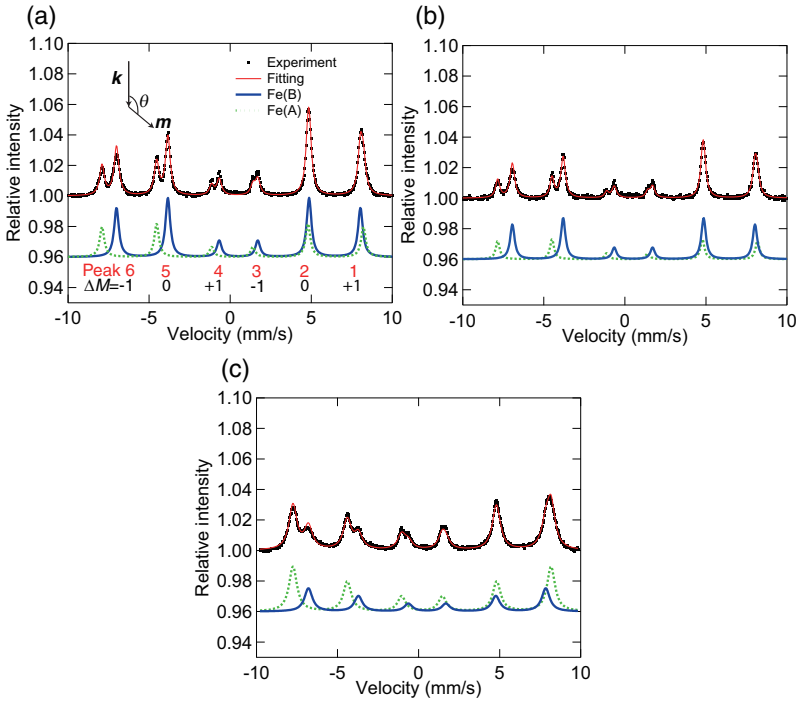

Figure 3.32: Conversion electron Mössbauer spectra (CEMS) of (a) the natural Fe_3O_4 (111) surface, (b) $^{57}Fe_3O_4$(4 nm)/Fe_3O_4 (111), and (c) powder Fe_3O_4. Dots present the experimental data, and lines show the spectrum components of Fe(A) (green) and Fe(B) (blue) obtained by fitting.

shown in figure 2.13 for the Fe(A) and Fe(B) sites. The peaks labeled as peaks 1–6 in figure 3.32 (a) correspond to the transitions 1–6 in figure 2.13. In order to estimate the peak intensities, the spectra were analyzed by fitting the data with Lorentzians. The fitting was based on the assumption $W_{1,6} = 3W_{3,4}$ where W_1–W_6 are the intensity of the peak 1–6(cf. equation 2.39) [60]. The fitting results are represented by solid curves in figure 3.32. The blue, green and the red lines show the component of Fe(B), Fe(A) and the sum of Fe(A) and Fe(B), respectively.

The spectral intensity ratios Fe(B)/Fe(A) were 1.76 and 2.20 for the natural and $^{57}Fe_3O_4$-deposited samples, which are different from the stoichiometric ratio of 1.88 [61]. Although the reason for this discrepancy is not clear at present, it has been discussed in terms of slightly included Fe(B) vacancies; When an Fe(B) vacancy is created, it traps the electron of 5 B-site Fe^{3+} ions [62]. These trapped B-site Fe^{3+} ions are indistinguishable from the Fe(A) sites, which leads to the decrease of the observed Fe(B)/Fe(A) ratio. The Fe(B)/Fe(A) ratios observed in our experiment indicate that the possible number of the Fe(B) vacancies in the $^{57}Fe_3O_4$-deposited sample is less than that of the natural sample by 1.5%, which can be neglected in the present study. The estimated internal magnetic field was 48.6 and 45.5 T for the Fe(A) and Fe(B) sites, respectively. These values are the same for both the natural and $^{57}Fe_3O_4$-deposited samples and are consistent with previous reports [63, 64]. As seen in figure 3.32, the ratio of the line intensities is different between the two samples. Using the equation 2.39, the spin direction of each site can be determined from the line intensity ratios. We also observed the CEMS spectrum of a randomly oriented powder Fe_3O_4, which is shown in figure 3.32(c). For the powder sample, the line intensity ratio W_5/W_6 is 0.67 for both Fe sites, which is in good agreement with the theoretical value ($W_5/W_6 = 2/3$) of magnetically randomly oriented samples. In contrast, W_5/W_6 of the Fe_3O_4 (111) surface obtained from figure 3.32(a) and (b) was found to be 1.10–1.20, which is significantly different from 0.67. This means that the magnetization of the Fe_3O_4 (111) surface is not randomly oriented. This is not surprising since Fe_3O_4 has easy-magnetization axes due to the magnetocrystalline anisotropy energy. However, if the four easy-axes are equally dominant, the line intensity ratio W_5/W_6 will be 0.67. The deviation of line intensity ratio W_5/W_6 from 0.67 means that the four easy-axes are not equally dominant.

The dependence of the line intensities W_{1-6} on the effective angle (θ) between the magnetization direction and the X-ray incident direction is given by equation 2.39. Given that the easy-magnetization axes of Fe_3O_4 is the $\langle 111 \rangle$ axes, there are one surface-normal magnetization axis and three non-perpendicular axes, as illustrated in figure 3.33.

If the magnetization of the surface is perpendicular to the surface, which corresponds to $\theta = 0°$, the observed line intensity ratio W_5/W_6 will be 0. If the magnetization is along either of the non-perpendicular easy magnetization axes ($\left[1\overline{1}1\right]$, $\left[\overline{1}11\right]$, and $\left[\overline{11}1\right]$; $\theta = 109.5°$), on the other hand, W_5/W_6 will be 1.07. Also, W_5/W_6 has a maximum ($W_5/W_6 = 1.33$) at $\theta = 90°$. These indicate that W_5/W_6 will lie between 0 and 1.07 if the perpendicular and non-perpendicular component coexist. We should note that we cannot distinguish the two magnetization directions that are anti-parallel to each other (e.g., $\theta = 109.5°$ and $\theta = 289.5°$) and the two magnetization directions that are symmetric with respect to the surface (e.g., $\theta = 109.5°$ and $\theta = 70.5°$) since equation 2.39 contains only $\sin^2\theta$ and $\cos^2\theta$.

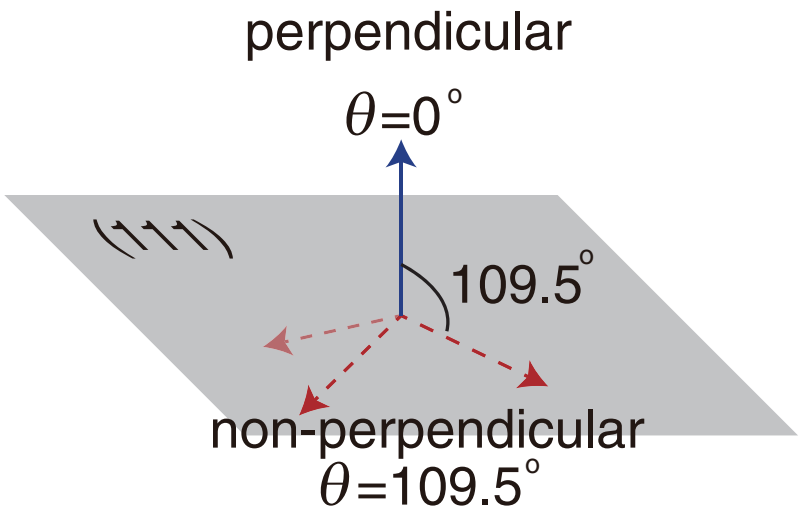

Figure 3.33: The bulk easy magnetization axes of Fe_3O_4.

Table 3.1: The W_5/W_6 intensity ratios of the CEMS spectra in figure 3.32 and the effective angle θ for each Fe site of the natural and $^{57}Fe_3O_4$-deposited Fe_3O_4 (111) surfaces.

	Natural Fe_3O_4	$^{57}Fe_3O_4$(4 nm)/Fe_3O_4
W_5/W_6(A-site)	1.10 ± 0.06	1.09 ± 0.12
W_5/W_6(B-site)	1.20 ± 0.03	1.18 ± 0.07
θ_A	107.9° ± 1.8°	108.3° ± 4.1°
θ_B	103.1° ± 1.5°	104.0° ± 2.7°
θ_{total}	96.4 ± 3.5	97.7 ± 6.1

Table 3.1 shows the W_5/W_6 values of the natural and $^{57}Fe_3O_4$-deposited Fe_3O_4 (111) surfaces and the effective angle (θ) of the magnetization direction calculated by equation 2.39. For both surfaces, the W_5/W_6 values are close to 1.07. The NRS results in figure 2.18 and 3.27 showed the presence of the $\omega_{2,5}$ component which indicates the presence of in-plane component of the magnetization. The lack of in-plane magnetic anisotropy in the frequency spectra indicates that the sample as a whole has no in-plane magnetic anisotropy. This indicates that the in-plane magnetization components cancel each other out. The W_5/W_6 values in table 3.1 was close to or slightly larger than the W_5/W_6 value corresponding to the non-perpendicular easy-axes (1.07). This indicates that the magnetization direction of the Fe_3O_4 (111) surface is identical to the non-perpendicular easy axes or more surface parallel than the non-perpendicular axes. If the surface contains both non-perpendicular and perpendicular easy-axes components, the observed W_5/W_6 value will be between 0 and 1.07. Therefore, the present results show that there are no perpendicular component within the probing depth of CEMS (45–60 nm). These results indicate that the surface is covered by closure domains, because if closure domains do not exist on the surface, the surface will contain body domains which are magnetized along the perpendicular easy axis.

Discussions

The results shown in table 3.1 show that the Fe_3O_4 (111) surface is covered with closure domains and the body domains magnetized along the perpendicular easy-axes are hidden below the closure domains. This tendency is consistent with a previous report by Özdemir *et al.* [20] which claimed that the Fe_3O_4 (111) surface is covered with closure domains. From the θ_A and θ_B values, the angle θ_{total} of the total magnetic moment can be calculated, which is also shown in table 3.1. We can notice that θ_{total} is significantly smaller than 109.5°, which means that the total magnetization direction is significantly rotated from the original non-perpendicular easy axes to the surface-parallel direction. This can be attributed to the competition between the magnetostatic energy and the magnetocrystalline anisotropy energy because the former tends to make the magnetization direction parallel to the surface and the latter tends to bind the magnetization direction to the easy-axes. Moreover, it can be noticed from table 3.1 that the observed magnetization direction is hardly influenced by the $^{57}Fe_3O_4$ deposition. This indicates that the magnetic structure does not have depth dependence since the contribution of the 4nm $^{57}Fe_3O_4$ layer to the CEMS signal is enhanced by a factor of 50 while the probing depth for the natural sample is 45–60 nm. This tendency is again consistent with a previous report by Özdemir *et al.* [20] which claimed that the magnetization direction of the closure domain is more surface parallel than the non-perpendicular easy axes. They considered that the decrease in θ_{total} is attributed to the magnetostatic energy that originates from the surface magnetic poles. Moreover, the angle θ_{total} observed in our study was hardly changed by $^{57}Fe_3O_4$ deposition within the experimental resolution, which indicates that the magnetization direction does not have depth dependence in the range of the probing depth of CEMS (45–60 nm). If we assume that the whole closure domain is uniaxially magnetized and that the magnetization direction is on the planes spanned by the perpendicular ([111]) and one of the non-perpendicular ([$\bar{1}$11], [1$\bar{1}$1] and [11$\bar{1}$] directions), the total energy E_{total} can be writ-

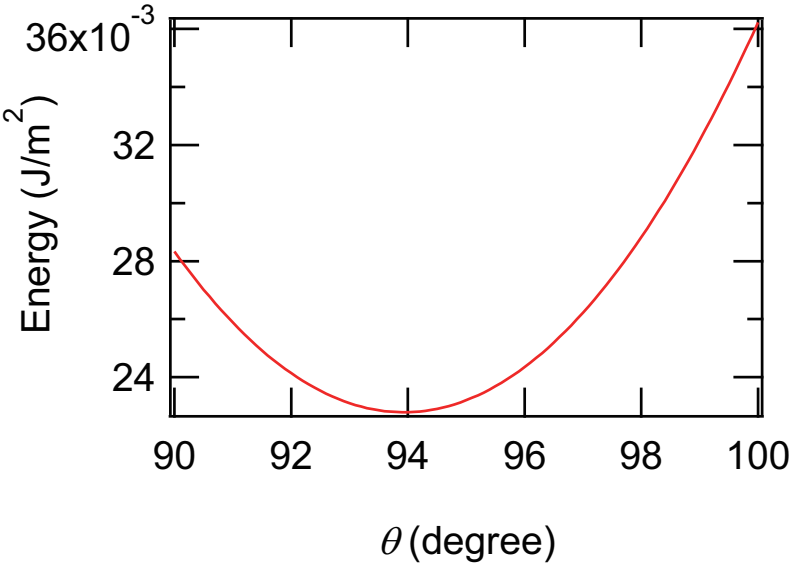

Figure 3.34: The dependence of E_{total} on the angle θ.

ten, from equations 1.22 and 1.16, as

$$\begin{aligned} E_{total} &= E_a + E_m \\ E_a &= K_1(V_c)(\alpha_1^2\alpha_2^2 + \alpha_2^2\alpha_3^2 + \alpha_3^2\alpha_1^2 - 1/3) \\ \alpha_1 &= \alpha_2 = \frac{-\cos\theta}{\sqrt{3}} + \frac{\sin\theta}{\sqrt{6}} \\ \alpha_3 &= \frac{-\cos\theta}{\sqrt{3}} - 2\frac{\sin\theta}{\sqrt{6}} \\ V_c &= \frac{1}{2}A\cos\theta \\ E_m &= 8.53\times10^{-8}M_s^2\cos^2\theta AL \end{aligned} \tag{3.4}$$

where A is the area of the sample surface, L is the width of the closure domains and V_c is the volume of the closure domains. The dependence of E_{total} on the angle θ is plotted in figure 3.34. The total energy E_{total} takes the minimum value at $\theta = 93.9°$. Although it is smaller than the observed θ in table 3.1, it shows that the magnetostatic energy cannot be neglected when we consider the surface magnetization direction.

Table 3.1 also shows that the magnetization of the Fe(A) site is almost parallel to the easy axes while the magnetization direction of Fe(B) is significantly different from the original easy axes ($\theta = 109.5°$). This indicates that the Fe(A) and Fe(B) spins are not parallel to each other at the surface.

We discuss the reason why the Fe(A) and Fe(B) spins are non-parallel to each other. Here, let us consider two ways to rotate the total magnetization direction in order to reduce the magnetostatic energy. One is to rotate both Fe(A) and Fe(B) spins to the surface-parallel direction. The other is to rotate only the Fe(B) spins. We label these spin configurations as configuration X and Y, respectively. These models are illustrated in figure 3.35. The angle θ between the total magnetization direction and the surface normal

direction is written as

$$\theta = \arccos\left(\frac{-\cos\theta_A + (9/5)\cos\theta_B}{\sqrt{(-\cos\theta_A + (9/5)\cos\theta_B)^2 + (-\sin\theta_A + (9/5)\sin\theta_B)^2}}\right), \tag{3.5}$$

where θ_A and θ_B are the angles corresponding to the magnetization direction of Fe(A) and Fe(B) sites, respectively. Let us consider the energy required to rotate the total magnetization direction by 10°. In configuration X, both Fe(A) and Fe(B) has to rotate by 10° in order to rotate the total magnetization direction by 10°. Configuration X costs no exchange energy since the Fe(A) and Fe(B) spins remains to be parallel. In configuration Y, in which only Fe(B) spins rotate, the Fe(B) spin rotation angle required to rotate the total magnetization direction by 10° is 4.9° since the magnetic moment of Fe(B) site is 9/5 times as large as that of Fe(A): Fe(A) spins do not rotate and Fe(B) rotates by 4.9°. This means that configuration Y costs smaller magnetocrystalline anisotropy energy than configuration X, but costs exchange energy because Fe(A) and Fe(B) spins become non-collinear. Therefore, the choice between two canting models depends on the competition between the exchange energy and the magnetocrystalline energy. Since the contribution of respective Fe sites to the magnetocrystalline anisotropy energy is unknown at present, it is difficult to estimate the magnetocrystalline anisotropy energy when the Fe(A) and Fe(B) spins are not parallel. Still, we can discuss by roughly estimating the magnetocrystalline anisotropy energy and the exchange energy.

In the case of configuration X, the increase of the anisotropy energy required to rotate the Fe(A) and Fe(B) by 10° estimated from equation 1.16 is 3×10^2 J/m^3. In configuration Y, on the other hand, the Fe(B) spin has to rotate towards the surface-parallel direction by 4.9° in order to rotate the total magnetization direction by 10°. From equation 1.1, the increase of the exchange energy $\Delta E_{exchange}$ per unit volume by rotating the Fe(B) spin is estimated as

$$\Delta E_{exchange} = -2n_B N J_{AB} S_A \cdot S_B(1 - \cos\Delta\theta_B), \tag{3.6}$$

where $n_B = 4.73 \times 10^{28}$ m^{-3} is the number of Fe(B) sites per unit volume, $N = 6$ is the number of the nearest Fe(A) sites of the Fe(B) site, $S_A = 5/2$ and $S_B = 9/4$ are the total spin quantum number of the Fe(A) and Fe(B) sites, respectively, and $\Delta\theta_B$ is the rotation angle of the Fe(B) site. By substituting $\Delta\theta_B = 4.9°$, $\Delta E_{exchange}$ is estimated to be 3.5×10^6 J/m^3 which is larger than the energy required to rotate the total magnetization direction by 10° in configuration X. Therefore, in the case of Fe_3O_4, configuration Y is not preferable. Therefore, the competition between the magnetocrystalline anisotropy energy and the exchange energy cannot explain the non-parallel spin configuration of the Fe(A) and Fe(B) site. This indicates that other forces such as Dzialoshinsky-Moriya interaction must be responsible for the non-collinearity of the Fe(A) and Fe(B) spins. Further theoretical studies should be conducted in order to clarify the origin of the non-collinearity.

In addition, the results of the low-/high-temperature NRS shows that the internal magnetic field B_{hf} of the Fe_3O_4 (111) surface is larger than the bulk. There are two possibilities that can explain the difference in the internal magnetic field B_{hf} of the bulk and the (111) surface of Fe_3O_4; The critical exponent β of the surface is different from the bulk,

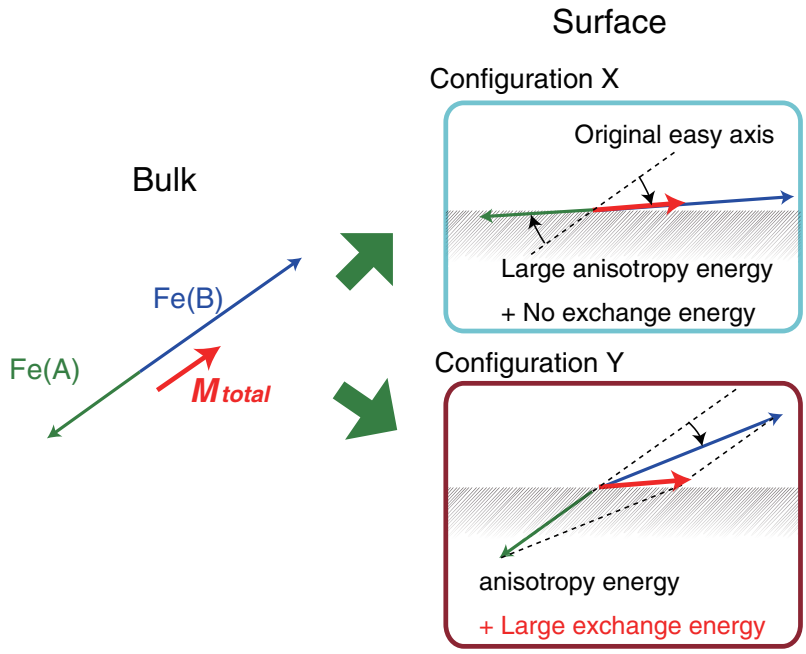

Figure 3.35: Two possible models of spin canting to reduce the magnetostatic energy on Fe_3O_4 (111) surface.

or the curie temperature T_c is higher at the surface than the bulk.

Let us consider the former case. Near the curie temperature, the thermal behavior of the magnetization M is written as

$$M \propto (\frac{T_c - T}{T_c})^{\beta}, \tag{3.7}$$

where T is the temperature, T_c is the curie temperature and β is the critical exponent. For Fe_3O_4, T_c is 839.5 K [59]. The critical exponent β depends on the type of the model (Heisenberg, Ising, etc.) and the dimensionality of the system. For the three-dimensional Ising model, $\beta \sim 5/16$ [65]. According to the previous report by Häggström *et al.* on the powdered Fe_3O_4, β of the bulk is 0.33–0.39 for Fe(A) and 0.35–0.45 for Fe(B) [59]. Table 3.4.3 shows the surface critical exponent β calculated for various models. These results show that β is larger at surfaces than the bulk. Figure 3.36 shows the thermal behavior of the magnetization for $\beta = 1/3$ and 0.8 based on equation 3.7. The temperature dependence of the magnetization becomes less steep as we increase the critical exponent β. This means that, if we consider the effect of two-dimensionality of the surface on the critical exponent, the surface magnetization near the curie temperature should be smaller. Therefore, we consider that the deviation of B_{hf} of the surface from the bulk is due to the difference in the curie temperature. Binder *et al.* reported, using the Monte Carlo method on the three-dimensional Ising model, that the curie temperature T_{cs} of the surface is higher than the bulk curie temperature T_c when the surface exchange constant J_s satisfies $J_s \geq 1.55J$ where J is the bulk exchange constant. Therefore, our present results, which showed that the surface magnetization is larger than the bulk at 500 K, cannot be attributed to the difference in the critical exponent.

Table 3.2: Calculated surface critical exponent β values for various models.

Model	Method	β	Ref.
Ising	Monte Carlo	0.78(2)	[66]
	series expansion	0.77(2)	[67]
	renormalization group	0.80(2)	[68]
xy	Monte Carlo	0.84(1)	[69]
	series expansion	0.79(3)	[67]
Heisenberg isotropic	Monte Carlo	0.75(10)	[70]
	series expansion	0.81(4)	[67]
	renormalization group	0.84(1)	[68]
Heisenberg anisotropic	renormalization group	0.84(1)	[68]

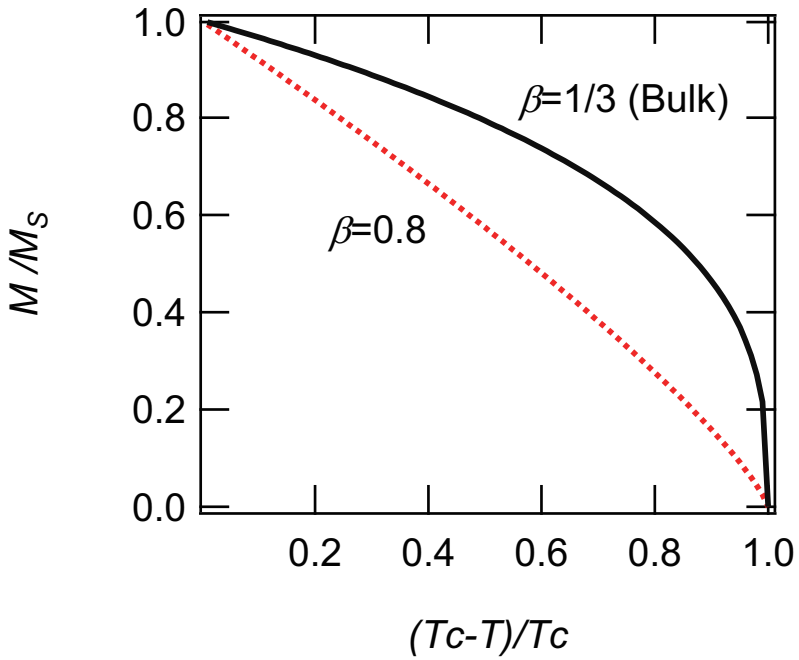

Figure 3.36: The thermal behavior of the magnetization for $\beta = 1/3$ and 0.8.

Based on these considerations, we consider that the peculiar thermal behavior of the internal magnetic field B_{hf} indicates that the surface curie temperature T_c is higher than the bulk. Since the curie temperature is determined by the competition between the exchange interaction and the thermal fluctuation of the spin direction, this results suggest that the exchange interaction of the surface is larger than the bulk.

Chapter 4

Conclusion

In this study, we investigated the electronic and magnetic structure of the Fe_3O_4 (111) surface by low-energy electron diffraction (LEED), ultra-violet photoemission spectroscopy (UPS), nuclear resonant scattering (NRS), and conversion electron Mössbauer spectroscopy. For nuclear resonant X-ray scattering experiments and micro four-point probe measurements, we designed and constructed experimental apparatus.

We prepared two kinds of surfaces, the Fe(A)1-terminated Fe_3O_4 (111) surface and the O_2-exposed Fe(A)1-terminated Fe_3O_4 (111) surface. The LEED pattern exhibited an unreconstructed 1×1 structure. The unreconstructed 1×1 LEED structure was present even below the 120 K where the bulk undergoes the Verwey transition with a structural change from cubic to monoclinic. We considered that the Verwey transition is suppressed at the surface due to the difference in the Fe(B) valence state from the bulk. In order to establish a method for modulating the Fe(B) valence state, we investigated the effect of H adsorption on these surfaces. We have discovered that the H atoms adsorbed on the Fe(A)-terminated Fe_3O_4 (111) surface reduces the work function but does not induce charge transfer. We argue that the H atom adsorbs on the surface as a neutral atom. The decrease of the work function can be explained by the formation of an electric dipole due to the hybridization of H $1s$ orbital with the substrate orbital or the mixing of the H $1s$ and the H $2p$ orbital due to the perturbation by the electric field from the substrate ions. On the O_2-exposed Fe(A)-terminated Fe_3O_4 (111) surface, on the other hand, H adsorption increases the Fe(B) t_{2g} derived peak in the UPS spectrum and decreases the work function. This indicates that the H atoms adsorb as cations on the O_2-exposed Fe(A)-terminated Fe_3O_4 (111) surface and dope electrons to the Fe(B) t_{2g} orbital.

We investigated the magnetic structure of the Fe_3O_4 (111) surface by nuclear resonant X-ray scattering and conversion electron Mössbauer spectroscopy. We found, from the NRS frequency spectra and the peak intensity ratios of CEMS results, that the surface-normal magnetization component is missing on the surface. This indicates that the Fe_3O_4 (111) surface is covered by closure domains. Furthermore, the magnetization direction of the closure domains is found to be tilted from the original easy-magnetization axes to the surface-parallel direction. This is considered to be caused by the effect of magnetostatic energy which tends to rotate the surface magnetization to the surface-parallel direction. We also found that the spin direction of the Fe(A) and Fe(B) sites are non-collinear near the surface. Based on the magnetocrystalline anisotropy and exchange energies of the bulk, we found that the experimental results cannot be explained by the compensation between the exchange, magnetocrystalline anisotropy and the magnetostatic energies. We consider that peculiar exchange interactions such as Dzyaloshinsky-Moriya interaction exist on the Fe_3O_4 (111) surface or that the Fe(A) spins are magnetically harder than the

Fe(B). Furthermore, we measured the temperature dependence of the internal magnetic field by NRS, and discovered that the internal magnetic field of the surface is larger than the reported value of the bulk. This phenomenon indicates that the exchange interaction of the surface is larger than the bulk.

References

[1] H.-T. Jeng and G. Y. Guo: Physical Review B **65** (2002) 094429.

[2] G. S. Parkinson, N. Mulakaluri, Y. Losovyj, P. Jacobson, R. Pentcheva, and U. Diebold: Physical Review B **82** (2010) 125413.

[3] M. Kurahashi, X. Sun, and Y. Yamauchi: Physical Review B **81** (2010) 193402.

[4] C. Martos, J. Dufour, and A. Ruiz: International Journal of Hydrogen Energy **34** (2009) 4475 .

[5] N. Mulakaluri, R. Pentcheva, M. Wieland, W. Moritz, and M. Scheffler: Physical Review Letters **103** (2009) 176102.

[6] E. Verwey: Nature **144** (1939) 327.

[7] F. Walz: Journal of Physics: Condensed Matter **14** (2002) R285.

[8] J. García and G. Subías: Journal of Physics: Condensed Matter **16** (2004) R145.

[9] K. Jordan, A. Cazacu, G. Manai, S. F. Ceballos, S. Murphy, and I. V. Shvets: Physical Review B **74** (2006) 085416.

[10] S. F. Alvarado, M. Erbudak, and P. Munz: Physical Review B **14** (1976) 2740.

[11] Y. S. Dedkov, M. Fonin, D. V. Vyalikh, J. O. Hauch, S. L. Molodtsov, U. Rüdiger, and G. Güntherodt: Physical Review B **70** (2004) 073405.

[12] Z. Zhang and S. Satpathy: Physical Review B **44** (1991) 13319.

[13] I. Leonov, A. Yaresko, V. Antonov, M. Korotin, and V. Anisimov: Physical review letters **93** (2004) 146404.

[14] E. De Grave, R. Persoons, R. Vandenberghe, and P. De Bakker: Physical Review B **47** (1993) 5881.

[15] 金森順次郎: 磁性/金森順次郎著 (新物理学シリーズ. 1969), 新物理学シリーズ.

[16] K. Abe, Y. Miyamoto, and S. Chikazumi: Journal of the Physical Society of Japan **41** (1976) 1894.

[17] G. S. Parkinson, N. Mulakaluri, Y. Losovyj, P. Jacobson, R. Pentcheva, and U. Diebold: Physical Review B **82** (2010) 125413.

[18] Z. Łodziana: Physical Review Letters **99** (2007) 206402.

[19] M. Kurahashi, X. Sun, and Y. Yamauchi: Physical Review B **81** (2010) 193402.

[20] Ö. Özdemir, S. Xu, and D. J. Dunlop: Journal of Geophysical Research: Solid Earth (1978–2012) **100** (1995) 2193.

[21] H.-U. Worm, P. Ryan, and S. Banerjee: Earth and Planetary Science Letters **102** (1991) 71.

[22] E. Lima, A. L. Brandl, A. D. Arelaro, and G. F. Goya: Journal of Applied Physics **99** (2006) 083908.

[23] M. Darbandi, F. Stromberg, J. Landers, N. Reckers, B. Sanyal, W. Keune, and H. Wende: Journal of Physics D: Applied Physics **45** (2012) 195001.

[24] K. L. Krycka, J. A. Borchers, R. A. Booth, Y. Ijiri, K. Hasz, J. J. Rhyne, and S. A. Majetich: Phys. Rev. Lett. **113** (2014) 147203.

[25] A. Thompson, D. Vaughan, C. for X-ray Optics (Lawrence Berkeley National Laboratory), C. for X-ray optics, advanced light source, and L. B. N. L. A. L. Source: *X-ray Data Booklet* (Lawrence Berkeley Laboratory, 2001), p. 2.

[26] J. Moulder and J. Chastain: *Handbook of X-ray Photoelectron Spectroscopy: A Reference Book of Standard Spectra for Identification and Interpretation of XPS Data* (Physical Electronics, 1995).

[27] S. Hasegawa and F. Grey: Surface Science **500** (2002) 84.

[28] Y. Ujihira: Reviews in Analytical Chemistry **8** (1985) 125.

[29] H. Eicher, F. Parak, L. Bogner, and K. Gersonde: Zeitschrift für Naturforschung C **29** (1974) 683.

[30] A. Boyle and H. Hall: Reports on Progress in Physics **25** (1962) 441.

[31] M. Krčmar, Z. Krečak, M. Stipčević, A. Ljubičić, and D. Bradley: Physics Letters B **442** (1998) 38.

[32] T. Kawauchi, K. Fukutani, M. Matsumoto, K. Oda, T. Okano, X. W. Zhang, S. Kishimoto, and Y. Yoda: Physical Review B **84** (2011) 020415.

[33] G. V. Smirnov: Hyperfine Interactions **97-98** (1996) 551.

[34] J. P. Hannon, N. V. Hung, G. T. Trammell, E. Gerdau, M. Mueller, R. Rüffer, and H. Winkler: Physical Review B **32** (1985) 5068.

[35] J. P. Hannon, G. T. Trammell, M. Mueller, E. Gerdau, R. Rüffer, and H. Winkler: Physical Review B **32** (1985) 6363.

[36] G. Smirnov: Hyperfine Interactions **123** (1999) 31.

[37] R. Röhlsberger: *Nuclear Condensed Matter Physics with Synchrotron Radiation: Basic Principles, Methodology and Applications* (Number 208. Springer, 2004), number 208.

[38] J. Hannon and G. Trammell: Physica B: Condensed Matter **159** (1989) 161.

[39] L. Kalev and L. Niesen: Physical Review B **67** (2003) 224403.

[40] T. Kawauchi, X. Zhang, and K. Fukutani: Journal of Magnetism and Magnetic Materials (2016).

[41] O. Öztürk and D. Williamson: Journal of Applied Physics **77** (1995) 3839.

[42] J. M. Thomas, M. J. Tricker, and A. P. Winterbottom: J. Chem. Soc., Faraday Trans. 2 **71** (1975) 1708.

[43] Y. Suetsugu, M. Shiraishi, T. Mishiba, and Y. Ohno: Journal of Vacuum Science & Technology A **17** (1999) 3500.

[44] L. Zhu, K. L. Yao, and Z. L. Liu: Phys. Rev. B **74** (2006) 035409.

[45] M. Paul, M. Sing, R. Claessen, D. Schrupp, and V. A. M. Brabers: Physical Review B **76** (2007) 075412.

[46] S. K. Shaikhutdinov, M. Ritter, X.-G. Wang, H. Over, and W. Weiss: Physical Review B **60** (1999) 11062.

[47] M. Ritter and W. Weiss: Surface science **432** (1999) 81.

[48] Y. S. Dedkov, M. Fonin, D. V. Vyalikh, J. O. Hauch, S. L. Molodtsov, U. Rüdiger, and G. Güntherodt: Physical Review B **70** (2004) 073405.

[49] S. Alvarado, M. Erbudak, and P. Munz: Physical Review B **14** (1976) 2740.

[50] Z. Zhang and S. Satpathy: Physical Review B **44** (1991) 13319.

[51] H.-T. Jeng and G. Guo: Physical review B **65** (2002) 094429.

[52] N. Berdunov, S. Murphy, G. Mariotto, and I. Shvets: Physical Review B **70** (2004) 085404.

[53] H. Ishida: Physical Review B **38** (1988) 8006.

[54] T. K. Shimizu, J. Jung, H. S. Kato, Y. Kim, and M. Kawai: Phys. Rev. B **81** (2010) 235429.

[55] N. Spiridis, D. Wilgocka-Ślezak, K. Freindl, B. Figarska, T. Giela, E. Młyńczak, B. Strzelczyk, M. Zajac, and J. Korecki: Physical Review B **85** (2012) 075436.

[56] A. Baron, J. Arthur, S. Ruby, A. Chumakov, G. Smirnov, and G. Brown: Physical Review B **50** (1994) 10354.

[57] N. Wu: *The maximum entropy method* (Springer Science & Business Media, 2012), Vol. 32.

[58] N. Spiridis, B. Handke, T. Slezak, J. Barbasz, M. Zajac, J. Haber, and J. Korecki: The Journal of Physical Chemistry B **108** (2004) 14356.

[59] L. Häggström, H. Annersten, T. Ericsson, R. Wäppling, W. Karner, and S. Bjarman: Hyperfine Interactions **5** (1977) 201.

[60] G. J. Long: *Mössbauer spectroscopy applied to inorganic chemistry* (Springer Science & Business Media, 1984), Vol. 1.

[61] G. A. Sawatzky, F. Van Der Woude, and A. H. Morrish: Phys. Rev. **183** (1969) 383.

[62] N. Spiridis, B. Handke, T. Slezak, J. Barbasz, M. Zajac, J. Haber, and J. Korecki: The Journal of Physical Chemistry B **108** (2004) 14356.

[63] R. Bauminger, S. Cohen, A. Marinov, S. Ofer, and E. Segal: Physical Review **122** (1961) 1447.

[64] W. Kündig and R. S. Hargrove: Solid State Communications **7** (1969) 223.

[65] H. E. Stanley: Introduction to Phase Transitions and Critical Phenomena, by H Eugene Stanley, pp. 336. Foreword by H Eugene Stanley. Oxford University Press, Jul 1987. ISBN-10: 0195053168. ISBN-13: 9780195053166 **1** (1987).

[66] K. Binder and D. Landau: Physical review letters **52** (1984) 318.

[67] K. Ohno, Y. Okabe, and A. Okabe: Progress of theoretical physics **71** (1984) 714.

[68] H. Diehl and E. Eisenriegler: Physical Review B **30** (1984) 300.

[69] D. Landau, R. Pandey, and K. Binder: Physical Review B **39** (1989) 12302.

[70] M. Landolt, R. Allenspach, and D. Mauri: Journal of applied physics **57** (1985) 3626.